Strojniški vestnik
Journal of Mechanical Engineering

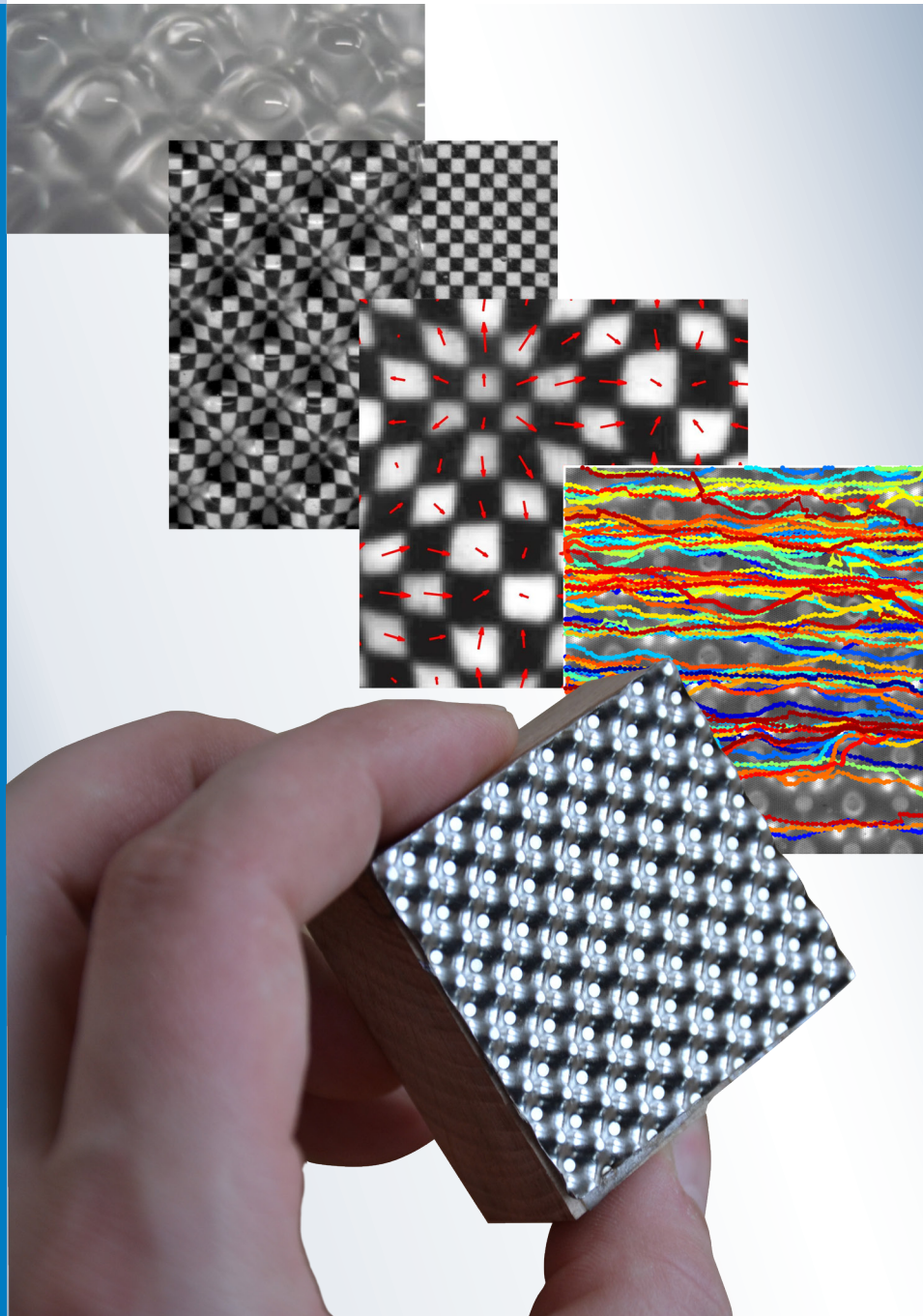

no. 1
year 2016
volume 62

Strojniški vestnik – Journal of Mechanical Engineering (SV-JME)

Aim and Scope
The international journal publishes original and (mini)review articles covering the concepts of materials science, mechanics, kinematics, thermodynamics, energy and environment, mechatronics and robotics, fluid mechanics, tribology, cybernetics, industrial engineering and structural analysis.
The journal follows new trends and progress proven practice in the mechanical engineering and also in the closely related sciences as are electrical, civil and process engineering, medicine, microbiology, ecology, agriculture, transport systems, aviation, and others, thus creating a unique forum for interdisciplinary or multidisciplinary dialogue.
The international conferences selected papers are welcome for publishing as a special issue of SV-JME with invited co-editor(s).

Editorial Office
University of Ljubljana, Faculty of Mechanical Engineering
SV-JME, Aškerčeva 6, SI-1000 Ljubljana, Slovenia
Phone: 386 (0)1 4771 137
Fax: 386 (0)1 2518 567
info@sv-jme.eu, http://www.sv-jme.eu

Print: Grafex, d.o.o., printed in 310 copies

Founders and Publishers
University of Ljubljana, Faculty of Mechanical Engineering, Slovenia
University of Maribor, Faculty of Mechanical Engineering, Slovenia
Association of Mechanical Engineers of Slovenia
Chamber of Commerce and Industry of Slovenia, Metal Processing Industry Association

Cover: Image depicts the entire technology chain for inspection of periodically corrugatted plate heat exhangers (CPHE): a fabricated corrugated plate for fluid flow visualization, a checkerboard pattern distorsion introduced by corrugation, it's estimation by image processing algorithm and streamlines obtained by particle tracking and distortion compensation algorithm. In foreground: a steel-mould for hot-embossing of transparent corrugatted plate.

Courtesy: Jaka Pribošek, University of Ljubljana, Faculty of Mechanical Engineering, Slovenia

ISSN 0039-2480

General information
Strojniški vestnik – Journal of Mechanical Engineering is published in 11 issues per year (July and August is a double issue).

Institutional prices include print & online access: institutional subscription price and foreign subscription €100,00 (the price of a single issue is €10,00); general public subscription and student subscription €50,00 (the price of a single issue is €5,00). Prices are exclusive of tax. Delivery is included in the price. The recipient is responsible for paying any import duties or taxes. Legal title passes to the customer on dispatch by our distributor.

Single issues from current and recent volumes are available at the current single-issue price. To order the journal, please complete the form on our website. For submissions, subscriptions and all other information please visit: *http://en.sv-jme.eu/.*

You can advertise on the inner and outer side of the back cover of the journal. The authors of the published papers are invited to send photos or pictures with short explanation for cover content.

We would like to thank the reviewers who have taken part in the peer-review process.

The journal is subsidized by Slovenian Research Agency.

Strojniški vestnik - Journal of Mechanical Engineering is available on http://www.sv-jme.eu, where you access also to papers' supplements, such as simulations, etc.

Contents

Strojniški vestnik - Journal of Mechanical Engineering
volume 62, (2016), number 1
Ljubljana, January 2016
ISSN 0039-2480

Published monthly

Papers

Strojniški vestnik - Journal of Mechanical Engineering 62(2016)1, 3-10

DOI:10.5545/sv-jme.2015.3125 Original Scientific Paper
Received for review: 2015-10-17
Received revised form: 2015-11-17
Accepted for publication: 2015-11-24

Correcting the Periodic Optical Distortion for Particle-Tracking Velocimetry in Corrugated-Plate Heat Exchangers

Jaka Pribošek[1,*] – Miha Bobič[2] – Iztok Golobič[1] – Janez Diaci[1]
[1] University of Ljubljana, Faculty of Mechanical Engineering, Slovenia
[2] Danfoss Trata, Slovenia

To improve current methods for the experimental validation of numerical simulations in corrugated-plate heat exchangers (CPHEs), a full-field quantitative velocimetry of fluid flow is required. This paper investigates the application of particle-tracking velocimetry (PTV) to modified CPHEs. For this, an experimental CPHE unit with a transparent, corrugated upper plate was built. We show that by viewing through a corrugated, refractive interface, a complex periodic optical distortion is introduced, that affects and corrupts the estimated particle trajectories. As this problem cannot be addressed using existing calibration techniques, we propose a novel calibration algorithm for periodic optical distortion. The algorithm relies on the automatic detection of nonlinear distortion using a checkerboard target place within the CPHE unit. The calibration is first made on a coarse grid and subsequently refined by a set of low-order periodic basis functions in order to seize the periodic nature of the deformation field. The proposed algorithms have been applied to a test case with known, uniform particle velocities in order to demonstrate the performance. When applied to a real case, a reduction in the systematic positional error by 35 % was demonstrated.
Keywords: optical distortion, corrugated-plate heat exchanger, particle-tracking velocimetry

Highlights
- *We modified corrugated-plate heat-exchanger units to allow fluid-flow visualization and applied a particle-tracking velocimetry to measure the flow.*
- *We addressed the problem of periodic optical distortion due to the view through corrugated refractive interfaces.*
- *A novel calibration method allowing for periodic optical distortion has been introduced.*
- *Experimental results using the proposed algorithms show a reduction in the systematic error by 35 %.*

0 INTRODUCTION

Plate heat exchangers (PHEs) have recently been gaining more attention owing to their high overall heat-transfer coefficient, compactness and implementation flexibility. As such, they are finally replacing the traditional tubular designs in various process applications [1]. Recent improvements to heat-transfer efficiency, a higher heat-transfer-area-to-volume ratio and a lower pressure drop have been achieved by the micro-corrugation of PHE surfaces – the so-called corrugated PHE (CPHE) [2].

Design optimization of the corrugated surface is crucial for tailoring this technology for various applications. So far, very few studies have addressed the optimization problem. Such optimizations of PHEs were mainly studied using CFD simulations [3]. However, the validation of these CFD simulations has mainly been limited to the overall pressure drop and to inlet/outlet temperature measurements [4]. To further extend the validation possibilities, the pressure distribution has recently been measured in a CPHE unit [5]. IR thermography has been applied to obtain a deeper understanding of the temperature fields and flow patterns inside the PHE [6] and [7]. In terms of a CFD validation, the existing methods still have a very limited scope.

The lack of experimental systems aimed at an internal flow inspection was first addressed by Focke and Knibbe [8]. In this study one of the plates of a plate heat exchanger was replaced by its transparent acrylic equivalent, enabling the visualization of the flow patterns inside the PHE. This pioneering study was able to draw many important conclusions and influenced many others that utilized similar experimental setups for the purpose of optimizing CFD codes [9] and [10] or experimental studies on fluid-flow phenomena [11] to [13]. Although most of the reported experimental units enable fluid-flow monitoring, no studies on the velocity fields inside PHEs can be found in the literature. One of the main reasons for this is the challenging system calibration due to the complex optical distortion that occurs in such situations.

Up to now, different optical setups, such as telecentric lenses and Scheimpflug camera configurations [14] to [16], have been exploited to minimize the distortion and compensate for the projection error. In this way, the calibration of a PTV system is fairly straightforward and simple image registration or scaling may be needed. This approach,

*Corr. Author's Address: University of Ljubljana, Faculty of Mechanical Engineering, Aškerčeva 6, SI-1000 Ljubljana, Slovenia jaka.pribosek@fs.uni-lj.si

however, does not allow for the compensation of the errors that arise from viewing through refractive interfaces. An analytic study of viewing through a refractive freeform optical interface is presented in [17], while others employ ray-tracing techniques. A generalized system-calibration procedure for optical setups used in particle velocimetry was proposed by Soloff et al. [18], followed by various improvements [19] to [22], as well as various self-calibrating schemes [23]. Existing techniques exploit either polynomial or rational models to model the optical distortion, which is generally sufficient to account for the distortion introduced by either the camera optics or the refractive interfaces, such as optical flats or cylindrical pipes. In the case that more complex, arbitrary distortion occurs, the refractive-matching technique is usually employed to avoid the distortion-compensation problem [24] and [25], since no general optical-distortion models accounting for such cases exist. Extending the work of Soloff et al. in this direction has also been suggested as a further desirable improvement to the PIV and PTV methods [26], although no further studies could be found, to the best of our knowledge.

In an experimental CPHE system, the upper plate is transparent and corrugated periodically, which results in periodic, freeform optical distortion. In our study, we provide experimental evidence that the results from the PTV in the CPHE are highly erroneous when left uncalibrated. In such a situation, the corrugation of the CPHE is small, implying that extremely dense calibration patterns are to be used for the calibration in order to provide sufficient sampling. This often has many practical limitations in regions where total internal reflection due to oblique interfaces occurs, which significantly limits the maximum density of the calibration pattern.

This paper provides a novel method for estimating the periodic optical distortion using a coarse grid pattern, subsequently refined using a discrete cosine transform. This allows us to capture the periodic nature of the deformation fields and still keep a coarse calibration pattern. We believe the proposed study is a first step towards a quantitative fluid-flow inspection inside a CPHE, which would be of great help in the validation of the CFD corrugation optimization.

1 METHODS

Our experimental corrugated heat-exchanger unit (Fig. 1) is based on the experimental designs reported in [8], [10] and [11], where the fluid flow is inspected at the cold side of the heat exchanger, and the flow is visualized through a transparent plate. A corrugated surface is first fabricated from 0.5-mm stainless-steel sheet by means of microforging technology. The corrugation of the plate is two-dimensional with an amplitude of 1.5 mm and a period of 7 mm in both the x and y directions fabrication of its transparent counterpart, avoiding the need for costly master-tool fabrication. The master, together with the PMMA sheet, is then preheated to 150 °C in a ventilated oven. The hot PMMA is then sandwiched between the negative master, on the one side, and the additional glass plate, on the other, and then pressed in a manual clamping press with a 35-kN clamping force and left for 25 min to cool. Next, the corrugated stainless-steel plate is inserted into the CNC-cut aluminum holder with integrated inlet and outlets and glued with an epoxy that has a high level of aluminum content for a better heat transfer. The pressure drop across the heat exchanger can be monitored with a pressure sensor (PS). The sensor data is acquired with an Agilent DS 34970A connected to a personal computer.

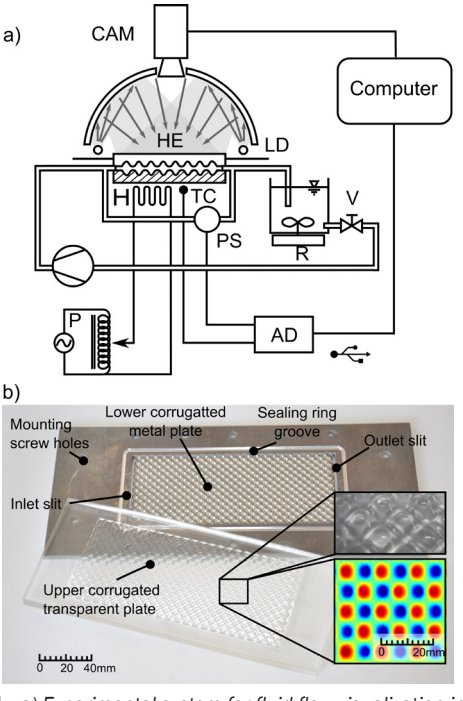

Fig. 1. *a) Experimental system for fluid-flow visualization inside the CPHE, and b) fabricated CPHE unit*

The fluid flow is monitored using a high-speed camera (Camelopard EVO, Optomotive L.t.d.), featuring 360 FPS streaming for an image size of 2048×1088 pixels and a pixel size of 5.5 μm. The camera was equipped with a standard 16-mm C-mount lens. Special attention was given to ensure the proper lighting conditions for the corrugated plate, which

seems to be a problem that has not received much attention in previous studies [8] and [27]. In order to prevent unwanted shadows and reflections as much as possible, we use homogenous lightning conditions. This was achieved using an improvised lightning tunnel as a variation of the classic Ulbricht Sphere illuminated with eight high-power LED diodes (LD), yielding a high-quality image.

The corrugated, transparent plate in contact with the fluid beneath the plate is a composite optical element that refracts the incident light. If the effects of pressure and temperature are neglected, the light travels in straight rays.

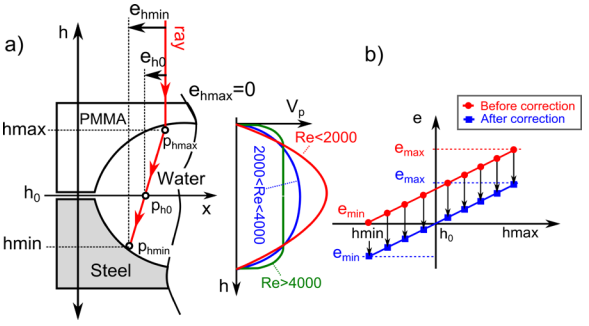

Fig. 2. *a) Three particles at different lateral positions along the same optical ray b) Error reduction by distortion compensation*

Fig. 2 depicts three particles, P_{h0}, P_{hmax} and P_{hmin}, along the same optical ray, that all correspond to the same image position on the camera. Regarding their actual position, the errors E_{h0}, E_{hmax} and E_{hmin} are present in the case of P_{hmax} and P_{hmin}, respectively. The error curve is linear, given by $E(h) = kh + e_{h0}$, and represented by the upper linear curve in Fig. 2b. By subtracting the displacement of P_{h0}, the error curve is shifted to zero (see the lower linear curve of Fig. 2b) modelled as $E(h) = kh + e_{h0}$. What interests us the most, however, is how the calibration affects the total error. This is formulated as an integral of the product of $E(h)$ and the probability $p(h)$ that a particle can be found at one particular height $E_{tot} = \int_{hmin}^{hmax} E(h)\,p(h)\,dh.$ Under the assumption of uniformly spread particles in the fluid, the probability $p(h)$ equals the normalized velocity distribution. By inserting the error functions, we estimate the difference between the corrected and uncorrected total errors $E_{tot} - E_{ctot} = \int_{hmin}^{hmax} e_{h0} v_{norm}(h)\,dh$, which for a positive definite function $v_{norm}(h)$ is always greater than zero. In highly distributed, turbulent flows, such as in a CPHE with Re > 4000, the effects of surface friction are less significant and the velocity-distribution function can be approximated using a uniform function (Fig. 2), for which the corresponding probability function sums to a unit one. As such, by means of a single plane planar calibration we reduced the total error of all the particles, regardless of their height, at least for the term $e_{h0}(hmax - hmin)$, or greater in the case of less turbulent flows.

1.1 Optical Distortion Correction

Given the two different domains, the Image domain $\mathcal{I}$ (observed) and the Cartesian domain $\mathcal{C}$ (hidden state), we refer to the mapping $\mathcal{I} \xrightarrow{T} \mathcal{C}$ as direct mapping, and $\mathcal{C} \xrightarrow{T^{-1}} \mathcal{I}$ as the inverse mapping between both domains. We estimate the unknown mappings by observing a fiducial checkerboard pattern through the corrugation plate placed at the middle of the cavity, formed by both plates of the corrugated-plate heat exchangers, yielding exact point-to-point correspondences between both domains.

1.2 Image Processing

We have developed a custom algorithm for an automatic mapping estimation based on image processing of the distorted view of a fiducial pattern (Fig. 3). For this a checkerboard pattern was employed, since by considering both white and black regions, a four-times-higher information density is obtained compared to conventional dot patterns. First, an adaptive threshold is applied in order to binarize the image and to eliminate the effects of the illumination gradient that may occur. This was achieved with a 10×10 window, where the local threshold was set according to the average intensity of that region. After the binarization we apply a morphological erosion to isolate the connected white regions. Two-pass connected component labelling is then applied for their segmentation, allowing us to calculate the centroid point of each blob i. The very same procedure is then repeated for the segmentation of the black regions, whereas the morphological erosion was replaced by dilation.

The detected feature points were then meshed using Delaunay triangulation. To each triangle, a circumcircle is calculated. The centroid of the circumcircle is then used to define the nearest neighboring triangle. The two triangles are combined to form a quadrilateral shape, which is then ordered in a grid using the recursive grid-finding algorithm. This grid-finding algorithm starts from an initial, randomly

chosen 3×3 neighborhood, which is inserted into an empty matrix *M*. From the remaining neighborhoods in the set, the one with at least one matching node is chosen and inserted into *M* such that the matching elements overlap. We repeated this procedure in a recursive manner until all the neighborhoods were assigned to *M*. The result of the represented segmentation and meshing is the formation of point-to-point correspondences with a Cartesian uniform mesh required to estimate the optical distortion.

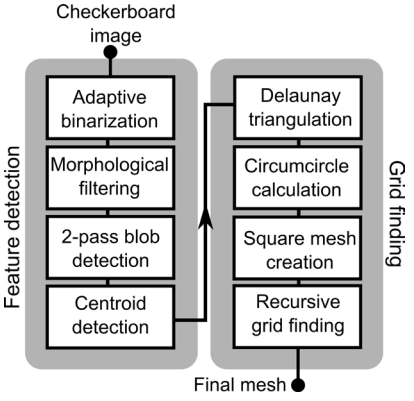

Fig. 3. *The complete calibration algorithm*

1.3 Rigid-Body Registration

By analyzing the point-to-point correspondences between both domains, we attempt to estimate the mapping between them. Fig. 4 shows the major steps of the nonlinear spatial deformation field estimation. Let p_i be the observed vertices in the Image domain and q_i the corresponding hidden vertices in the Cartesian domain of the same fiducial pattern, for $i=1,...,N$. We may then split the mapping T we are searching for into a *rigid-body transformation term H* (camera extrinsic parameters) and a *nonlinear deformation field* δ_i induced by the optical distortion of the corrugated plate $q_i=\mathrm{H}p_i+\delta_i$. Using the homogenous coordinate notation for the given point-to-point correspondences p_i and q_i, $i=1,...,N$ we have:

$$\begin{bmatrix} q_{xi} \\ q_{yi} \\ 1 \end{bmatrix}^{\mathcal{C}} = \begin{bmatrix} s_x\cos\alpha & -s_y\sin\alpha & t_x \\ s_x\sin\alpha & s_y\cos\alpha & t_y \\ 0 & 0 & 1 \end{bmatrix} \begin{bmatrix} p_{xi} \\ p_{yi} \\ 1 \end{bmatrix}^{\mathcal{I}} + \begin{bmatrix} \delta_{xi} \\ \delta_{yi} \\ 0 \end{bmatrix}^{\mathcal{C}}. \quad (1)$$

Assuming an isotropic scaling $s_x=s_y=s$ we can reformulate the following least-square system, minimizing the δ_i terms, yielding a rigid-body registration that accounts for the camera pose (α, t_x, t_y), and the optical magnification (s):

$$\begin{bmatrix} p_{x1} & -p_{y1} & 1 & 0 \\ p_{y1} & p_{x1} & 0 & 1 \\ p_{x2} & -p_{y2} & 1 & 0 \\ p_{y2} & p_{x2} & 0 & 1 \\ \vdots & \vdots & \vdots & \vdots \\ p_{xn} & -p_{yn} & 1 & 0 \\ p_{yn} & p_{xn} & 0 & 1 \end{bmatrix} \begin{bmatrix} s\cos(\alpha) \\ s\sin(\alpha) \\ t_x \\ t_y \end{bmatrix} = \begin{bmatrix} q_{x1} \\ q_{y1} \\ q_{x2} \\ q_{y2} \\ \vdots \\ q_{xn} \\ q_{yn} \end{bmatrix}. \quad (2)$$

The above system $Ax=y$ is solved for x using the singular value decomposition (SVD) and yields the elements of the rigid-body transformation matrix H. This then allows the characterization of the nonlinear terms induced by the optical distortion as the difference between q and p':

$$\begin{bmatrix} \delta_{xi} \\ \delta_{yi} \end{bmatrix} = \begin{bmatrix} q_{xi} \\ q_{yi} \end{bmatrix} - \begin{bmatrix} p_{xi}' \\ p_{yi}' \end{bmatrix}, \quad (3)$$

where p' denotes the p being transformed to $\mathcal{C}$:

$$\begin{bmatrix} \delta_{xi} \\ \delta_{yi} \\ 0 \end{bmatrix}^{\mathcal{C}} = \begin{bmatrix} q_{xi} \\ q_{yi} \\ 1 \end{bmatrix}^{\mathcal{C}} - \begin{bmatrix} s\cos\alpha & -s\sin\alpha & t_x \\ s\sin\alpha & s\cos\alpha & t_y \\ 0 & 0 & 1 \end{bmatrix} \begin{bmatrix} p_{xi} \\ p_{yi} \\ 1 \end{bmatrix}^{\mathcal{I}}, \quad (4)$$

where δ_{xi} and δ_{yi} then represent the required deformation field, evaluated for the region i.

3.3 Parametrization of the Deformation Fields

In order to ensure good sampling of the deformation field, we strive to keep the fiducial calibration pattern as dense as possible, while still maintaining good performance and robust segmentation. Regardless of all the efforts, the obtained sampling frequency of the optical distortion remains very low. However, since the structures of the corrugated plate have a periodic geometry, the deformation field induced by the optical distortion will be periodic. Since we sample the displacement field with a sampling frequency that is a non-integer multiple of the fundamental frequency of the periodic structures, we may exploit this fact to further improve the estimation of the optical distortion. We do this by modelling a spatial deformation vector field as a linear combination of some periodic basis functions. The basis function used here are a few frequency components (< 300) of the two-dimensional direct cosine transform (2D DCT) of the input deformation field. The transform of the variable $\delta_x^{\{\mathcal{C}\}}(k_1,k_2)$ in the Cartesian domain to $F(k_1,k_2)$ in the frequency domain for the 2D DCT is given in [28]:

$$F(k_1,k_2)=\alpha(k_1)\alpha(k_2)\sum_{n_1=0}^{N_1-1}\sum_{n_2=0}^{N_2-1}\delta_x^{\{C\}}(k_1,k_2)$$
$$\cos\left(\frac{\pi(2n_1+1)k_1}{2N_1}\right)\cos\left(\frac{\pi(2n_2+1)k_2}{2N_2}\right), \quad (5)$$

for $k_1=0,1,...,N_1-1$ and $k_2=0,1,...,N_2-1$ and $\alpha(k)$ defined as:

$$\alpha(k)=\begin{cases}\sqrt{\frac{1}{N}}, & for\ k=0\\ \sqrt{\frac{2}{N}}, & for\ k=1,2,\ldots,N-1\end{cases}. \quad (6)$$

Analogously to Eq. (6), we write the same for the transformation of $\delta_y^{\{C\}}(k_1,k_2)$.

Using the 2D DCT, we enforce the periodicity on the estimated "sparse" deformation field by blocking some of the lowest and highest frequency components. Using the filtered $\tilde{F}(k_1,k_2)$ we reproduce the filtered deformation field as:

$$\widetilde{\delta}_x^{\{C\}}(k_1,k_2)=\sum_{k_1=0}^{N_1-1}\sum_{k_2=0}^{N_2-1}\alpha(k_1)\alpha(k_2)\tilde{F}(k_1,k_2)$$
$$\cos\left(\frac{\pi(2n_1+1)k_1}{2N_1}\right)\cos\left(\frac{\pi(2n_2+1)k_2}{2N_2}\right), \quad (7)$$

for $n_1=0,1,...,N_1-1$ and $n_2=0,1,...,N_2-1$.

In addition to this, knowing the deformation field as an linear combination of some basis functions allows us to upsample the original deformation field (Fig. 5b), while maintaining the smoothness and periodicity constraints. Since the parametrization was made in the Cartesian domain, we apply a backward transform to the image domain, and interpolate it over the entire domain to prepare the look-up table for an efficient implementation.

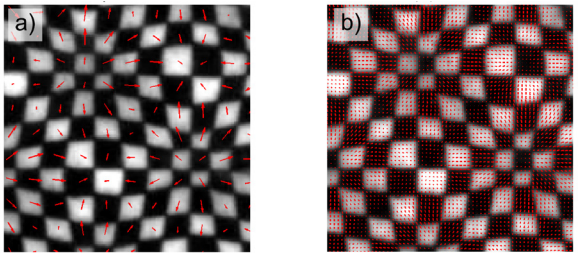

Fig. 5. *a) Original and b) upsampled and smoothed deformation field; the magnitude of the deformation field on right was scaled down for the sake of clarity*

After the calibration we acquire an image stream of the particles flowing through the CPHE section. The outcome of the general PTV algorithm is a state vector built from particle positions and velocities in the image domain $\mathcal{I}$:

$$S_k^{\{\mathcal{I}\}}=\left[x\ \dot{x}\ y\ \dot{y}\right]^T. \quad (8)$$

where k runs through all the detected particles. To allow an estimation of the true physical quantities in the Cartesian domain, the trajectories are corrected by the mapping build from the deformation fields $\widetilde{\delta}_x$ and $\widetilde{\delta}_y$:

$$\begin{bmatrix}s'_k\\1\end{bmatrix}^{\{C\}}=\begin{bmatrix}s_x & 0 & 0 & 0 & \widetilde{\delta}_x(x,y)\\ 0 & s_x & 0 & 0 & \widetilde{\delta}_x(x+\dot{x}t,y+\dot{y}t)-\widetilde{\delta}_x(x,y)\\ 0 & 0 & s_y & 0 & \widetilde{\delta}_y(x,y)\\ 0 & 0 & 0 & s_y & \widetilde{\delta}_y(x+\dot{x}t,y+\dot{y}t)-\widetilde{\delta}_y(x,y)\\ 0 & 0 & 0 & 0 & 1\end{bmatrix}, \quad (9)$$

2 EXPERIMENTAL

2.1 Optical Distortion Estimation

We inspect the optical distortion at the central section plane of the CPHE unit, in such a way that the fiducial pattern is pressed against the upper corrugated plate. Fig. 6 shows the periodically distorted view of the calibration pattern. As seen from Fig. 6, the distortion cannot be neglected as it would result in erroneous particle trajectories and velocities. The distortion compensation is thus crucial and is discussed in Section 4.2.

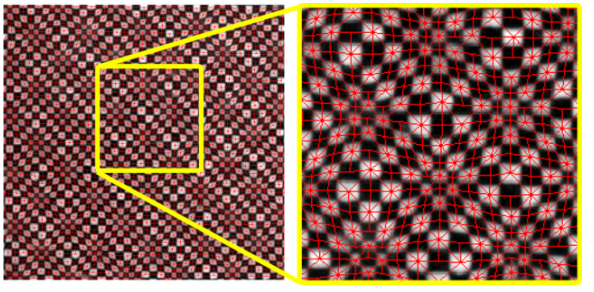

Fig. 6. *Periodically distorted view of the fiducial calibration pattern observed through CPHE; the image is overlaid with an automatically detected mesh that corresponds to the Cartesian grid of the fiducial pattern*

2.2 Evaluation of the PTV Correction Algorithm

We tested the performance of the proposed methods in a test case involving the one-dimensional uniform flow of fiducial particles. First, the system was calibrated as described in Section 4.1 in a central section plane of the heat-exchanger unit. Next, a

fiducial, randomized polka-dot pattern was placed below the corrugated plate at different heights from the central section, i.e., 0.5 mm, 1 mm, 1.5 mm and 2.0 mm.

In this way the effects of the particle flow at various heights were simulated. The pattern is then translated in the x direction in steps of 500 μm using a precision micro-translation stage. This means that the simulated velocity-field distribution of the particles is known to be uniform and one dimensional (no x-velocity components present). This allows us to evaluate the spatial errors of the particle trajectories before and after the correction. To each trajectory, a line has been fitted, and the deviation from the line has been analyzed. The mean total error in Table 1 is then calculated as the mean of all the absolute deviations from the straight lines.

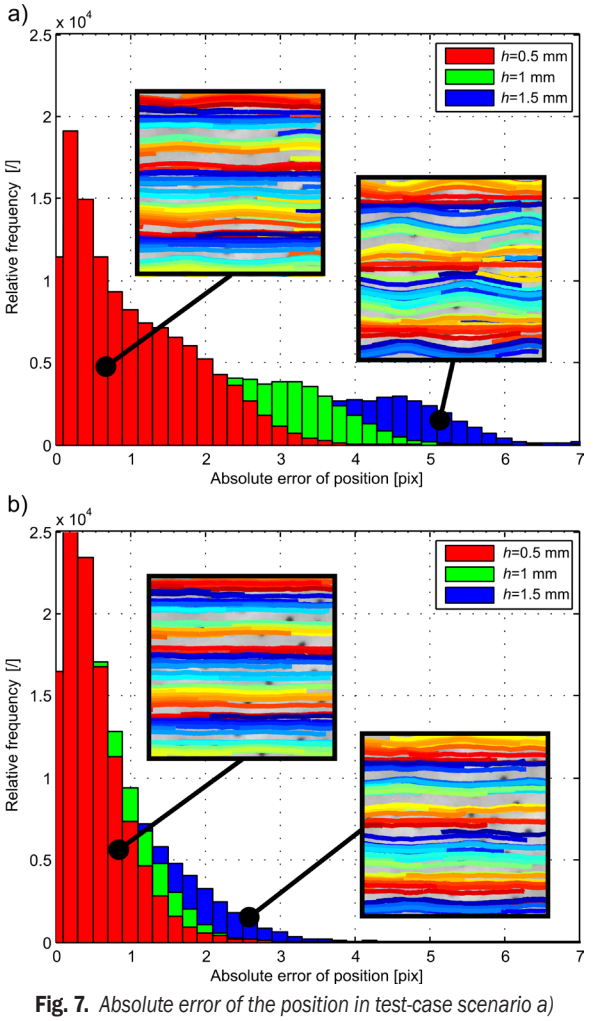

Fig. 7. *Absolute error of the position in test-case scenario a) before and b) after distortion correction (see online journal for color version of this figure)*

3 DISCUSION

Fig. 7 shows the total error evaluated for all the streamlines before the correction. Here, the total error increases with the depth of the particles. Fig. 8 represents the same trajectories after the distortion compensation. The distortion was measured at the central section plane (h = 0), so the positional errors are reduced in proportion to the particle height. Table 1 represents the exact percentage of the error elimination that is gained by the distortion correction.

Table 1. *Mean total error before and after correction*

	Height [mm]	Mean total error before correction [pix]	Mean total error after correction [pix]	Percentage error eliminated [%]
Test case	0.5	1.0	0.51	51.0
	1	1.54	0.60	61.1
	1.5	2.12	0.87	58.9
Real case	/	5.75	3.99	30.6

Applying the same principle to the real case, the percentage difference before and after the correction is less significant. This is due to the fact that some

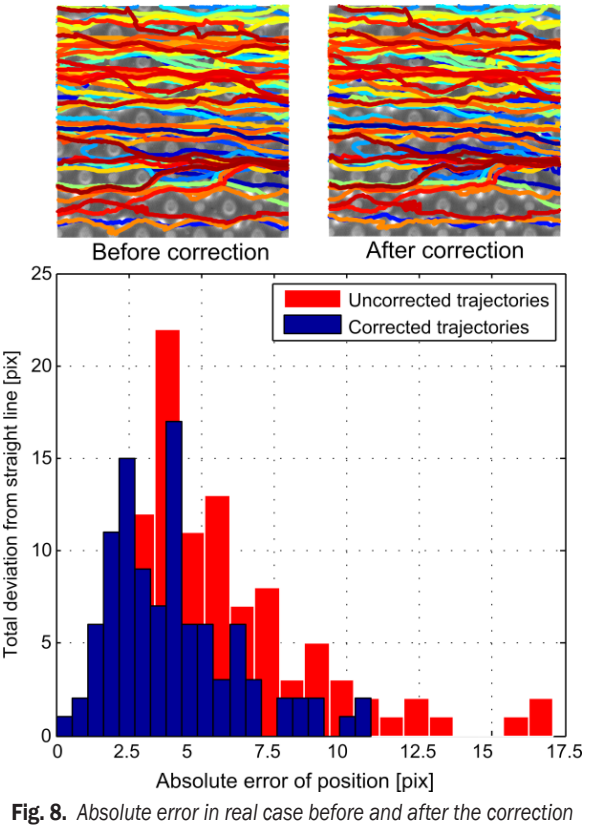

Fig. 8. *Absolute error in real case before and after the correction (see online journal for color version of this figure)*

particles flow above the central section plane, and when calibrated, a small positional error is introduced, as clarified in Section 1. Last but not least, it is worth mentioning that by knowing the exact height of each individual particle, obtained using any type of 3D velocimetry method, the error of the particle trajectory could be completely eliminated. For this, a volumetric calibration would be required, which could be easily performed by applying the same calibration procedures at multiple heights.

4 CONCLUSION

In this study we report on the design of an experimental framework to study the fluid-flow phenomena inside a corrugated-plate heat exchanger. We analyzed the error of the conventional particle-tracking velocimetry due to the optical distortion induced by the corrugated optical interface. We developed an automatic calibration algorithm in order to estimate the nonlinear periodic deformation field, used to partially eliminate the positional error of the particle-tracking velocimetry. The presented experimental framework and methods enable a deeper insight into the flow phenomena inside corrugated PHEs and facilitate experimental studies and the optimization of corrugated-plate heat exchangers. Further work towards 3D velocimetry would open up possibilities to eliminate the error completely.

5 REFERENCES

[1] Wang, L., Sundén, B., Manglik, R.M. (Eds.) (2007). *Plate Heat Exchangers: Design, Applications and Performance*. WIT Press, Southampton.

[2] Ansari, M.S., Mishra, P., Gaikwad, K., Awachat, P.N. (2014). Heat transfer analysis of corrugated plate heat exchanger over coil type heat exchanger: A review. *International Journal of Engineering Research and Technology*, vol. 3, no. 3, p. 446-449.

[3] Aslam Bhutta, M.M., Hayat, N., Bashir, M.H., Khan, A.R., Ahmad, K.N., Khan, S. (2012). CFD applications in various heat exchangers design: A review. *Applied Thermal Engineering*, vol. 32, p. 1-12, **DOI:10.1016/j.applthermaleng.2011.09.001**.

[4] Gullapalli, V.S., Sundén, B. (2014). CFD simulation of heat transfer and pressure drop in compact brazed plate heat exchangers. *Heat Transfer Engineering*, vol. 35, no. 4, p. 358-366, **DOI:10.1080/01457632.2013.828557**.

[5] Ahn, C.H., Choi, J., Son, C., Min, J.K., Park, S. H., Gillespie, D., Go, J.S. (2013). Measurement of pressure distribution inside a cross-corrugated heat exchanger using microchannel pressure tappings. *Measurement Science and Technology*, vol. 24, no. 3, p. 035306, **DOI:10.1088/0957-0233/24/3/035306**.

[6] Kabelac, S. (2010). Analysis of local heat transfer in plate heat exchangers for flow pattern optimisation. *14th International Heat Transfer Conference*, vol. 4, p. 375-384, **DOI:10.1115/IHTC14-22387**.

[7] Freund, S., Kabelac, S. (2010). Investigation of local heat transfer coefficients in plate heat exchangers with temperature oscillation IR thermography and CFD. *International Journal of Heat and Mass Transfer*, vol. 53, no. 19-20, p. 3764-3781, **DOI:10.1016/j.ijheatmasstransfer.2010.04.027**.

[8] Focke, W.W., Knibbe, P.G. (1986). Flow visualization in parallel-plate ducts with corrugated walls. *Journal of Fluid Mechanics*, vol. 165, p. 73-77, **DOI:10.1017/S0022112086003002**.

[9] Paras, S.V., Kanaris, A.G., Mouza, A.A., Karabelas, A.J. (2002). CFD code application to flow through narrow channels with corrugated walls. *15th International Congress of Chemical and Process Engineering*.

[10] Kanaris, A.G., Mouza, K.A., Paras, S.V. (2004). Designing novel compact heat exchangers for improved efficiency using a CFD code. *1st International Conference From Scientific Computing to Computational Engineering*.

[11] Vlasogiannis, P., Karagiannis, G., Argyropoulos, P., Bontozoglou, V. (2002). Air–water two-phase flow and heat transfer in a plate heat exchanger. *International Journal of Multiphase Flow*, vol. 28, no. 5, p. 757–772, **DOI:10.1016/S0301-9322(02)00010-1**.

[12] Bellows, K.D. (1997). *Flow Visualization of Louvered-Fin Heat Exchangers*. University of Illinois, Urbana.

[13] Subbiah, M. (2012). The characteristics of brazed plate heat exchangers with different chevron angles. *Heat Exchangers – Basics Design Applications*, INTECH Open Access Publisher, Rijeka, **DOI:10.5772/32888**.

[14] Prasad, A.K., Jensen, K. (1995). Scheimpflug stereocamera for particle image velocimetry in liquid flows. *Applied Optics*, vol. 34, no. 30, p. 7092-7099, **DOI:10.1364/ao.34.007092**.

[15] Astarita, T. (2012). A Scheimpflug Camera Model for Stereoscopic and Tomographic PIV. *16th International Symposium on Applications of Laser Techniques to Fluid Mechanics*.

[16] Konrath, R. Schröder, W. (2002). Telecentric lenses for imaging in particle image velocimetry: a new stereoscopic approach. *Experiments in Fluids*, vol. 33, no. 5, p. 703-708, **DOI:10.1007/s00348-002-0531-7**.

[17] Agarwal, S., Mallick, S.P., Kriegman, D., Belongie, S. (2004). *On Refractive Optical Flow*. Computer Vision-ECCV, Springer, Berlin, Heidelberg, p. 483-494, **DOI:10.1007/978-3-540-24671-8_38**.

[18] Soloff, S.M., Adrian, R.J., Liu, Z.-C. (1997) Distortion compensation for generalized stereoscopic particle image velocimetry. *Measurement Scienceand Technolgy*, vol. 8, no. 12, p. 1441-1454.

[19] Willert, C.E. (2006). Assessment of camera models for use in planar velocimetry calibration. *Experiments in Fluids*, vol. 41, no. 1, p. 135-143, **DOI 10.1007/s00348-006-0165-2**.

[20] Claus, D., Fitzgibbon, A.W. (2005). A rational function lens distortion model for general cameras. *IEEE Computer Society Conference on Computer Vision and Pattern Recognition*, vol. 1, p. 213-219, **DOI:10.1109/CVPR.2005.43**.

[21] Krug, D., Holzner, M., Lüthi, B., Wolf, M., Tsinober, A., Kinzelbach, W. (2014). A combined scanning PTV/LIF technique to simultaneously measure the full velocity gradient

tensor and the 3D density field. *Measurement Science and Technology*, vol. 25, no. 6, p. 065301, **DOI:10.1088/0957-0233/25/6/065301**.

[22] Schanz, D., Gesemann, S., Schröder, A., Wieneke, B., Novara, M. (2013). Non-uniform optical transfer functions in particle imaging: calibration and application to tomographic reconstruction. *Measurement Science and . Technology*, vol. 24, no. 2, p. 024009, **DOI:10.1088/0957-0233/24/2/024009**.

[23] Wieneke, B. (2008). Volume self-calibration for 3D particle image velocimetry. *Experiments in Fluids*, vol. 45, no. 4, p. 549-556, **DOI:10.1007/s00348-008-0521-5**.

[24] Budwig, R. (1994). Refractive index matching methods for liquid flow investigations. *Experiments in Fluids*, vol. 17, no. 5, p. 350-355, **DOI:10.1007/BF01874416**.

[25] Hassan, Y. A., Dominguez-Ontiveros, E. E. (2008). Flow visualization in a pebble bed reactor experiment using PIV and refractive index matching techniques. *Nuclear Engineeringand Design*, vol. 238, no. 11, pp. 3080-3085, **DOI:10.1016/j.nucengdes.2008.01.027**.

[26] Adrian, R. J. (2005). Twenty years of particle image velocimetry. *Experiments in Fluids*, vol. 39, no. 2, p. 159-169, **DOI:10.1007/s00348-005-0991-7**.

[27] Pantzali, M.N., Kanaris, A.G., Antoniadis, K.D., Mouza, A.A., Paras, S.V. (2009). Effect of nanofluids on the performance of a miniature plate heat exchanger with modulated surface. *International Journal of Heat and Fluid Flow*, vol. 30, no. 4, p. 691-699, **DOI:10.1016/j.ijheatfluidflow.2009.02.005**.

[28] Ashburner, J., Friston, K.J. (1999). Nonlinear spatial normalization using basis functions. *Human Brain Mapping*, vol. 7, no. 4, p. 254-266, **DOI:10.1002/(SICI)1097-0193(1999)7:4<254::AID-HBM4>3.0.CO;2-G**.

Strojniški vestnik - Journal of Mechanical Engineering 62(2016)1, 11-20

DOI:10.5545/sv-jme.2015.2699 Original Scientific Paper
Received for review: 2015-05-22
Received revised form: 2015-09-14
Accepted for publication: 2015-11-09

Analysis of the Accuracy of Reconstructed Two Teeth Models Manufactured Using the 3DP and FDM Technologies

Grzegorz Budzik – Jan Burek – Anna Bazan – Paweł Turek
The Rzeszow University of Technology, Department of Mechanical Engineering, Poland

This paper presents results of the research focused on the accuracy of the manufacturing process of biomedical models, specifically tooth models. A patient's head was scanned with cone-beam computer tomography (CBCT). The best effect of tooth geometry reconstruction was obtained using the isotropic dimensions of voxel 0.2 mm × 0.2 mm × 0.2 mm. The same Hounsfield value was used (1254HU) and the method of segmentation (region growing) applied for the models of the teeth in the process of 3D reconstruction. The marching cubes algorithm, a method of surface rendering, allowed fully reconstructing the 3D geometry. The models were manufactured using two additive techniques (3DP and FDM). They were similarly aligned in the work space of both printers to maintain similar conditions of printing, and similar layer thicknesses of 0.1 mm and 0.13 mm were used. The printed models were scanned using a focus variation (FV) microscope. The scanned geometry of the models of the two teeth was compared with the geometry of the teeth after their segmentation and filtering. A fitting process was carried out using the best fit algorithm with a fitting condition of 0.001 mm. The achieved accuracy of the FV measurements was significantly higher than the accuracy of the used printing methods. FV can be applied to performing 3D scans of complex shapes such as the crown and roots of a tooth. 3DP models have more homogenous structure, whereas layer structure is easy to recognize for FDM models. Due to that, the 3DP models have to be strengthened using infiltration, which makes it more difficult to predict the final dimensions and to achieve required accuracy.

Keywords: dental model, reverse engineering, rapid prototyping, focus variation

Highlights

- *The accuracy of FDM and 3DP techniques were examined in terms of manufacturing dental models such as tooth models.*
- *The infiltration applied to the 3DP models reduced in accuracy compared to FDM models.*
- *For the FDM models, the values of mean deviation were negative and met the accuracy specified by the printer's manufacturer.*
- *Due to infiltration the values of mean deviation of 3DF models were positive.*
- *The infiltration also caused the models manufactured with the FDM to be more accurate than the 3DP ones.*
- *It was determined that the focus variation method can be applied to measure parts with a complex shape, such as the crown and roots of a tooth.*

0 INTRODUCTION

Traditional computer modelling is performed using CAD systems. Everything starts with a constructor idea. They present their concept on a technical drawing and then perform it in a virtual environment of a 3D model. This model may then be manufactured with the use of available methods. The problem arises when technical documentation of an object, for example, a tooth model, is not available.

2D images are the traditional way of presenting anatomical structures; unfortunately, this method is sometimes ineffective. In advanced cases of dental conditions, there are difficulties in the recognition and proper interpretation of 2D images of the affected area. This is why other ways to show the shape of the complex internal structures have been researched, such as the Marching Cube **[1]** and **[2]** and Splitting Box algorithm **[3]**. With the development of computer tomography systems, it has become possible to obtain volumetric data. Thanks to processing the volumetric data, a 3D computer model of a scanned part can be created as a result. Next, medical models can be manufactured using subtractive **[4]** or additive techniques **[5]** and **[6]**. Due to the complexity of the reconstruction process of medical models, the accuracy of an output model is dependent on a 3D scanning method, such as structure light **[7]**, MDCT **[8]** and **[9]**, CBCT **[10]** and **[11]**, and MRI systems **[12]**. Scientists also present work about a comparative evaluation of CBCT and MDCT at the stage of image reconstruction **[13]** and **[14]** and accuracy reconstruction 3D model **[15]**. The reconstruction process is also dependent on spatial and contrast resolution of computer tomography systems **[16]** and **[17]** method of segmentation **[18]** software algorithms **[19]** and **[20]**, and a manufacturing technology **[7]** and **[21]**.

Additive techniques are based on the incremental building of objects. They are the opposite of subtractive methods of manufacturing, often described as conventional, where an object is shaped via mechanical removal of material. Rapid prototyping (RP), i.e. additive manufacturing of physical models

*Corr. Author's Address: The Rzeszow University of Technology, Department of Mechanical Engineering, Poland, pturek@prz.edu.pl

[22] and [23] rapid tooling (RT) [24] and machining [25] are currently used to fabricate dental models. These models help a surgeon to diagnose, plan a treatment [26] and [27] and perform surgery [28] and [29].

In the field of biomedical applications, additive manufacturing (AM) has great advantages over subtractive methods when it comes to building intricate shapes matching human anatomy as well as constructing complex porous microstructures [30]. There is a broad variety of devices using the additive methods currently on the market. Each device has specific characteristics and requirements regarding material, environmental conditions, the temperature of the process, the and stage of the final model preparation. Due to the diversity of properties and the varied availability of the RP technologies, none of these dominates in the field of medical applications; this applies to dental surgery as well [25].

The RP technologies are open to new possibilities for the development of customized applications such as the manufacture of dental models. Scientists are still conducting research to obtain reasonable accuracy at the stage of processing 2D data [10] and [11], as well as to improve the quality of dental models manufactured using the RP [31] and [32],working on material properties [33] and to find an optimal measurement system for inspecting dimensions [34] and [35].

The purpose of this investigation is to analyse the accuracy of the models of two teeth manufactured with the use of different RP methods. Because 3D printing (3DP) and fused deposition modelling (FDM) are one of the most widely used RP methods, as well as due to the relatively low cost of these processes, they were chosen for this research.

An additional aim of this paper is to evaluate a focus variation (FV) microscope as a measuring system for inspecting small parts with complex geometry, such as dental models.

1 METHOD

Three-dimensional computer models of 2 teeth were obtained by scanning the patient's mandible with the cone beam computer topography method and subsequent segmenting the teeth from measured data. After performing geometry reconstruction, the models were printed using the two RP methods, i.e. FDM and 3DP. Next the printed models were measured using an FV microscope. The measured geometries of the models of the two teeth were compared with geometries of the teeth after their segmentation and filtering.

1.1 Reconstruction of Geometries of the Teeth from DICOM Data

All measurements of the mandible were made with a cone bean computer tomography system - Gendex CB500 3D by a medical partner. The maximum resolution of Gendex is 0.125 mm; however, parameters are set up for each patient individually. Table 1 presents parameters used during the measurements. To minimize artefacts associated with discontinuous interpolation, the isostructure of the voxel (0.2 mm × 0.2 mm × 0.2 mm) was used. The obtained data included a stack of individual images. Each image represented a thin slice of the scanned body part and was composed of individual pixels. Those pixels were arranged on a two-dimensional grid.

The scanned data of the patient's mandible obtained using the cone-beam computed tomography (CBCT) and stored as images in the digital imaging and communications in the medicine (DICOM) format were subsequently processed in software 3D Doctor to reconstruct the geometry of the two separated teeth.

Table 1. *Parameters used in measurements with Gendex CB500 3D*

Parameter	Value/Type
Voxel size	0.2 mm × 0.2 mm × 0.2 mm
Type of sensor	Amorphous silicon flat panel
Line of Pairs	14 lp/cm
Grayscale (BIT)	14 bit
Shades of grey	16384 shades of grey
Field of view	8 cm × 8 cm – standard mode
Scan times	23 s

To increase accuracy, the images were subjected to filtration, reducing noisy and blurred edges. Noise reduction and sharpening parameters were chosen empirically to obtain the best results.

To separate a tooth from the mandible, a region-growing algorithm was used. The region-growing algorithm allows to select pixels with similar Hounsfield units (HU) and classify them into a group defining the given tissue [18]. The threshold value was set above 1254HU to select only the tissue that represented a segmented tooth.

After the 3D image was segmented, i.e. after every voxel was assigned to some material, a polygonal surface model was created. To reconstruct the surface, the marching cubes algorithm was used

[1] and [2] (Fig. 1). This algorithm guarantees that the resulting surfaces are free from cracks and holes, that no facet (single surface build on three nearest points) intersects one another, and that all regions assigned to different materials are well separated from one another. A disadvantage of this technique is that small details of a segmented data set may be lost.

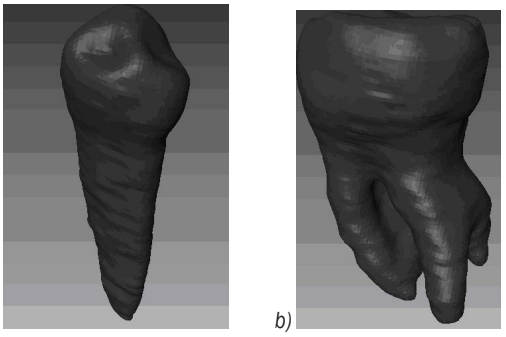

Fig. 1. *Tooth models reconstructed from the DICOM data: a) tooth 1, b) tooth 2*

1.2 Manufacturing Models of the 2 Teeth Using Rapid Prototyping Technologies

The models were manufactured using the two rapid prototyping technologies: FDM and 3DP. These methods are cheaper than others used in the dental industry such as PolyJet or SLS. Furthermore, the accuracy of FDM models is comparable to those of PolyJet or SLS. FDM and 3DP were also chosen for the reason of testing an FV microscope as a measuring system for printed models. The authors were curious about the results of measuring white powder and white/cream plastic, which are materials with different optical properties.

FDM is the most widely used additive technique in manufacturing medical replicas after stereolithography [21]. An FDM model is built of thin layers of thermoplastic wire similar to filaments (Fig. 2a). Filaments of heated thermoplastic wire are extruded from a tip that moves in the *xy*-plane. The platform is maintained at a lower temperature so that the thermoplastic hardens quickly. After the platform descends, an extrusion head deposits a second layer on the first. Along the way, support is built and fastened to a printed part either with a second, weaker material or with a perforated linkage. Support structures are fabricated for overhanging geometries and are later removed by breaking them away from the object. A water-soluble support material that can be easily washed away is also available. Several types of materials are available for building models, e.g. acrylonitrile butadiene styrene (ABS) which offers good strength, or polycarbonate and polysulfide materials that have recently increased the capability of the FDM method in terms of strength and temperature range. The advantage of the FDM method is that there is no need for untidy liquid photopolymers, powders and lasers [36].

A 3D printing system uses print heads to selectively disperse a binder onto powder layers (Fig. 2b). A thin layer of powder is spread over a tray with a roller. A print head scans the powder tray and delivers continuous jets of a solution that binds powder particles (mostly gypsum powder) as it touches them. After one layer of a model is built, the powder bed is lowered, and the next layer of powder is spread. No support structure is required while a prototype is fabricated because surrounding powder supports unconnected parts. When the process is completed, the surrounding powder is aspirated.

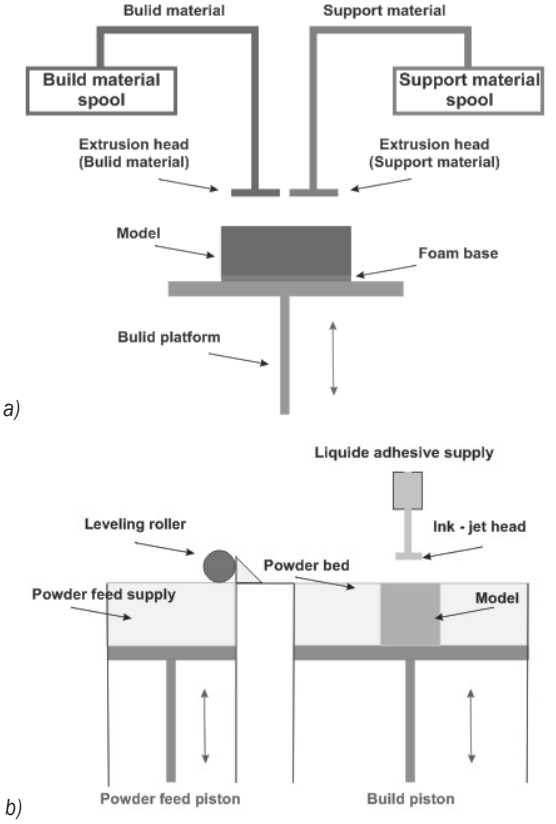

Fig. 2. *a) FDM technology diagram b) 3D printing technology (3DP) diagram*

In the finishing process, prototype surfaces are infiltrated with epoxy resin or a salt solution to harden

the structure. An advantage of the 3DP technology is the low cost of a printed model [36].

The sets of the process parameters used to manufacture the models of the two teeth are presented in Table 2. In both the printers, the models were similarly aligned in the work space to maintain similar conditions of production.

Table 2. *Parameters used in manufacturing the models of the 2 teeth*

FDM	Printer	Fortus 360 mc
	Accuracy (p = 99.7%)	Parts are produced with the accuracy of ± 0.2 mm [37]
	Material	ABS
	Layer thickness	0.127 mm
	Manufacturing time	Tooth 1 to 15 min Tooth 2 to 30 min
3DP	Printer	ZPrinter 650
	Accuracy (p = 99.7%)	Parts are produced with the accuracy of ± 0.18 mm (with no infiltration) [38]
	Material	gypsum powder
	Infiltrating material	epoxy resin
	Layer thickness	mm
	Manufacturing time	Tooth 1 to 20 min Tooth 2 to 35 min

1.3 Measurement of the Printed Models

Measurements of the printed elements were carried out using the Alicona InfiniteFocus microscope based on a measurement method called FV. The operating principle of an FV microscope combines the small depth of focus of the optical system with the vertical scanning of a specimen.

Focus variation is an area-based method in which many points are measured with one vertical scan. In the FV method, information on image sharpness of a measured surface is used to determine surface height as a function of position (x, y) [39] and [40].

The construction and operating principle of an FV microscope are shown in Fig. 3. The optical system is moved in the vertical direction along the optical axis in the range in which all points of a scanned surface are shown as sharp. In certain positions from this range, white light, emitted by a light source, is delivered through a semi-transparent mirror and lenses and illuminates the sample. The light reflected by the scanned surface is projected through the semi-transparent mirror and the lenses to a charge-coupled device (CCD) sensor. During the vertical movement of the optical system, contrast on the CCD sensor is changing relative to the change of focus. A contrast curve is calculated for every lateral position (pixel) on the CCD sensor and for the whole vertical scanning range. With the contrast curve, the Z position where the sample was in focus can be determined (Fig. 4). This allows to relate the vertical position of the optical system to Z coordinates of the points on the scanned surface [41].

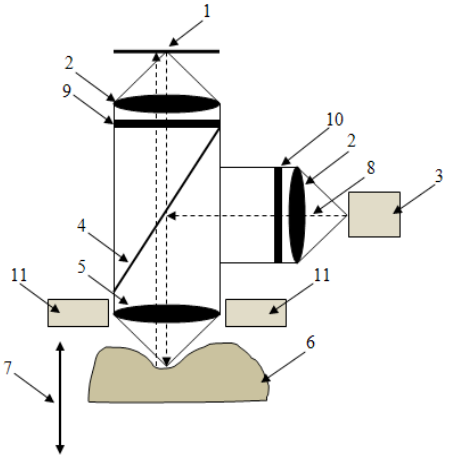

Fig. 3. *Diagram of the focus variation scanning method: 1 CCD sensor, 2 lenses, 3 white light source, 4 semi-transparent mirror, 5 objective lens with limited depth of field, 6 sample, 7 vertical movement with a driving unit, 8 light rays from the white light source, 9 optional analyzer, 10 optional polarizer and 11 optional ring light*

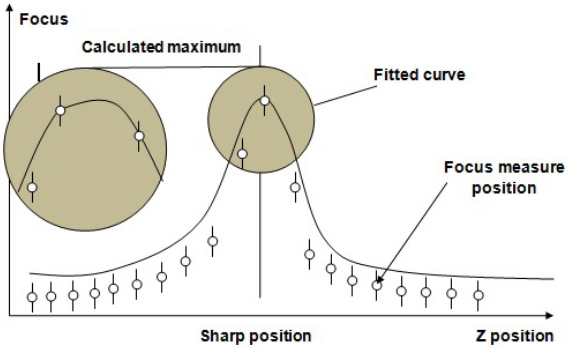

Fig. 4. *Change of focus with respect to Z position*

For each vertical position of the optical system, several scans of contrast are carried out. Consequently, it is possible to calculate the repeatability of measurement for each point. Due to the complexity of the geometry of the measured models, they were scanned in parts. The FDM and 3DP models of Tooth 1 were scanned in two parts – side surface and top surface (Fig. 5), and Tooth 2 models were scanned in three parts – side surface, top surface, and roots (Fig. 6).

In the case of an FV microscope, there are several objectives with different magnification capabilities that can be used. For each objective, a specific range

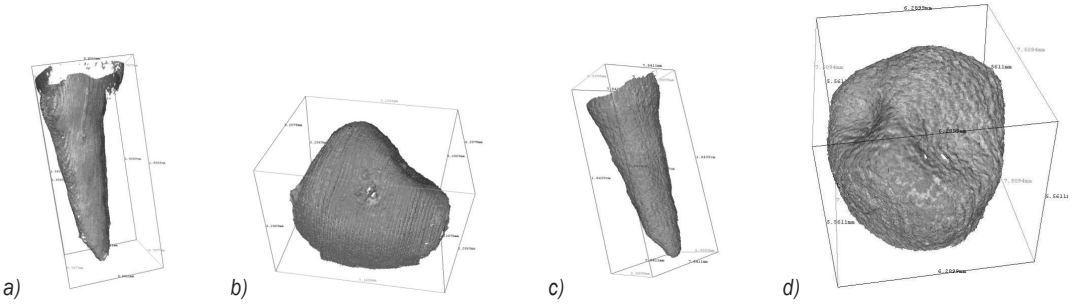

Fig. 5. *Scanned point clouds of the FDM model of the tooth 1: a) side surface, b) top surface, and of the 3DP model of the tooth 1: c) side surface, d) top surface*

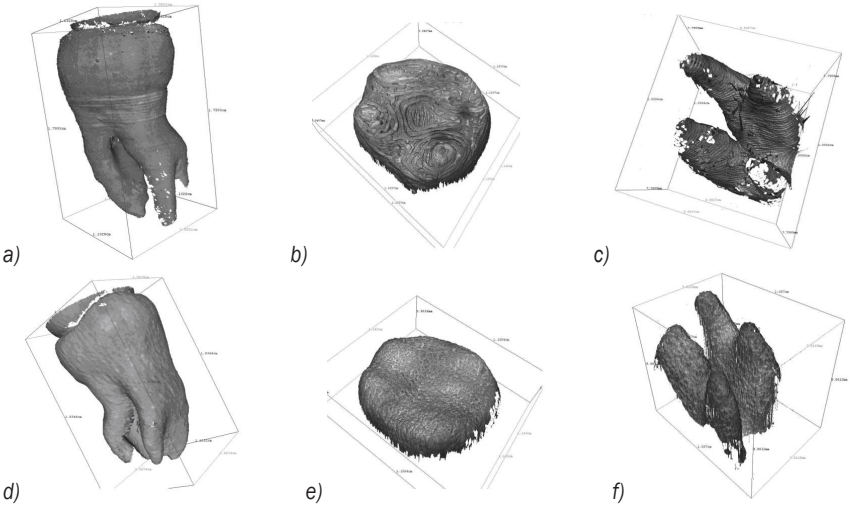

Fig. 6. *Scanned point clouds of the FDM model of the tooth 2: a) side surface, b) top surface c) roots, and of the 3DP model of the tooth 2: a) side surface, b) top surface c) roots*

of vertical and lateral resolution can be set. Each objective is also characterized by the field of view. Additionally, the distance between the objective lens and a measured surface varies for each objective; the higher magnification, the smaller the distance between the lens and a sample. In the studied case, where complex geometry was measured, especially for the roots and the side surface of Tooth 2, it was essential to choose an objective for which the working distance would be long enough to avoid collision during the measurement. This is why the 2.5× objective was chosen. The vertical resolution for this objective can be set in the range from 2.3 μm to 132.51 μm, and the lateral resolution from 6.92 μm to 58.71 μm.

During the research, several sets of resolutions' values were used at testing stage. The set that offers the best quality was chosen for the final measurements. Measurement settings (i.e. vertical and lateral resolution) for each scan are presented in Table 3. Information regarding the repeatability of measurements of the tooth 1 and the tooth 2 are shown in Table 4.

Table 3. *Infinite focus scan setting*

Tooth	Scanned part	Vertical resolution [μm]	Lateral resolution [μm]
Tooth 1	side surface	15.5	19.57
Tooth 1	top surface	15.5	19.57
Tooth 2	side surface	26.76	27.86
Tooth 2	top surface	15.22	19.57
Tooth 2	Roots	7.08	16.27

Scanned geometries of the models of the 2 teeth were compared with the geometries of the teeth after their segmentation and filtering. The fitting process was carried out using the best fit algorithm with a fitting condition of 0.001 mm.

Table 4. *Repeatability information of scanned point clouds*

Scanned part		FDM			3DP		
		Repeatability threshold [μm]	Mean repeatability [μm]	Median repeatability [μm]	Repeatability threshold [μm]	Mean repeatability [μm]	Median repeatability [μm]
Tooth 1	side surface	5.39	2.32	2.13	1.63	0.59	0.51
	top surface	11.5	3.39	1.87	10.02	1.47	1.07
Tooth 2	side surface	7.75	3.0	2.43	2.33	0.44	0.33
	top surface	59.1	9.21	4.01	29.8	8.89	3.62
	roots	76.6	11.9	5.8	13.2	3.23	1.96

Table 5. *Results of comparison between the CAD models reconstructed from the DICOM data and the printed models (Tooth 1)*

	Tooth 1 (FDM)		Tooth 1 (3DP)	
Part	Mean deviation [μm]	SD [μm]	Mean deviation [μm]	SD [μm]
side surface	-25	59	41	129
top surface	-59	47	145	80
assembly	-43	30	98	68

side surface

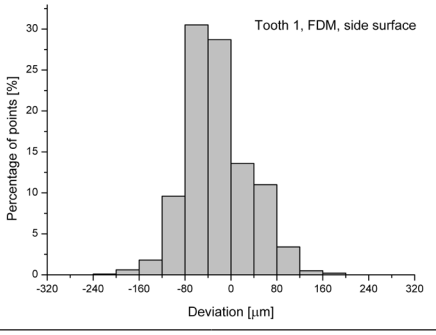

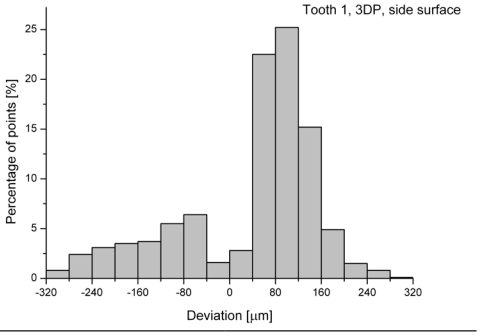

top surface

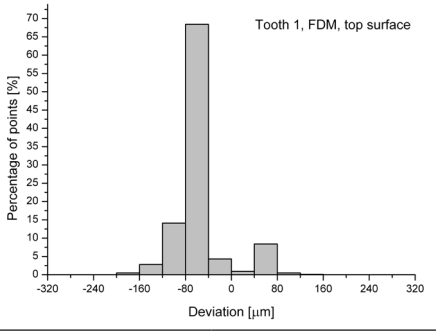

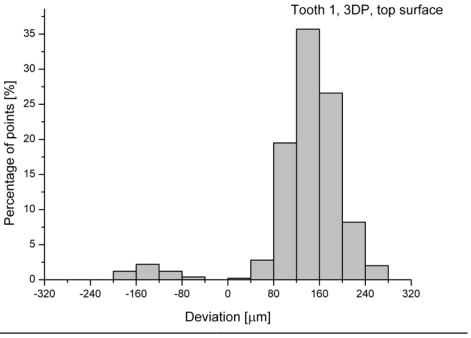

assembly

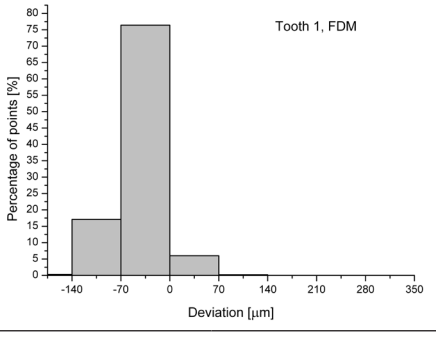

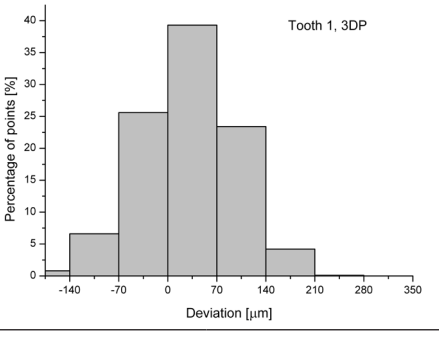

The comparison was made for all the scanned parts of the teeth as well as for the scanned parts assembled into complete tooth geometries. The assembly and the process of comparison were made using Focus Inspection software. As a result, the deviation for each point was calculated. Values

of mean deviation of an inspected part, standard deviation (SD) for these values, and distribution of deviations of the printed models are shown in Table 5 for Tooth 1 and in Table 6 for Tooth 2.

3 RESULTS AND DISCUSSION

The models of the two teeth manufactured using the FDM and 3DP technologies were compared with their CAD models to examine their accuracy. Basic statistics (mean value and *SD*) and distributions of the printed models are gathered in Tables 5 and 6.

The accuracy of the fabricated models was influenced by errors of scanning, manufacturing, and the best-fit algorithm used.

Repeatability (Table 4) is the standard deviation of a series of the same measurements. Knowing the vertical resolution (Table 3) and the mean repeatability of scanning, it is possible to calculate a confidence interval at a specific level of significance. The confidence interval reflects the quality of scanning. The smaller the confidence interval, the better measurement.

The smallest 95 % confidence interval was calculated for the 3DP side surface, and it equalled to ±9 μm. The biggest 95 % confidence intervals were calculated for the FDM roots, the FDM top surface, and the 3DP top surface and they were ±27 μm, ±26 μm, and ±25 μm respectively.

Comparing the values of scanning resolutions and the scanning mean repeatability with the distributions of models' deviations, it can be assumed that measurement errors have negligible influence on the results. The values of deviations far more exceed the scanning confidence intervals.

For all the inspected parts of the models of the two teeth and for the complete models, values of mean deviation were negative for FDM and positive for 3DP. In every case, except roots, the absolute value of the mean deviation was significantly higher for the 3DP models than for the FDM models. Higher and positive values of the 3DP models' deviations were caused by infiltration of the models with an epoxy resin that increased their dimensions.

For all the parts and the complete models, the standard deviation of the deviations' values was also much bigger for the 3DP than the FDM.

For the top surface and roots of the Tooth 2 models manufactured using the FDM and the 3DP, and the side surface of the FDM model of Tooth 2, a bimodal distribution of the deviations could be recognized. To perform the evaluation of these parts, each original distribution was separated into two distributions using the peak fit function available in OriginPro 9.1. The mean value and the standard deviation of the components are presented in Table 7.

For all the above-mentioned parts, it can be observed that one mean value of components' distributions is positive and the second is negative, and the modes are symmetrical with respect to 0. Also in each case, the antimode is near 0. It can be then assumed that the observed bimodal distributions are composed of distributions of the positive and negative deviations. That implicates low and similar values of mean deviation when the distributions are evaluated as unimodal (Table 6).

The observed bimodality may indicate an error during the fitting process, specifically the rotation/translation of the measured models with respect to nominal shape (reconstructed CAD models).

All the calculated statistics of the components are significantly smaller for the FDM models than for the 3DP ones, as was previously observed for all unimodal distributions.

The values of mean deviations for the assemblies are approximately equal to the mean values calculated from the mean deviations of the scanned parts. Standard deviations for the assemblies are lower than the SD of the single parts, except the side surface of Tooth 2 manufactured with the 3DP. The greater number of points in the assemblies' files allowed for a better fit to nominal, that is to CAD models.

It can be stated that FDM models are manufactured with the accuracy specified by the printer's manufacturer (Table 2). In the case of the 3DP models, there is a lack of information on model accuracy after the infiltration. That is why the comparison with the data presented by the 3D printer's manufacturer cannot be made.

4 CONCLUSIONS

The geometry of patient's tooth crowns and roots can be obtained by scanning the patient's mandible using CBCT. At the stage of acquiring and processing the data to create a 3D CAD model of a tooth, the voxel size and the Hounsfield value are the most significant parameters. The 3D CAD model saved as the standard template library (STL) file can be used to fabricate a physical model by one of the additive techniques.

This paper asserts that small complex models, such as the crown and roots of a tooth, can be manufactured using the 3DP and FDM technologies. The fabricated models were examined in terms of their accuracy. They were compared with their CAD models, and that is why their accuracy is the result of

Table 6. *Results of comparison between the CAD models reconstructed from the DICOM data and the printed models (Tooth 2)*

	Tooth 2 (FDM)		Tooth 2 (3DP)	
Part	Mean deviation [μm]	*SD* [μm]	Mean deviation [μm]	*SD* [μm]
side surface	-30	67	137	101
top surface	-8	82	77	135
roots	-10	83	11	168
assembly	-11	58	71	111

side surface

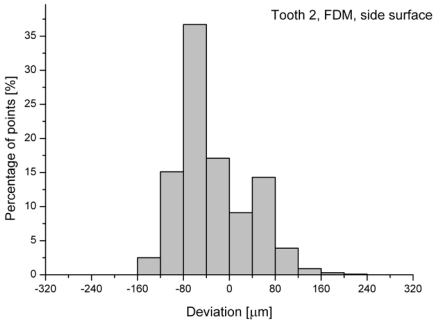

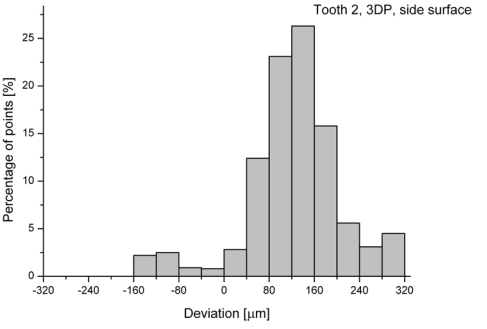

top surface

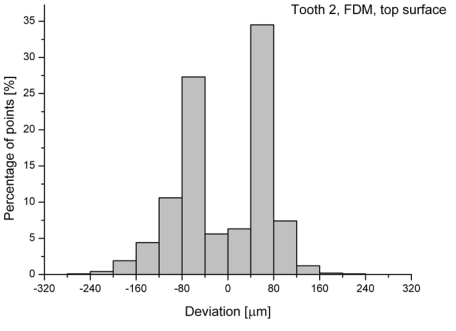

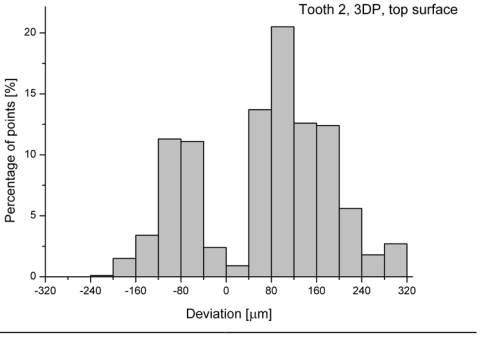

roots

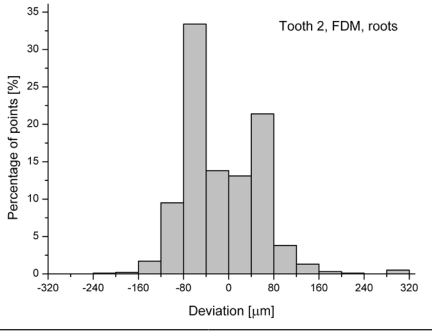

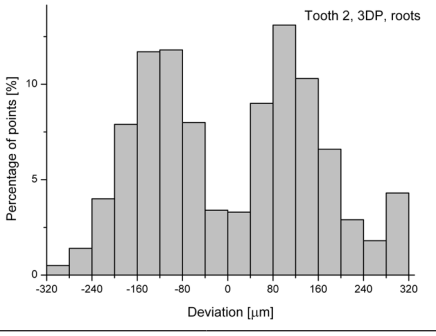

assembly

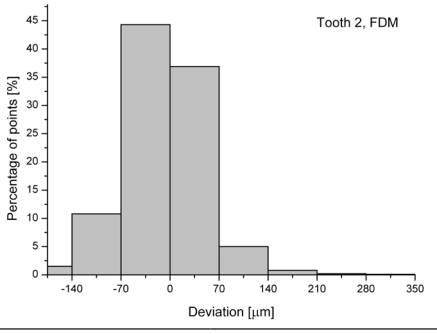

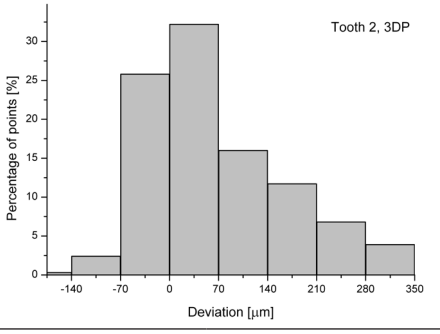

errors of scanning, manufacturing, and the used best-fit algorithm.

Recognizable errors during the fitting process occurred especially in the case of the top surface and

Table 7. *Statistics of components' evaluated bimodal distributions*

Part	Tooth 2 (FDM)				Tooth 2 (3DP)			
	Mean 1 [μm]	*SD* 1 [μm]	Mean 2 [μm]	*SD* 2 [μm]	Mean 1 [μm]	*SD* 1 [μm]	Mean 2 [μm]	*SD* 2 [μm]
side surface	-59	31	52	29	-	-	-	-
top surface	-65	25	61	21	-82	29	116	57
roots	-56	27	49	26	-120	52	109	49

the roots of the Tooth 2 models. Better fitting results were achieved for the assemblies rather than for the separate parts.

Upon comparing the mean deviations and their standard deviations, it can be concluded that the models manufactured with the FDM are more accurate than the 3DP ones. This is caused by the infiltration applied to the 3DP models. To be able to predict final dimensions and meet required accuracy of the 3DP models, it would be necessary to carry out further studies.

The focus variation method can be applied to measure parts with a complex shape, such as the crown and roots of a tooth. The achieved accuracy of measurement is significantly higher than the accuracy of the printing methods used. This means that measurement errors can be regarded as negligible. The focus variation method can be an alternative to the current measurement methods that are used in case of relatively small and complex dental models.

5 REFERENCES

[1] Lorensen, W., Cline, H. (1987). Marching cubes: a high resolution 3D surface construction. *ACM SIGGRAPH Computer Graphics*, vol. 21, no. 4, p. 163-169, **DOI:10.1145/37402.37422**.

[2] Newman, T.S., Yi, H. (2006). A survey of the marching cubes algorithm. *Computers & Graphics*, vol. 30, no. 5, p. 854-879, **DOI:10.1016/j.cag.2006.07.021**.

[3] Preim, B., Bartz, D. (2007). *Visualization in Medicine: Theory, Algorithms, and Applications*. Morgan Kaufmann Publishers Inc., San Francisco.

[4] Budzik, G., Burek, J., Dziubek, T., Gdula, M., Płodzień, M., Turek, P. (2015). The analysis of accuracy zygomatic bone model manufactured by 5-axis HSC 55 linear. *Mechanik*, vol. 88. (in Polish)

[5] Markowska, O., Budzik, G. (2012). Innovative methods of manufacturing bone implants using the reverse engineering (RE) and the rapid prototyping (RP) techniques. *Mechanik*, vol. 85. (in Polish)

[6] Salmi, M., Paloheimo, K.S., Tuomi, J., Wolff, J., Mäkitie, A. (2013). Accuracy of medical models made by additive manufacturing (rapid manufacturing). *Journal of Cranio-Maxillo-Facial* Surgery, vol. 41, no. 7, p. 603-609, **DOI:10.1016/j.jcms.2012.11.041**.

[7] Budzik, G., Burek, J., Dziubek, T., Markowska, O., Turek, P., Pakla, P. (2014). Applications of rapid prototyping technology in the craniofacial surgery. *12th Conference Mechanics in Medicine*, p. 16-29.

[8] Ryniewicz, A. (2010). Accuracy assessment of shape mapping using computer tomography. *Metrology and Measurement Systems*, vol. 17, no. 3, p. 481-492, **DOI:10.2478/v10178-010-0040-6**.

[9] Nizam, A., Gopal, R.N., Naing, L., Hakim, A.B., Samsudin, A.R. (2006). Dimensional accuracy of the skull models produced by rapid prototyping technology using stereolithography apparatus. *Archives of Orofacial Sciences*, vol. 1, p. 60-66.

[10] Ye, N., Jian, F., Xue, J., Wang, S., Liao, L., Huang, W., Yang, X., Zhou, Y., Lai, W., Li, J., Wang, J. (2012). Accuracy of in-vitro tooth volumetric measurements from cone-beam computed tomography. *American Journal of Orthodontics and Dentofacial Orthopedics*, vol. 142, no. 6, p. 879-887, **DOI:10.1016/j.ajodo.2012.05.020**.

[11] Maret, D., Telmon, N., Peters, O.A., Lepage, B., Treil, J., Inglèse, J.M., Peyre, A., Kahn, J.L., Sixou, M. (2012). Effect of voxel size on the accuracy of 3D reconstructions with cone beam CT. *Dentomaxillofacial Radiology*, vol. 41, no. 8, p. 649-655, **DOI:10.1259/dmf/81804525**.

[12] Huotilainen, E., Paloheimo, M., Salmi, M., Paloheimo, K. S., Björkstrand, R., Tuomi, J., Mäkitie, A. (2013). Imaging requirements for medical applications of additive manufacturing. *Acta Radiologica*, vol 55, no. 1, p. 78-85, **DOI:10.1177/0284185113494198**.

[13] Kim, M., Huh, K.H., YI, W.J., Heo, M.S., Lee, S.S., Choi, S.Ch. (2012). Evaluation of accuracy of 3D reconstruction images using multi-detector CT and cone-beam CT. *Imaging Science in Dentistry*, vol. 42, no. 1, p. 25-33, **DOI:10.5624/isd.2012.42.1.25**.

[14] Liang, X., Jacobs, R., Hassan, B., Li, L., Pauwels, R., Corpas, L., Souza, P.C., Martens, W., Shahbazian, M., Alonso, A., Lambrichts, I. (2010). A comparative evaluation of cone beam computed tomography (CBCT) and multi-slice CT (MSCT) Part I. On subjective image quality. *European Journal of Radiology*, vol. 75, no. 2, p. 265-269, **DOI:10.1016/j.ejrad.2009.03.042**.

[15] Liang, X., Lambrichts, I., Sun, Y., Denis, K., Hassan, B., Li, L., Pauwels, R., Jacobs, R. (2010). A comparative evaluation of cone beam computed tomography (CBCT) and multi-slice CT (MSCT). Part II: On 3D model accuracy. *European Journal of Radiology*, vol. 75, no. 2, p. 270-274, **DOI:10.1016/j.ejrad.2009.04.016**.

[16] Alsleem, H., Davidson, R. (2013). Factors affecting contrast-detail performance in computed tomography: A review. *Journal of Medical Imaging and Radiation Sciences*, vol. 44, no. 2, p. 62-70, **DOI:10.1016/j.jmir.2012.12.001**.

[17] Romans, L. (2011). *Computed Tomography for Technologists: A Comprehensive Text*. Wolters Kluwer Health, Lippincott Williams & Wilkins, Baltimore.

[18] Cerrolaza, M., Gavidia, G., Soudah, E., Martín-Landrove, M. (2014). Modeling human tissue: An efficient integrated methodology. *Biomedical Engineering: Applications, Basis and Communications*, vol. 26, no. 1, **DOI:10.4015/S1016237214500124**.

[19] Vera, V., Corchado, E., Redondo, R., Sedano, J., García, Á.E. (2013). Applying soft computing techniques to optimise a dental milling process. *Neurocomputing*, vol. 109, p. 94-104, **DOI:10.1016/j.neucom.2012.04.033**.

[20] Huotilainen, E., Jaanimets, R., Valášek, J., Marcián, P., Salmi, M., Tuomi, J., Mäkitie, A., Wolff, J. (2014). Inaccuracies in additive manufactured medical skull models caused by the DICOM to STL conversion process. *Journal of Cranio-Maxillofacial Surgery*, vol. 42, no. 5, p. e259-e265, **DOI:10.1016/j.jcms.2013.10.001**.

[21] El-Katatny, I., Masood, S.H., Morsi, Y.S. (2010). Error analysis of FDM fabricated medical replicas. *Rapid Prototyping Journal*, vol. 16, no. 1, p. 36-43, **DOI:10.1108/13552541011011695**.

[22] Lambrecht, J.Th., Berndt, D.C., Schumacher, R., Zehnder, M. (2009). Generation of three-dimensional prototype models based on cone beam computed tomography. *International Journal of Computer Assisted Radiology and Surgery*, vol. 4, no. 2, p. 175-180, **DOI:10.1007/s11548-008-0275-9**.

[23] Salmi, M., Paloheimo, K. S., Tuomi, J., Ingman, T., Mäkitie, A. (2013). A digital process for additive manufacturing of occlusal splints: a clinical pilot study. *Journal of the Royal Society Interface*, vol. 10, no. 84, **DOI:10.1098/rsif.2013.0203**.

[24] Salmi, M., Tuomi, J., Sirkkanen, R., Ingman, T., Mäkitie, A. (2012). Rapid tooling method for soft customized removable oral appliances. *The Open Dentistry Journal*, vol. 6, p. 85-89, **DOI:10.2174/1874210601206010085**.

[25] Martorelli, M., Gerbino, S., Giudice, M., Ausiello, P. (2013). A comparison between customized clear and removable orthodontic appliances manufactured using RP and CNC techniques. *Dental Materials*, vol. 29, no. 2, p. e1-e10, **DOI:10.1016/j.dental.2012.10.011**.

[26] Figliuzzi, M., Mangano, F., Mangano, C. (2012). A novel root analogue dental implant using CT scan and CAD/CAM: selective laser melting technology. *International Journal of Oral and Maxillofacial Surgery*, vol. 41, no. 7, p. 858-862, **DOI:10.1016/j.ijom.2012.01.014**.

[27] Papaspyridakos, P., Lal, K. (2008). Complete arch implant rehabilitation using subtractive rapid prototyping and porcelain fused to zirconia prosthesis: A clinical report. *The Journal of Prosthetic Dentistry*, vol. 100, no. 3, p. 165-172, **DOI:10.1016/S0022-3913(08)00110-8**.

[28] Lee, J.H. (2014). Accelerated techniques for a post and core and a crown restoration with intraoral digital scanners and CAD/CAM and rapid prototyping. *Journal of Prosthetic Dentistry*, vol. 112, no. 5, p. 1024-1029, **DOI:10.1016/j.prosdent.2014.04.019**.

[29] Tuomi, J., Paloheimo, K.S., Vehviläinen, J., Björkstrand, R., Salmi, M., Huotilainen, E., Mäkitie, A.A. (2014). A novel classification and online platform for planning and documentation of medical applications of additive manufacturing. *Surgical Innovation*, vol. 21, no. 6, p. 553-559, **DOI:10.1177/1553350614524838**.

[30] Beaman, J.J., Atwood, C., Bergman, T.L., Bourell, D., Hollister, S., Rosen, D. (2004) *Additive/subtractive manufacturing research and development in Europe*. Final report by World Technology Evaluation Center, p. 55-62.

[31] Hazeveld, A., Slater, J.J.H., Ren, Y. (2014). Accuracy and reproducibility of dental replica models reconstructed by different rapid prototyping techniques. *American Journal of Orthodontics and Dentofacial Orthopedics*, vol. 145, no. 1, p. 108-115, **DOI:10.1016/j.ajodo.2013.05.011**.

[32] Reyes, A., Turkyilmaz, I., Prihoda, T.J. (2015). Accuracy of surgical guides made from conventional and a combination of digital scanning and rapid prototyping techniques. *The Journal of Prosthetic Dentistry*, vol. 113, no. 4, p. 295-303, **DOI:10.1016/j.prosdent.2014.09.018**.

[33] Baloš, S., Milutinović, M., Potran, M., Vuletić, J., Puškar, T., Pepelnjak, T. (2015). The mechanical properties of moulded and thermoformed denture resins. *Strojniški vestnik - Journal of Mechanical Engineering*, vol. 61, no. 2, p. 138-145, **DOI:10.5545/sv-jme.2014.2249**.

[34] Budak, I., Trifkovic, B., Puskar, T., Vukelic, D., Vucaj-Cirilovic, V., Hodolic, J., Todorovic, A. (2013). Comparative analysis of 3D digitization systems in the field of dental prosthetics. *Technical Gazette - Tehnički vjesnik*, vol. 20, no. 2, p. 291-296.

[35] Flügge, T.V., Schlager, S., Nelson, K., Nahles, S., Metzger, M.C. (2013). Precision of intraoral digital dental impressions with iTero and extraoral digitization with the iTero and a model scanner. *American Journal of Orthodontics and Dentofacial Orthopedics*, vol. 144, no. 3 , p. 471-479, **DOI:10.1016/j.ajodo.2013.04.017**.

[36] Hollister, S.J. (2005). Porous scaffold design for tissue engineering. *Nature Materials*, vol. 7, no. 4, p. 518-24, **DOI:10.1038/nmat1421**.

[37] Hanssen J., (2013), FORTUS 360mc/400mc ACCURACY STUDY, from *http://www.stratasys.com/* accessed on 2013-03-18.

[38] ZPrinter Materials and Accuracy. (2011). Functional Performance and Accuracy of 3D Printed Models, from *http://www.3d-sourcegraphics.com/* accessed on 2011-06-02

[39] Danzl, R., Helmli, F., Scherer, S. (2011). Focus variation – a robust technology for high resolution optical 3D surface metrology. *Strojniški vestnik - Journal of Mechanical Engineering*, vol. 57, no. 3, p. 245-256, **DOI:10.5545/sv-jme.2010.175**.

[40] Giusca, C., Claverley, J., Sun, W., Leach, R.K., Helmli, F., Chavigner M.P.J. (2014). Practical estimation of measurement noise and flatness deviation on focus variation microscopes. *CIRP Annals - Manufacturing Technology*, vol. 63, no. 1, p. 545-548, **DOI:10.1016/j.cirp.2014.03.086**.

[41] Helmli, F. (2011). Focus variation instruments. Leach, R. (ed.) *Optical Measurement of Surface Topography*. Springer, Berlin, Heidelberg, p. 131-166, **DOI:10.1007/978-3-642-12012-1**.

Strojniški vestnik - Journal of Mechanical Engineering 62(2016)1, 21-31

DOI:10.5545/sv-jme.2015.2859
Original Scientific Paper
Received for review: 2015-07-10
Received revised form: 2015-09-18
Accepted for publication: 2015-10-08

Investigation of Rotor-Stator Interaction and Flow Unsteadiness in a Low Specific Speed Centrifugal Pump

Ning Zhang* – Minguan Yang – Bo Gao – Zhong Li – Dan Ni
Jiangsu University, School of Energy and Power Engineering, China

Instantaneous flow dynamics induced by rotor-stator interaction are detrimental to the stable operation of centrifugal pumps. In this study, unsteady rotor-stator interaction and flow structures within a low specific-speed centrifugal pump are analysed using the Large Eddy Simulation (LES) method. For that purpose, pressure pulsations and the evolution processes of vortical structures are combined to investigate rotor-stator interaction in order to clarify the inherent correlation between pressure amplitude and vorticity distribution. The results show that distinct peaks at blade passing frequency (f_{BPF}) are closely associated with the positions of the monitoring point due to rotor-stator interaction. An unsteady vortical structure at the near tongue region is related to the relative position of the impeller with respect to the tongue, and the upstream effect of the volute tongue significantly affects the vorticity distribution on the blade pressure side. Rotor-stator interaction is dominated by vortex shedding in the wake of the blade trailing edge and their impingement on the volute tongue with subsequent cutting and distortion. Moreover, the high-pressure amplitude is generated with the corresponding high vorticity magnitude observed as well. Therefore, it is confirmed that pressure amplitude is significantly associated with the corresponding vorticity magnitude.

Keywords: centrifugal pump, large eddy simulation, flow unsteadiness, rotor-stator interaction, pressure pulsation, vortical structure

Highlights

- *Numerical investigation of rotor-stator interaction and flow unsteadiness in a centrifugal pump.*
- *Vortical structure within the pump and its shedding from the blade trailing edge.*
- *Evolutionary process of vortical structure at the near tongue region.*
- *Correlation between pressure amplitude and vortical structure.*

0 INTRODUCTION

Unsteady pressure pulsation due to fluid-structure interaction significantly affects the stable and safe operation of the centrifugal pump. Due to the intense rotor-stator interaction between the impeller and the volute, severe vibration can be generated causing some unexpected damage to the mechanical components, for instance, the bearing and seal of the pump [1]. Some studies have been carried out to investigate unsteady rotor-stator interaction, either by the numerical or experimental method, but most of them only focus on the unsteady pressure pulsation at blade passing frequency (f_{BPF}) [2] and [3]. According to the classic theory, it is well known that flow discharged from the impeller exit, showing a jet-wake pattern, has a significant impact on rotor-stator interaction in centrifugal pumps, as well as to the unsteady pressure pulsation characteristics [4] and [5]. Therefore, it is essential to analyse unsteady flow structure, especially vorticity distribution within the pump, to clarify the influence of wake dynamics shedding from the blade trailing edge on pressure pulsations.

Posa et al. [6] and [7] numerically investigated unsteady flow distribution in a mixed flow pump using LES, especially the instantaneous vorticity distribution, and numerical results were validated with experiments. As for rotor-stator interaction, many studies only concentrate on distinct peaks in pressure spectra, especially pressure amplitude at f_{BPF}. Parrondo et al. [8] analysed pressure pulsations in a centrifugal pump for various conditions, and particular emphasis was placed on pressure amplitude at f_{BPF}. With the development of non-contact and nonintrusive measuring techniques in recent years, unsteady particle image velocimetry (PIV) and laser Doppler velocimetry (LDV) measuring techniques are often applied to investigate complex rotor-stator interaction in pumps so that no external disturbance would be imposed on the flow field. Keller et al. [9] used PIV to analyse unsteady flow field around the near tongue region at high flow rates, and consecutive contours of vorticity sheet shedding in the wake of the blade trailing edge were attained to observe the details of flow evolution at the tongue region. Wu et al. [10] and [11] also applied the PIV technique to investigate the internal flow field in a centrifugal pump. Stress was laid on the flow distribution at a nominal flow rate, and an unsteady velocity field together with principal Reynolds normal stress and the principal Reynolds shear stress were revealed. Feng et al. [12] successfully used LDV to periodically measure unsteady flow in a radial flow pump, and complex flow structures in the interaction region

*Corr. Author's Address: Jiangsu University, Xuefu road 301, Zhenjiang, China, zhangningwlg@163.com

between the rotating impeller and stationary diffuser were captured. To alleviate the intense rotor-stator interaction, some effective approaches could be implemented, for instance increasing the radial gap between the impeller and volute [13], optimal design of the impeller and the volute and some specially devised structures of the pump [14]. However, in these studies, most simply concentrate on pressure amplitude at f_{BPF} or unsteady flow structure individually, and a combination analysis has rarely been conducted. As a result, a comprehensive understanding of rotor-stator interaction, especially the correlation between instantaneous flow dynamics and pressure pulsation, has not been thoroughly illustrated.

In this study, unsteady rotor-stator interaction in a low specific speed centrifugal pump is analysed using a numerical method. Pressure pulsation signals together with vorticity distribution are attained. Special attention is laid on the vortical structure shedding in the wake of the blade trailing edge and the interaction with the volute tongue. The detailed evolution process of vortical structures at the near tongue region and within the blade channel are focused and analysed. Finally, the correlation between pressure amplitude and vorticity distribution is discussed.

1 NUMERICAL INVESTIGATION

1.1 Governing Equations

After adding a filter to Navier-Stokes (N-S) and continuity equations, LES governing equations can be described in the following form:

$$\frac{\partial \overline{u}_i}{\partial x_i} = 0, \tag{1}$$

$$\frac{\partial \overline{u}_i}{\partial t} + \frac{\partial}{\partial x_j}(\overline{u}_i \overline{u}_j) = \\ = -\frac{1}{\rho}\frac{\partial \overline{p}}{\partial x_i} + \frac{\partial}{\partial x_j}\left[\nu\left(\frac{\partial \overline{u}_i}{\partial x_j} + \frac{\partial \overline{u}_j}{\partial x_i}\right)\right] + \frac{\partial \overline{\tau}_{ij}}{\partial x_j} + S_i, \tag{2}$$

where $\overline{u}_i$ $(i = 1, 2, 3)$ is the grid-scale velocity component, $\overline{p}$ is the grid-scale static pressure, ρ is the density and ν is the kinematic viscosity. S_i is the source term, and $\overline{\tau}_{ij}$ is the subgrid-scale (SGS) stress tensor having the form of $\overline{\tau}_{ij} = \overline{u_i u_j} - \overline{u_i}\,\overline{u_j}$. From comparisons with conventional Navier-Stokes (N-S) equations, it is found that an additional SGS stress tensor $\overline{\tau}_{ij}$ term is introduced in the LES governing equations. In the present study, SGS model Smagorinsky-Lilly is applied to close the equations and $\overline{\tau}_{ij}$ term is solved in Eq. (3).

$$\overline{\tau}_{ij} - \frac{1}{3}\delta_{ij}\overline{\tau}_{kk} = -2\nu_T \overline{S}_{ij}, \tag{3}$$

where $\overline{S}_{ij}$ is the strain rate tensor and ν_T is the SGS stress viscosity having the form of Eq. (4).

$$\nu_T = (C_s \Delta)^2 \left|\overline{S}\right|, \tag{4}$$

$$\left|\overline{S}\right| \equiv \sqrt{2\overline{S}_{ij}\overline{S}_{ij}}, \tag{5}$$

where Δ is the filter scale and C_s is a dimensionless parameter called the Smagorinsky coefficient. Moreover, during numerical calculation, C_s is usually a constant 0.1.

1.2 Mesh Generation

A low specific speed n_s = 69 centrifugal pump, incorporating a two-dimensional impeller with six backward-curved blades, is designed for investigation. Moreover, the main parameters of the model pump are presented in Table 1. During numerical simulation, the front and back chambers of the model pump are usually neglected for simplification. However, in low specific speed pumps, the leakage flow from the wear ring clearance is normally more than 5 % of the total flow rate, and it would have a significant effect on the unsteady flow structure inside the model pump. Therefore, in this paper, the entire computational domain, containing inlet suction, impeller, volute, pump outlet, front and back chambers, is established for calculation as shown in Fig. 1. Moreover, the wear ring clearance is 0.5 mm.

Table 1. *Main design parameters of the model pump*

Parameters	value
Nominal flow rate Q_d	55 m³/h
Designed head H_d	20 m
Nominal rotating speed n_d	1450 r/min
Specific speed $n_s = 3.65 n_d \sqrt{Q_d} / H_d^{0.75}$	69
Blade number Z	6
Angle of volute tongue	20°
Impeller suction diameter D_1	80 mm
Impeller outlet diameter D_2	260 mm
Impeller outlet width b_2	17 mm
Volute inlet diameter D_3	290 mm
Volute outlet diameter D_4	80 mm
Tangential velocity at impeller exit u_2	19.6 m/s
Impeller rotating period ΔT	0.0414 s

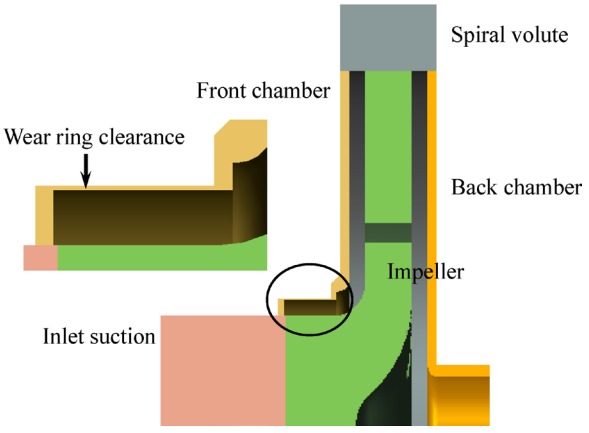

Fig. 1. *Computational domain of the model pump*

Structured grids of the model pump are generated using the Ansys-ICEM mesh generation tool for high precision calculation. Fig. 2 shows partially structured grids at the mid-span of the impeller. In the near-wall region, a fine grid is required by LES, so grid cells near the wall are refined to satisfy the requirement [15] to [17]. At the near wall region, the mesh cell size is lower than 0.5mm. Finally, the averaged y^+ value of the whole computational domain is approximately 4.5, which would provide adequate resolution in the critical regions of the computation domain. After the independent mesh check, the performance of the model pump does not change more than 0.5 % when the overall mesh element exceeds 2×10^6. Finally, the overall mesh element used in the calculation is about 2.5×10^6. The mesh element of each part, i.e. inlet and outlet suctions, impeller, volute casing, front chamber, back chamber, is 58,240; 56,128; 1,298,386; 752,361; 270,668; 127,372, respectively. The same mesh is used for steady and transient simulation.

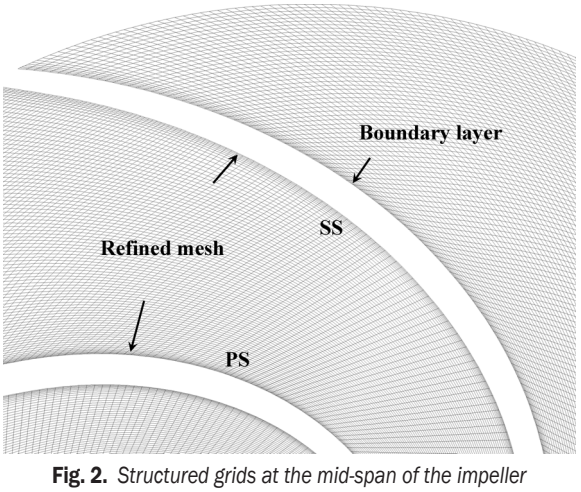

Fig. 2. *Structured grids at the mid-span of the impeller*

1.3 Solution Parameters

Commercial software Ansys-Fluent 13.0 is used for numerical simulation. For transient LES calculation, steady numerical simulation results achieved by the RNG k–ε model are set as the initialization condition. Velocity inlet boundary condition is imposed at the pump inlet suction, where a spectral synthesizer is chosen for fluctuating velocity algorithm.

A constant pressure $p=1\times10^5$ Pa boundary condition is imposed at the pump outlet. To achieve adequate resolution of pressure signals, the time step is set as $\Delta t=1.15\times10^{-4}$ s. During numerical simulation, when the continuity residual is lower than 3×10^{-5}, the result is considered to be converged. Nearly 30 impeller revolutions are calculated to enable periodic pressure pulsation results. Moreover, the inside faces of the front and back chambers rotate synchronously with the rotating impeller.

It is well accepted that even at a nominal flow rate, flow field distribution along the volute periphery tongue casing is not circumferentially uniform leading to pressure pulsating [18] and [19]. Therefore, it is essential to have a comprehensive understanding of pressure pulsation along the volute. For this purpose, twenty monitoring points are evenly mounted on the volute casing near the impeller exit, as seen in Fig. 3. The angle between two adjacent monitoring points is 18 deg. The angle of the volute tongue is 20 deg, and it is located between Point B and Point C. Pressure pulsation signals are processed with a FFT (Fast Fourier Transform) algorithm to investigate pressure spectrum characteristics under various flow rates.

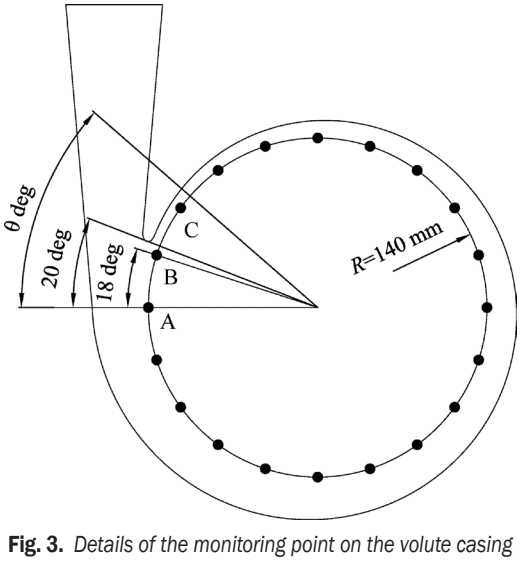

Fig. 3. *Details of the monitoring point on the volute casing*

2 EXPERIMENTAL SETUP

To validate the accuracy of the current numerical method, experimental investigation of the model pump was conducted on a closed test rig as shown in Fig. 4. An electronic flowmeter was applied to obtain flow rates of the model pump at various operating conditions; meanwhile, the head was measured using the pressure gauges located at the pump inlet and outlet pipes. The measuring errors are lower than 1% of the measured values. During experiments, the rotating speed of the model pump was ensured to be at the design value of 1450 r/min by adopting a frequency inverter. Meanwhile, one pressure transducer (PCB113B27 series) is mounted at Point C to achieve the pressure spectrum. During experiments, the inlet static pressure is about atmospheric pressure. Even at 1.4 Q_d, the critical NPSH is about 3.3 m, which means that cavitation could not occur during pump operations.

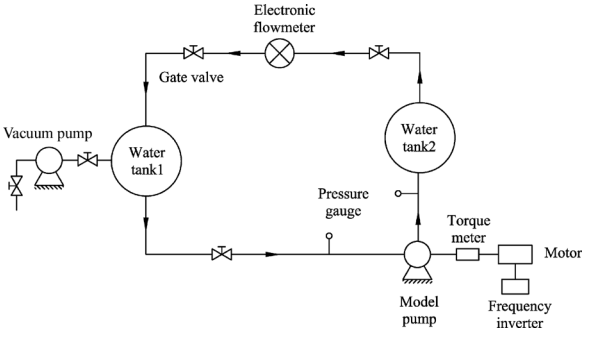

Fig. 4. *Closed test platform*

3 RESULTS AND DISCUSSIONS

3.1 Validation of the Numerical Method

To validate the accuracy of the current numerical method, Fig. 5a shows a performance comparison between numerical and experimental results. The best efficiency point is around 1.1 Q_d. The predicted results exhibit good agreement with the experimental results. From 0.4 Q_d to1.4 Q_d, calculation errors are lower than 2%. At flow rates lower than 0.4 Q_d, numerical error increases, rising to 3.5 % from head curve at 0.2 Q_d. It remains a satisfactorily precise calculation. As observed from Fig. 5b, the calculation error at f_{BPF} is relatively small: normally lower than 10 %. As for pulsation pressure prediction, it is a fairly good result [20] and [21]. Numerical result shows that leakage flow from the wear ring clearance is almost 10% of the total flow rate at the design flow rate, and it increases to 19 % of the total flow rate at 0.2 Q_d. Therefore, it is unreasonable to exclude the front chamber in low specific speed centrifugal pumps, since the disturbance flow at the impeller inlet leaking from the wear ring clearance would generate apparent influence on the unsteady flow field.

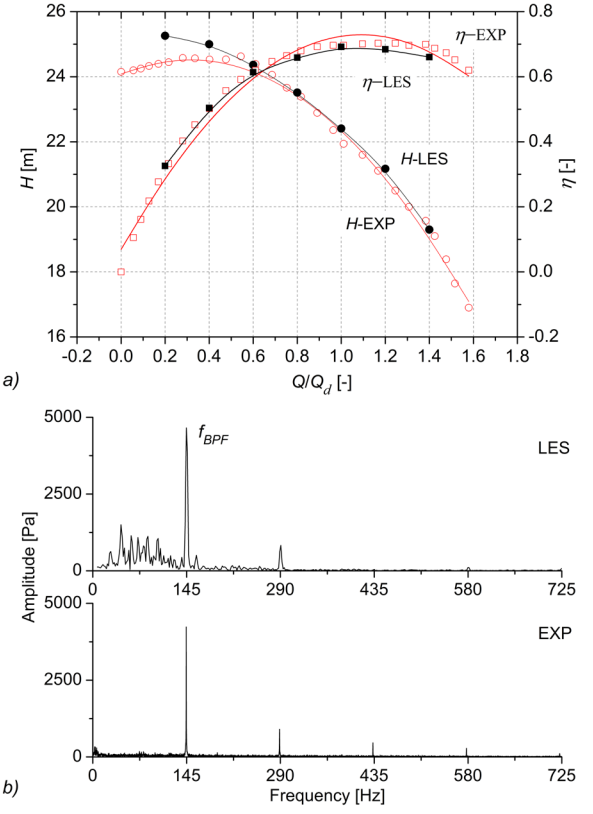

Fig. 5. *a) Performance comparison between experimental and numerical results, b) comparison of pressure spectra*

From the comparison results, it indicates that the current numerical method could effectively capture the main flow structures within the model pump.

3.2 Unsteady Pressure Pulsations

Fig. 6a shows the time domain pressure signals of Point C for numerical simulation, and the corresponding pressure spectra are shown in Fig. 6b. It is found that pressure signals fluctuate significantly, and pronounced peaks at blade passing frequency f_{BPF} (145 Hz) dominate the pressure spectra under different flow rates. Meanwhile, the high harmonic frequency $2f_{BPF}$ could also be identified.

According to Fig. 6b, discrete peaks at f_{BPF} are the predominant components in pressure spectra inferred

from the numerical results. Due to the asymmetry of the spiral volute and jet-wake flow pattern at the blade exit, flow field is not circumferentially uniform, and it would affect pressure spectra at different monitoring points along the volute casing. To clarify the correlation, Fig. 7 presents angular distributions of pressure amplitudes at f_{BPF} under various flow rates. It is observed that angular distribution of pressure amplitude at f_{BPF} exhibits a modulated pattern characterized by the presence of six local peaks and valleys. The modulation pattern is closely associated with rotor-stator interaction inside the model pump [22] and [23]. At off-design conditions, especially at flow rates of 0.2 Q_d and 1.4 Q_d, pressure amplitudes are much larger than that at the rated condition.

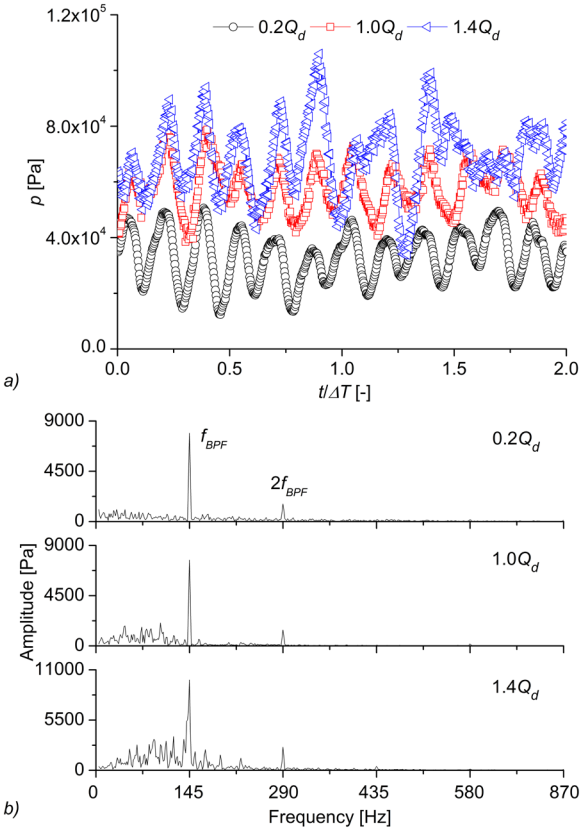

Fig. 6. *a) Time domain pressure pulsation signals at point C under three flow rates, b) the corresponding pressure spectra*

From Fig. 7, it is also noted that pressure amplitudes at the near tongue region, Points A, B, and C, show great discrepancy, and Fig. 8 presents the enlarged configuration of pressure amplitudes at f_{BPF} for a nominal flow rate. As observed, pressure amplitude at Point B (θ = 18 deg ahead of the volute tongue) is quite small. In contrast, pressure amplitude at the point after the volute tongue, around Point C (θ

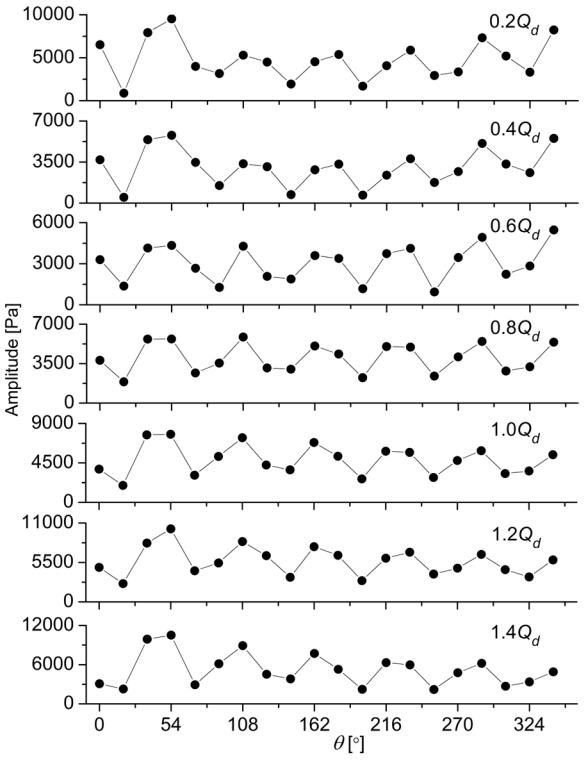

Fig. 7. *Angle distributions of pressure amplitudes at fBPF along the volute casing under various flow rates*

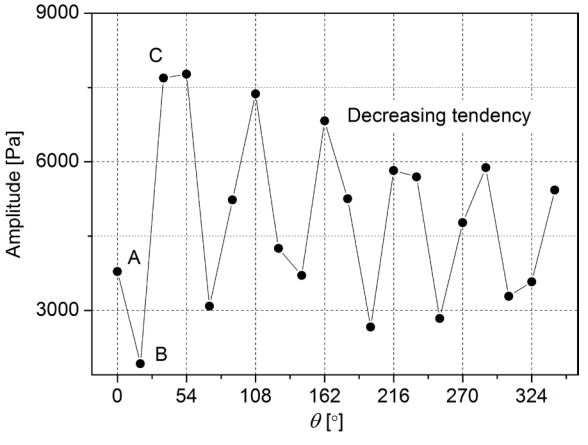

Fig. 8. *Pressure amplitudes at fBPF for nominal flow rate*

= 54 deg), achieves maximum, indicating that rotor-stator interaction is more intense around this region. This phenomenon is more obvious when the model pump operates at low flow rates of 0.2 Q_d and 0.4 Q_d. At a great distance from the volute tongue (θ > 54 deg), rotor-stator interaction is less intense due to the increasing radial gap between the impeller and volute. As shown in Fig. 8, it is evident that pressure amplitudes (θ > 54 deg) show a decreasing tendency

due to the less significant rotor-stator interaction. In these regions, pressure pulsation is mainly induced by the unsteady flow structure shedding from the blade trailing edge (jet-wake pattern).

3.3 Instantaneous Flow Dynamics

Based on the results of Fig. 7 and Fig. 8, it is clear that pressure amplitudes on the periphery of the spiral volute casing show a significant difference. Around the volute tongue region, pressure amplitude at Point C is much larger than that at Point B, as means that flow induced pulsation pressure mechanisms at these regions are obviously different. Therefore, it is essential to clarify flow structures inside the model pump and its influence on pressure amplitude, particularly around the volute tongue zone, where intense fluid-structure interaction is expected.

Fig. 9 shows relative velocity distributions on the mid-span of the impeller for four flow rates, namely 0.2 Q_d, 0.6 Q_d, 1.0 Q_d and 1.4 Q_d. As observed, at a high flow rate of 1.4 Q_d, flow mainly concentrates on the blade suction side due to the increasing blade inlet angle, and the high-velocity region almost covers the whole blade passage, extending to the blade exit. At almost half chord of the blade pressure side, a significant low relative velocity region is formed. Meanwhile, a small portion of the flow detaches from the blade surface in this region. At a low flow rate of 0.6 Q_d, the separate flow region on the blade pressure side expands, forming a significant counter-clockwise rotating vortex. At the blade exit, the velocity of the flow near the blade pressure side is much larger than that near the blade suction side. Hence, flow at the impeller outlet is characterized by a jet-wake pattern, which results in pressure pulsating at any position along the spiral volute casing. At 0.2 Q_d, due to the reverse flow at the blade exit, a large scale vortex occurs on the blade pressure side in Channel 2 causing partial blade channel blockage. In general, at low flow rate, flow separation may easily occur inside the blade channels due to the inlet flow deviating seriously from the rated condition. As observed in Channel 1, flow distribution is in a disorderly status characterized by many small scale vortices developed. At a nominal flow rate, flow distribution is more uniform than that at off-design conditions, especially at the blade outlet region. However, the separate flow region on the blade pressure side could still be observed. Due to the high incident angle, flow tends to move towards the blade suction side, and low-velocity magnitude on the blade pressure side is expected. Furthermore, the curvature of the blade may be larger, and fluid could not move along the blade streamlines. Consequently, a high-pressure gradient occurs, leading to secondary flow forming. Finally, a separate flow structure develops on the blade pressure side due to the combination effects.

$$\text{Vorticity} = 2\omega_z = \left(\frac{\partial v_y}{\partial x} - \frac{\partial v_x}{\partial y} \right). \quad (6)$$

Having investigated relative velocity inside the blade channels at four flow rates, vorticity distribution would be further analysed to illustrate instantaneous flow dynamics. Fig. 10 shows the vorticity magnitude at the mid-span of the impeller for a nominal flow rate. As observed, four typical vorticity regions with high magnitude developed inside the model pump, specifically regions α, β, γ, and δ. At the blade pressure side of each channel, high vorticity magnitude region β is observed, in accordance with the flow detachment region as shown in Fig. 9. The vorticity value in the central zone of the impeller is quite small indicating that the flow field is relatively uniform. On the blade suction side, another strong vorticity region γ is generated, and it almost starts from the blade leading edge covering the whole blade chord. This high vorticity region is probably caused by the boundary layer developed on the blade suction side, and a high-velocity gradient is usually expected in this region. The vorticity sheet shows good coherence on the blade before approaching the blade trailing edge. At the blade outlet, it is evident that the vortical structure in region γ starts to detach from the blade suction side, consequently shedding in the wake. Then the shed vortical structure moves into the volute casing; therefore, a high vorticity magnitude region δ is generated inside the volute casing. The periodic shedding effect of the vortical structure would cause intense pressure changes and pulsations, as characterized by the modulated pattern shown in Fig. 7. At the near tongue area, it is noted that a rather strong vorticity region α is generated. It is caused by the impingement effect between the shedding vortex from the blade trailing edge and the volute tongue. Due to the impingement effect, turbulence activity in this region is more intense, as manifested by the increase of vorticity magnitude, and it would have a significant influence on pressure pulsations in this region.

Due to the intense impeller-tongue interaction, the flow structure around the near tongue region is rather complicated and distorted. As observed in Fig. 7, pressure amplitudes at the near tongue region, Points A, B, and C, show significant discrepancy. The pressure magnitude at Point C is almost 4 times that at Point B. Besides, in Fig. 10, vorticity magnitudes

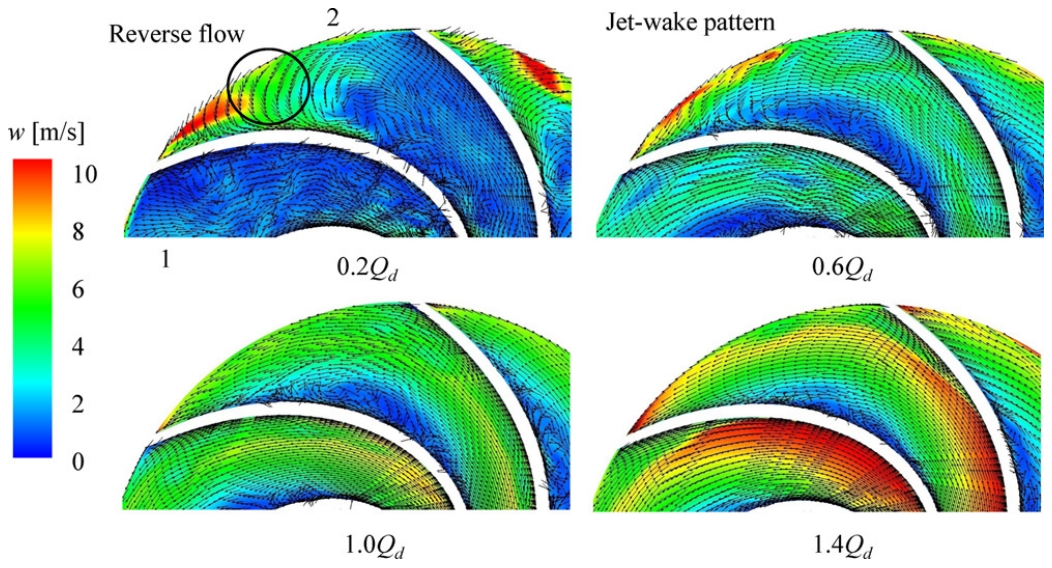

Fig. 9. Relative velocity distributions on mid-span of the impeller for different flow rates

in the areas before and after the volute tongue differ obviously, and a high vorticity magnitude area is generated at the after tongue region. Therefore, the emphasis is placed upon the vorticity distribution at the interested near tongue region to investigate instantaneous flow dynamics and clarify the correlation between vortical structure and pressure amplitude.

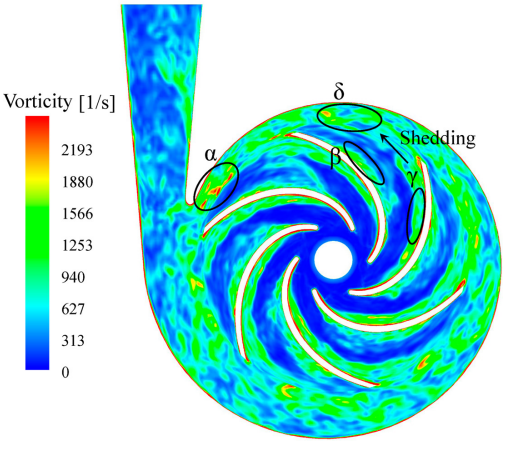

Fig. 10. *Vorticity distribution at the mid-span of the impeller under nominal flow rate*

Fig. 11 shows instantaneous vorticity distributions for four consecutive positions of the impeller at the rated condition. At $t_1 = 0$ (Fig. 11a), it is evident that two vortical structures, denoted as VS1 and VS2, are generated around the volute tongue. These vortical structures are closely associated with the wake shedding from the trailing edge of Blade 3. When approaching the volute tongue, the vortical structure impinges on the tongue, and it is cut into two parts (VS1 and VS2). Then the two resultant vorticity zones continue their motion towards the pump exit and the narrow side of the tongue respectively. In Fig. 11b, when Blade 2 aligns with the tongue, the torn-off portion, VS1 moves to the pump outlet and experiences a reduction in magnitude. It is more significant that seen in Fig. 11d, and VS1 becomes progressively weaker, while undergoing some distortion. This is due to the combination effect of the bending and streamwise stretching of the vortical structure near the volute tongue and its mixing effect with the external flow with lower vorticity magnitude in the diffuser section. Finally, with the impeller rotating, VS1 would dissipate in the diffuser section. It is also noted that the magnitude of VS2 undergoes a rapid decrease at this moment. This is due to the increasing of the radial distance between the impeller and the volute when VS2 continues its motion to the narrow side of the volute tongue. In Fig. 11c, with the impeller continuously rotating, Blade 2 moves away from the volute tongue. However, the wake shedding from the trailing edge of Blade 2 has not reached to the tongue; therefore, the intense impingement effect does not occur. Consequently, the low vorticity magnitude around Point B is always observed.

According to the results of Fig. 11, vortical structures around the volute tongue that show obvious differences, which cause different pressure amplitudes at Points B, and C. Due to the impingement effect of vortical structure on the tongue, a high magnitude of

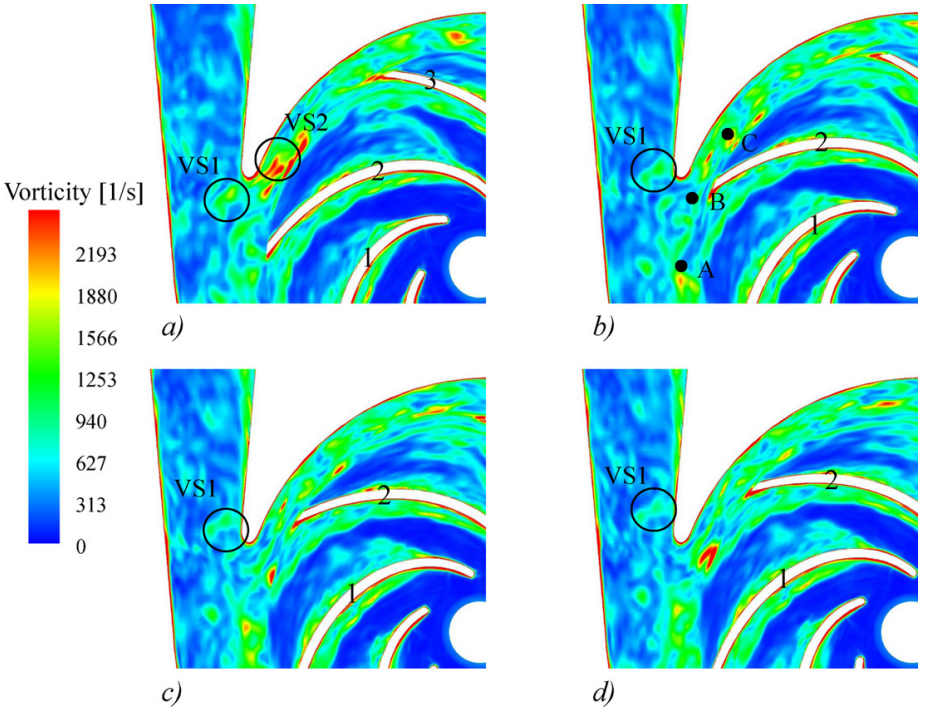

Fig. 11. *Configurations of vorticity distributions around the volute tongue at the mid-span of the impeller for four consecutive positions at nominal flow rate; a) t_1 = 0, b) t_2 = 18/360 ΔT, c) t_3 = 28/360 ΔT, d) t_4 = 38/360ΔT*

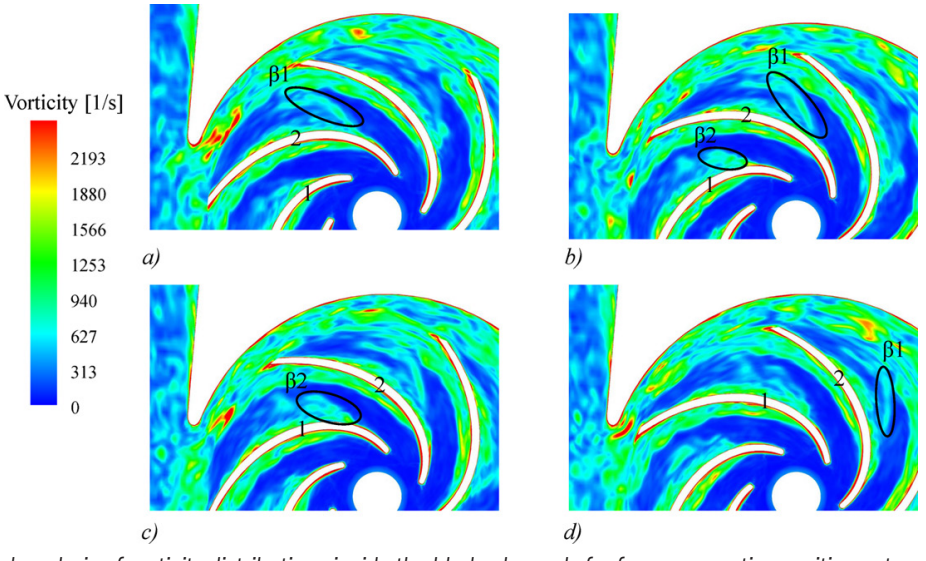

Fig. 12. *Detailed analysis of vorticity distributions inside the blade channels for four consecutive positions at nominal flow rate; a) t_1=0, b) t_2=28/360 ΔT, c) t_3=48/360 ΔT, d) t_4=78/360 ΔT*

the vorticity region VS2 is generated. It also means that strong turbulence activity is expected in this region as indicated by the high value of vorticity magnitude, and the corresponding Point C coincidentally is located in this area. As a contrast, Point B would always undergo lower vorticity magnitude with the impeller rotating periodically. Therefore, it is certain that the pressure amplitudes of the monitoring point are closely associated with the corresponding vorticity magnitudes, and high vorticity magnitude would generally result in high-pressure amplitude.

The unsteady rotor-stator interaction has two kinds of effects, as discussed by Feng et al. [12]. The first is the downstream effect of the impeller acting on

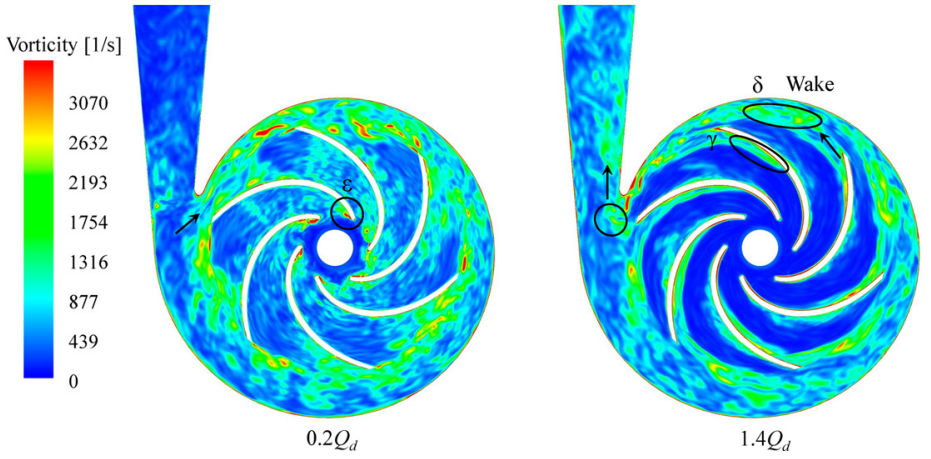

Fig. 13. *Vorticity magnitudes at off-design flow rates of 0.2 Q_d and 1.4 Q_d*

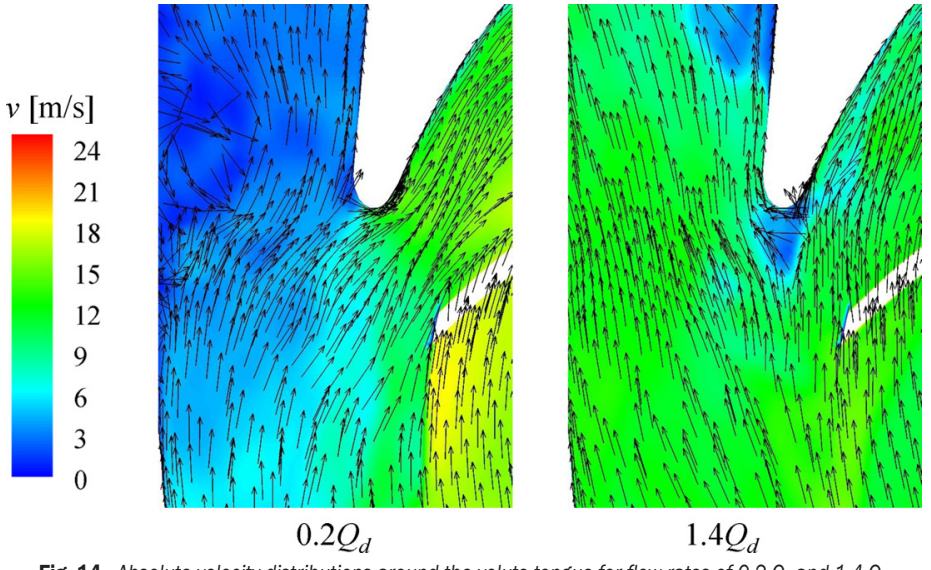

Fig. 14. *Absolute velocity distributions around the volute tongue for flow rates of 0.2 Q_d and 1.4 Q_d*

the stator characterized by the unsteady effects due to flow discharged from the impeller and the jet-wake flow pattern. The second is the upstream effect of the stator acting on the flow distribution inside the impeller channels. Moreover, in this study, the upstream effect of the volute tongue is significant from vorticity distribution inside the different blade channels. From Fig. 12, it is found that vorticity distribution in blade Channel 2 facing the volute tongue is different from that at other channels as shown in Fig. 10. In Fig. 10, vorticity region β shows good coherent on the blade pressure side, however, in Fig. 12a, vorticity region $\beta 1$ detaches from Blade 2, extending into the central zone of the blade channel. In Fig. 12b, with Blade 2 moving away from the volute tongue, vorticity region $\beta 1$ separates completely from Blade 2. Moreover, it experiences a reduction in magnitude due to the mixing effect of the low vorticity magnitude fluid in the central zone of the blade channel, as shown in Fig. 12d; finally, it would be shed in the wake of the blade trailing edge into the volute casing. With Blade 1 moving close to the volute tongue, the upstream effect of the volute tongue would significantly affect the vorticity distribution inside Blade channel 1. As shown in Fig. 12b, vorticity region $\beta 2$ starts to detach from the pressure side of Blade 1. With Blade 1 rotating further, vorticity region $\beta 2$ separates and stretches into the central zone of the channel. Finally, it would also undergo a decrease in magnitude and be shed in wake into the volute casing. Therefore, it is concluded that the vorticity distributions in different blade channels show great discrepancy due to the upstream effect of

the volute tongue acting on the impeller. When the blade channel passes the volute tongue, the vorticity region on the blade pressure side would detach into the central zone of the channel. However, in other blade channels, the vortical structure shows coherent characteristics on the blade pressure sides.

As observed in Fig. 9, it is evident that flow structures at off-design conditions show great discrepancy compared with that at the nominal condition. Fig. 13 presents vorticity distributions at flow rates of 0.2 Q_d and 1.4 Q_d. At the high flow rate of 1.4 Q_d, the blade inlet angle is much larger than that at the nominal flow rate leading to flow deviating to the blade suction side. Due to the impacting effect of the inflow on the blade suction side, vorticity region γ differs significantly from that at a nominal flow rate. At 1.0 Q_d, vorticity region γ develops from the blade leading edge almost covering the whole blade channel. However, at 1.4 Q_d, vorticity region γ starts to develop at the blade downstream covering half of the blade chord. At the blade trailing edge, vortical structure sheds in the wake, which is in coincidence with that at a nominal flow rate. At a low flow rate of 0.2 Q_d, in contrast with that at 1.4 Q_d, the blade inlet angle is much smaller than that at a nominal flow rate. Flow at the blade leading edge would deviate to the blade pressure side. As observed, high vorticity region ε develops at the blade leading edge due to the deviating effect of the inflow. Vorticity sheets, at blade pressure and suction sides, are not significant compared with that at the rated condition. As presented in Fig. 9, many small-scale vortices are generated in the central zone of the blade channel, resulting in vorticity magnitude increasing rapidly.

Furthermore, it is found that vortical structures show a significant difference for flow rates 0.2 Q_d and 1.4 Q_d at the near tongue region. At 1.4 Q_d, vortical structure shedding from the blade outlet is eventually cut by the volute tongue and interacts with the tongue intensely. One portion of the vortical structure continues to move to the diffuser exit. However, at a low flow rate of 0.2 Q_d, the cut effect of the volute tongue is not significant, and the whole wake approaching the volute tongue moves to the narrow side of the tongue. The vortical structure at the near tongue region is closely associated with the corresponding absolute velocity distribution as presented in Fig. 14. At a low flow rate of 0.2 Q_d, a significant portion of the fluid leaks from the wide side of the tongue to the narrow side of the volute tongue. In contrast, at a high flow rate of 1.4 Q_d, all fluid tends to move into the diffuser section of the volute casing. Thus, the vortical structure at the near tongue zone is associated with absolute velocity distribution and is significantly affected by the leakage flow direction at the volute tongue region.

4 CONCLUSIONS

Rotor-stator interaction and unsteady flow in a low specific speed centrifugal pump are investigated in this study, and some conclusions are carried out.

Angular distributions of pressure amplitudes at f_{BPF} show a typical modulated pattern due to the intense rotor-stator interaction. At nominal flow rate, pressure amplitudes at f_{BPF} along the volute casing show a decreasing tendency in the distant region of the volute tongue, and it is attributed to the increasing gap between the impeller and volute.

Four different patterns of vorticity regions are captured on the mid-span of the impeller. It is evident that the vortical structure, shedding in the wake from the blade exit, interacts intensely with the volute tongue. From a combination analysis of pressure pulsation and vortical structure, it is found that the pressure pulsation amplitude is determined by the corresponding vorticity magnitude. When the blade passes the volute tongue, it is also evident that the upstream effect of the volute tongue has a significant influence on vorticity distribution on the blade pressure side. At off-design flow rates, vortical structures on the blade suction side at 1.4 Q_d, blade leading edge and around the tongue region at 0.2 Q_d exhibit great discrepancy from that at a nominal flow rate.

For further investigation, experimental investigations consisting of pressure pulsation and unsteady PIV measurements should be conducted to validate the numerical results and provide a comprehensive view of rotor-stator interaction in centrifugal pumps.

5 ACKNOWLEDGMENT

The authors gratefully acknowledge the financial support of National Natural Science Foundation of China (51576090, 51476070, 51206063), a Project Funded by the Priority Academic Program Development of Jiangsu Higher Education Institutions (PAPD), and the Research and Innovation Project for College Graduates of Jiangsu Province (KYLX_1036).

6 REFERENCES

[1] Rodriguez, C.G., Mateos-Prieto, B., Egusquiza, E. (2014). Monitoring of rotor-stator interaction in a pump-turbine

using vibration measured with onboard sensors rotating with shaft. *Shock and Vibration*, vol. 2014, art. ID. 276796, **DOI:10.1155/2014/276796**.

[2] Kato, C., Mukai, H., Manabe, A. (2003). Large-eddy simulation of unsteady flow in a mixed-flow pump. *International Journal of Rotating Machinery*, vol. 9, no. 5, p. 345-351, **DOI:10.1155/S1023621X03000320**.

[3] Liu, H.L., Wang, K., Kim, H.B., Tan, M.G., (2013). Experimental investigation of the unsteady flow in a double-blade centrifugal pump impeller. *Science China Technological Sciences*, vol. 56, no. 4, p.812-817, **DOI:10.1007/s11431-013-5154-0**.

[4] Byskov, R.K., Pedersen, N. (2003). Flow in a centrifugal pump impeller at design and off-design conditions-part II: large eddy simulations. *ASME Journal of Fluids Engineering*, vol. 125, no. 1, p. 73-83, **DOI:10.1115/1.1524586**.

[5] Pei, J., Yuan, S.Q., Yuan, J.P. (2013). Fluid-structure coupling effects on periodically transient flow of a single-blade sewage centrifugal pump. *Journal of Mechanical Science and Technology*, vol. 27, no. 7, p.2015-2023, **DOI:10.1007/s12206-013-0512-1**.

[6] Posa, A., Lippolis, A., Verzicco, R., Balaras, E. (2011). Large-eddy simulations in mixed-flow pumps using an immersed-boundary method. *Computers & Fluids*, vol. 47, no. 1,p. 33-43, **DOI:10.1016/j.compfluid.2011.02.004**.

[7] Posa, A., Lippolis, A., Balaras, E. (2015). Large-eddy simulation of a mixed-flow pump at off-design conditions. *ASME Journal of Fluids Engineering*, vol. 137, no. 10, p. 101302, **DOI:10.1115/1.4030489**.

[8] Parrondo, J.L., González, J., Fernández-Francos, J. (2002). The effect of the operating point on the pressure fluctuations at the blade passage frequency in the volute of a centrifugal pump. *ASME Journal of Fluids Engineering*, vol. 124, no. 3, p. 784-790, **DOI:10.1115/1.1493814**.

[9] Keller, J., Blanco, E., Barrio, R., Parrondo, J. (2014). PIV measurements of the unsteady flow structures in a volute centrifugal pump at a high flow rate. *Experiments in Fluids*, vol. 55, no. 10, art no.1820, **DOI:10.1007/s00348-014-1820-7**.

[10] Wu, Y.L., Yuan, H.J., Shao, J., Liu, S.H. (2009). Experimental study on internal flow of a mini centrifugal pump by PIV measurement. *International Journal of Fluid Machinery and Systems*, vol. 2, no. 2, p. 121-126, **DOI:10.5293/IJFMS.2009.2.2.121**.

[11] Wu, Y.L., Liu, S.H., Yuan, H.J., Shao, J. (2011). PIV measurement on internal instantaneous flows of a centrifugal pump. *Science China Technological Sciences*, vol. 54, no. 2, p. 270-276, **DOI:10.1007/s11431-010-4262-3**.

[12] Feng, J.J., Benra, F.K., Dohmen, H.J. (2011). Investigation of periodically unsteady flow in a radial pump by CFD simulations and LDV measurements. *ASME Journal of Turbomachinery*, vol. 133, no. 1, art. id. 011004, **DOI:10.1115/1.4000486**.

[13] Yang, S.S., Liu, H.L., Kong, F.Y., Xia, B., Tan, L.W. (2014). Effects of the radial gap between impeller tips and volute tongue influencing the performance and pressure pulsations of pump as turbine. *ASME Journal of Fluids Engineering*, vol. 136, no. 5, art. no. 054501, **DOI:10.1115/1.4026544**.

[14] Zhang, N., Yang, M.G., Gao, B., Li, Z., Ni, D. (2015). Experimental investigation on unsteady pressure pulsation in a centrifugal pump with special slope volute. *ASME Journal of Fluids Engineering*, vol. 137, no. 6, art. no. 061103, **DOI:10.1115/1.4029574**.

[15] Yang, Z.J., Wang, F.J., Zhou, P.J. (2012). Evaluation of subgrid-scale models in large-eddy simulations of turbulent flow in a centrifugal pump impeller. *Chinese Journal of Mechanical Engineering*, vol. 25, no. 5, p. 911-918, **DOI:10.3901/CJME.2012.05.911**.

[16] Yamanishi, N., Fukao, S., Qiao, X., Kato, C., Tsujimoto,Y. (2007). LES simulation of backflow vortex structure at the inlet of an inducer. *ASME Journal of Fluids Engineering*, vol. 129, no .5, p. 587-594, **DOI:10.1115/1.2717613**.

[17] Bing, H., Cao, S.L. (2014). Parametrization of blade leading and trailing edge positions and its influence on mixed-flow pump performance. *Journal of Mechanical Engineering Science*, vol. 228, no. 4, p.703-714, **DOI:10.1177/0954406213490104**.

[18] Gao, Z.X., Zhu, W.R., Lu, L., Deng, J., Zhang, J.G., Wuang, F.J. (2014). Numerical and experimental study of unsteady flow in a large centrifugal pump with stay vanes. *ASME Journal of Fluids Engineering*, vol. 136, no. 7, art. no. 071101, DOI:10.1115/1.4026477.

[19] Pei, J., Benra, F.K., Dohmen, H.J. (2012). Application of different strategies of partitioned fluid-structure interaction simulation for a single-blade pump impeller. *Proceedings of the Institution of Mechanical Engineers. Part E: Journal of Process Mechanical Engineering*, vol. 226, no. 4, p. 297-308, **DOI:10.1177/0954408911432974**.

[20] Barrio, R., Fernández, J., Blanco, E., Parrondo, J. (2011). Estimation of radial load in centrifugal pumps using computational fluid dynamics. *European Journal of Mechanics - B/Fluids*, vol. 30, no. 3, p. 316-324, **DOI:10.1016/j.euromechflu.2011.01.002**.

[21] Barrio, R., Blanco, E., Parrondo, J., González, J., Fernández, J. (2008). The effect of impeller cutback on the fluid-dynamic pulsations and load at the blade-passing frequency in a centrifugal pump. *ASME Journal of Fluids Engineering*, vol. 130, no. 11, art. no. 111102, **DOI:10.1115/1.2969273**.

[22] Barrio, R., Parrondo, J., Blanco, E. (2010). Numerical analysis of the unsteady flow in the near-tongue region in a volute-type centrifugal pump for different operating points. *Computers & Fluids*, vol. 39, no. 5, p. 859-870, **DOI:10.1016/j.compfluid.2010.01.001**.

[23] Fu, Y., Yuan, J., Yuan, S., Pace, G., d'Agostino, L., Huang, P., Li, X. (2015). Numerical and experimental analysis of flow phenomena in a centrifugal pump operating under low flow rates. *ASME Journal of Fluids Engineering*, vol. 137, no. 1, art. no. 011102, **DOI:10.1115/1.4027142**.

Strojniški vestnik - Journal of Mechanical Engineering 62(2016)1, 32-40
DOI:10.5545/sv-jme.2015.2611
Short Scientific Paper
Received for review: 2015-04-17
Received revised form: 2015-10-12
Accepted for publication: 2015-11-09

Using Sandwich Composite Shells for Fully Pressurized Tanks on Liquefied Petroleum Gas Carriers

Veysel Alankaya[1,*] – Fuat Alarçin[2]
[1]Turkish Naval Academy, Department of Naval Architecture, Turkey
[2]Yıldız Technical University, Department of Marine Engineering Operation, Turkey

The growth of shipping as the main link of the seaborne gas supply chain results from the growing demand for liquefied petroleum gasses due to their various uses, such as fuel for cooking/heating, automotive power, and numerous applications. This study investigates the structural suitability of sandwich composite materials for pressurized tanks, which can be used in on-board carriers or barges for transportation, as well as inland for industrial or residential storage needs. The analytical solution methodology for analysing stresses and deformations is based on higher order shear deformation theory (HSDT). A boundary discontinuous generalized double Fourier series approach is used to solve highly coupled linear partial differential equations. The complementary boundary constraints are introduced through boundary discontinuities, generated by the selected boundary conditions for the derivation of the complementary solution. Numerical solutions are presented for laminated sandwich shells having both cylindrical and spherical forms, which are the preferred geometries for pressurized tanks.
Keywords: sandwich composites, pressurized tanks, boundary-discontinuity, doubly curved shell, liquefied petroleum gas carriers

Highlights
- *HSDT with arbitrary boundary conditions was studied.*
- *Laminated sandwich composite shells are analysed with the presented mathematical model.*
- *Results are in good agreement with FEA counterparts.*
- *Effect of core layer and geometry using stress distribution is presented.*

0 INTRODUCTION

Petroleum gases, an alternative to fuel oil with lower prices, are preferred for numerous uses, which can be briefly listed as (i) in-house basic needs, such as cooking and heating, (ii) industrial needs for power plants, plastic and chemical applications, and (iii) propulsion fuel for transportation. This large operational suitability causes the configuration of a distribution network depending on pipelines for the areas with infrastructure, storages for field usage, or shipping solutions for seaborne supply.

The U.S. Energy Administration estimates energy consumption, which was approximately 825 million barrels in 2013, to increase by 0.6 % annually from 2012 to 2040 while the natural oil resources are declining [1].

Since many world oil resources are difficult to reach, growth in sea gas transport capacity and the construction of new gas transport pipelines are expected.

As indicated by Fujitani et al. [2], while pipelines on land and in the sea can deliver the gas in gaseous form only over relatively short distances, another means of transporting the gas in larger quantities over longer distances is required.

The most cost efficient way of transporting gas between continents is to carry it in liquid form using ships. Further transport cost reductions can be achieved by decreasing the weight of the ship using composite materials rather than steel, since composites have a higher weight-to-stiffness ratio.

The aim of this study is to investigate the suitability of sandwich composite shells as structural members of cylindrical or spherical tanks by analysing stress distribution through the shell thickness and the shell deformations under pressure loading.

1 PRESSURIZED LIQUEFIED GAS TANKS

Liquefied gasses are defined as consisting of a broad range of petroleum gas mixtures, which, as listed in the rules of Turkish Lloyd [3], include: acetaldehyde, ammonia, butane, carbon dioxide, ethane, ethylene, nitrogen, refrigerant gasses, sulphur dioxide, etc.

Liquefied gas transportation distinguishes three major gas conditions: (i) fully pressurized (pressurized at ambient temperature), (ii) semi-refrigerated (pressurized and refrigerated at optimum temperature and pressure), (iii) fully refrigerated (refrigerated at or near atmospheric pressure). The loads associated with these liquefied gas conditions are one of the main characteristics that determine the pressurized tank design. For refrigerated tanks, the tank material's low-temperature toughness becomes the most important property to consider, since most materials become

*Corr. Author's Address: Turkish Naval Academy, Department of Naval Architecture, , Tuzla, 34942 Istanbul, Turkey, valankaya@dho.edu.tr

brittle below a certain temperature. Some liquefied gasses, such as ammonia, butane, propane, propylene and vinyl chloride, can be transported at ambient temperatures. Although the storage temperature is not considered for liquefied gasses, operating temperature caused by environmental conditions shall be taken into account in terms of stationary thermal loads. The operating temperature may give rise to significant thermal stresses. Therefore, each cargo tank is fitted with at least one liquid level gauging device, designed to operate at pressures not less than the maximum allowable relief valve setting at the temperatures within the cargo operating temperature range [3].

These liquefied gasses are transported via cylindrical or spherical cargo tanks at a vapour pressure of maximum 18 MPa, as indicated by Fujitani et al. [2]. In this study, the main loading is considered to be the maximum vapour pressure, ignoring thermal stresses caused by operating temperature and environmental conditions.

In addition to the liquefied gas storage temperature, tank design is also done according to the cargo tank arrangement restrictions from the International Code for the construction and equipment of ship carrying liquefied gasses in bulk (ICG code), incorporated into the Safety of life at sea (SOLAS) convention. According to the ICG code, liquefied gasses that do not need to be refrigerated, are restricted to Type C tanks, which are structurally independent of the ship's hull. Fig. 1 shows a generic mid-ship section view of a hull and cargo tank.

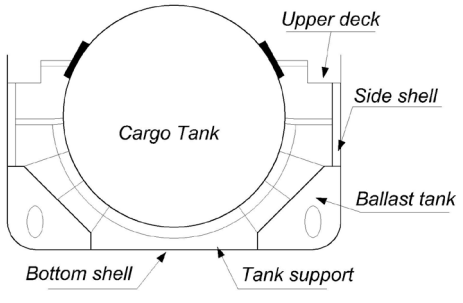

Fig. 1. *Mid-ship section of the hull and cargo tank*

Type C cargo tanks are completely self-supporting and do not form part of the ship's hull, nor do they contribute to the hull strength [2]. Similar applications of independent tanks are also common at liquefied natural gas (LNG) ships, as presented in Fig. 2. However LNG tanks, which store the gas at -162 °C, are not investigated in this study, because the refrigeration temperature effect on the tank material is beyond the scope of this study. Nevertheless, since LNG tanks are cylindrical and spherical in shape, the present methodology also could be applied to these tanks.

Fig. 2. *Hull-independent tank on an LNG carrier* [4]

2 COMPOSITE MATERIALS

As presented by Mouritz et al. [5], composite materials can be chosen for several functional components of ships, such as hull (complete or partial as for bulkheads), superstructure (complete for small crafts, or partial for bigger crafts), for the mast, for the propulsion system components, and even for propellers.

One major reason for these choices is the composites' high stiffness-to-weight ratio, which reduces the components weight; another reason is the lower cost of moulding complex geometry parts rather than machining them.

Moreover, the design flexibility inherent in composite laminates, which is described as tailoring by Kabir et al. [6], makes composites a reasonable choice for obtaining optimum specific design requirements through a combination of structural/material concepts, stacking sequence, ply orientation, choice of the component phases, etc. These allow composites to provide modern solutions for thermal and acoustic insulation, stealth capabilities, shock resistance, etc.

When Liquefied Petroleum Gas (LPG) is in a hull-independent type C tank, no thermal insulation is required. Therefore, the design of the material can be tailored to be non-flammable and to bear the load while minimizing weight.

Utilization of composite materials, however, also brings difficulties to the analyst, such as the inter-laminar or transverse shear stress due to mismatch of material properties among layers, bending-stretching coupling due to lamination asymmetry, and in-plane orthotropy. The transverse stress and strain components are ignored in classical or thin shell theories, which makes these theories inadequate

for the analysis of thicker shells. Hence, reliable prediction of deformations and stresses for thicker structures require the use of higher order shear deformation theories, which are based on a cubic or higher expansion of the in-plane displacements. Higher order theories introduce additional unknowns that are difficult to interpret in physical terms and require more mathematical computations for finding solutions [7] and [8].

As indicated by Youssif [9], to analyse the effects of design sensitivities efficiently and accurately, it is crucial to have the appropriate techniques associated with good structural models. Therefore, it is essential to develop a solution methodology considering the additional complexities arising by way of satisfying boundary conditions that cannot be handled by Navier's or Levy's traditional analytical approaches. Chaudhuri [10] provides the mathematical explanations for the boundary discontinuous type Fourier series approach for solving completely coupled system of partial differential equations, subjected to admissible general boundary conditions.

In this particular study, static deflections of cylindrical and spherical shaped pressurized tanks made of sandwich composites are investigated by using the higher order shear deformation theory. The effects of boundary conditions on the solution functions are introduced as described by Oktem and Chaudhuri [11] and the presented solution methodology is developed to apply to sandwich composites.

3 DEFINITION OF THE PROBLEM

The geometry of a composite shell, which consists of laminated plies with uniform thicknesses is shown in Fig. 3, where a and b represent the dimensions in the ξ_1, ξ_2 axes respectively, while ξ_3 is a line normal to the mid-surface defined at the centre going through the shell thickness h. The terms R_1 and R_2 are the mid-surface curvatures in the (ξ_1, ξ_2) axes respectively.

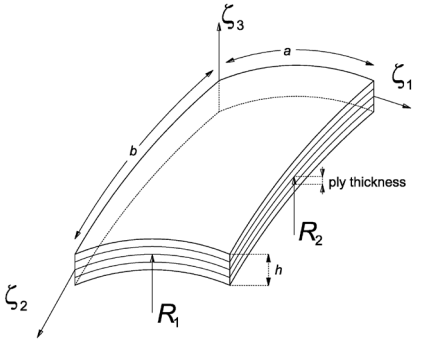

Fig. 3. *Rectangular panel geometry of a composite shell*

Fig. 4 shows the ply distance z from the mid-surface. The terms ϕ_1 and ϕ_2 are rotations about ξ_2 and ξ_1 axes, respectively. Details of the strain-displacement relations and other explanations are given by Reddy [12].

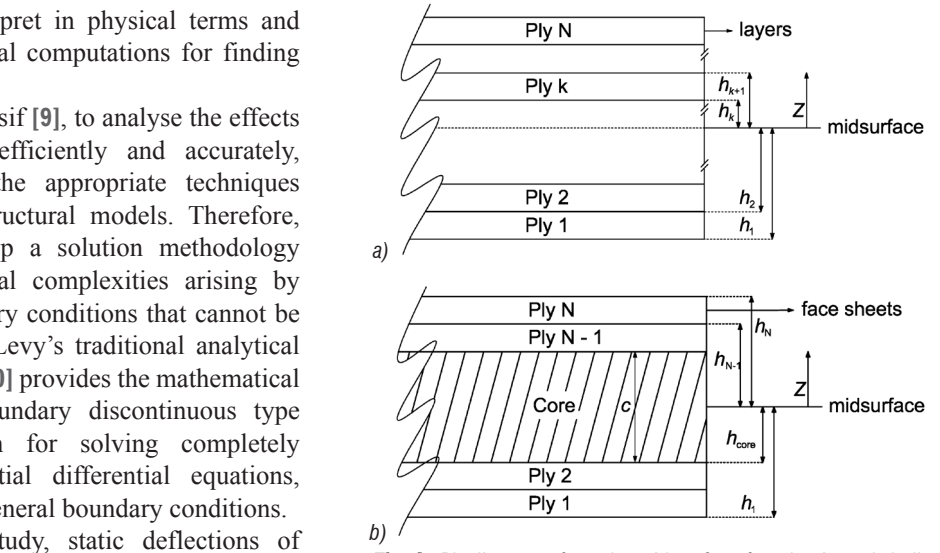

Fig. 4. *Ply distances from the mid-surface for a laminated shell; a)without a core, and b) with a sandwich core*

The displacement field by considering the cubic terms and satisfying the conditions of transverse shear stresses (and hence strains) vanishing at a point (ξ_1, ξ_2, $\pm h/2$) on the top and bottom surfaces of the shell, is given by Reddy [12] as follows:

$$u_1 = u(\xi_1,\xi_2,\xi_3) = u_0(\xi_1,\xi_2) + z\varphi_1(\xi_1,\xi_2) - \frac{4}{3h^2}z^3\left(\varphi_1 + \frac{\partial w_0}{\partial \xi_1}\right), \quad (1a)$$

$$u_2 = v(\xi_1,\xi_2,\xi_3) = v_0(\xi_1,\xi_2) + z\varphi_2(\xi_1,\xi_2) - \frac{4}{3h^2}z^3\left(\varphi_2 + \frac{\partial w_0}{\partial \xi_2}\right), \quad (1b)$$

$$u_3 = w(\xi_1,\xi_2,\xi_3) = w_0(\xi_1,\xi_2), \quad (1c)$$

where u, v, w represent displacements of a point at three axes ξ_1, ξ_2, ξ_3, while u_0, v_0, w_0 are displacements of a point at the mid-surface ($\xi_3 = 0$).

Equilibrium equations derived by using the principles of virtual work are given as follows [12]:

$$\frac{\partial N_1}{\partial \xi_1} + \frac{\partial N_6}{\partial \xi_2} = 0, \quad (2a)$$

$$\frac{\partial N_6}{\partial \xi_1} + \frac{\partial N_2}{\partial \xi_2} = 0, \quad (2b)$$

$$\frac{\partial Q_1}{\partial \xi_1}+\frac{\partial Q_2}{\partial \xi_2}-\frac{4}{h^2}\left(\frac{\partial K_1}{\partial \xi_1}+\frac{\partial K_2}{\partial \xi_2}\right)+$$
$$+\frac{4}{3h^2}\left(\frac{\partial^2 P_1}{\partial \xi_1^2}+\frac{\partial^2 P_2}{\partial \xi_2^2}+2\frac{\partial^2 P_6}{\partial \xi_1 \partial \xi_2}\right)=-q, \quad (2c)$$

$$\frac{\partial M_1}{\partial \xi_1}+\frac{\partial M_6}{\partial \xi_2}-Q_1+\frac{4}{h^2}K_1-\frac{4}{3h^2}\left(\frac{\partial P_1}{\partial \xi_1}+\frac{\partial P_6}{\partial \xi_2}\right)=0, \quad (2d)$$

$$\frac{\partial M_6}{\partial \xi_1}+\frac{\partial M_2}{\partial \xi_2}-Q_2+\frac{4}{h^2}K_2-\frac{4}{3h^2}\left(\frac{\partial P_6}{\partial \xi_1}+\frac{\partial P_2}{\partial \xi_2}\right)=0. \quad (2e)$$

In Eq. (2), q is the transverse load and N_i, M_i, P_i, $i=1,2,6$) denotes stress resultants, stress couples and second stress couples (see, e.g., Reddy **[12]**). Q_i ($i=1,2$) represents the transverse shear stress resultants. They are given as follows:

$$N_i=A_{ij}\varepsilon_j^0+B_{ij}\kappa_j^0+E_{ij}\kappa_j^2, \quad (i,j=1,2,6), \quad (3a)$$

$$M_i=B_{ij}\varepsilon_j^0+D_{ij}\kappa_j^0+F_{ij}\kappa_j^2, \quad (3b)$$

$$P_i=E_{ij}\varepsilon_j^0+F_{ij}\kappa_j^0+H_{ij}\kappa_j^2, \quad (3c)$$

$$Q_1=A_{5j}\varepsilon_j^0+D_{5j}\kappa_j^1, \quad (j=4,5), \quad (4a)$$

$$Q_2=A_{4j}\varepsilon_j^0+D_{4j}\kappa_j^1, \quad (4b)$$

$$K_1=D_{5j}\varepsilon_j^0+F_{5j}\kappa_j^1, \quad (4c)$$

$$K_2=D_{4j}\varepsilon_j^0+F_{4j}\kappa_j^1, \quad (4d)$$

in which A_{ij}, B_{ij}, etc. are the laminate rigidities (integrated stiffnesses). These are given as follows:

$$\left(A_{ij},B_{ij},D_{ij}\right)=\sum_{k=1}^{N}\int_{\xi_{k-1}}^{\xi_k}Q_{ij}^{(k)}\left(1,z,z^2\right)dz, \quad (5a)$$

$$\left(E_{ij},F_{ij},H_{ij}\right)=\sum_{k=1}^{N}\int_{\xi_{k-1}}^{\xi_k}Q_{ij}^{(k)}\left(z^3,z^4,z^6\right)dz. \quad (5b)$$

Generalized stress-strain constitutive relations for an orthogonal lamina can be expressed as follows:

$$\begin{Bmatrix}\sigma_1\\ \sigma_2\\ \sigma_6\\ \sigma_5\\ \sigma_4\end{Bmatrix}=\begin{bmatrix}Q_{11} & Q_{12} & 0 & 0 & 0\\ Q_{12} & Q_{22} & 0 & 0 & 0\\ 0 & 0 & Q_{66} & 0 & 0\\ 0 & 0 & 0 & Q_{55} & 0\\ 0 & 0 & 0 & 0 & Q_{44}\end{bmatrix}\begin{Bmatrix}\varepsilon_1\\ \varepsilon_2\\ \varepsilon_6\\ \varepsilon_5\\ \varepsilon_4\end{Bmatrix}, \quad (6a)$$

in which σ_1, σ_2, σ_6, σ_5, σ_4 are the stress and ε_1, ε_2, ε_6, ε_5, ε_4 are the strain components. Q_{ij} expressions in terms of engineering constants are given below:

$$Q_{11}=\frac{E_1}{1-\nu_{12}\nu_{21}}, \quad (6b) \qquad Q_{12}=\frac{\nu_{12}E_2}{1-\nu_{12}\nu_{21}}, \quad (6c)$$

$$Q_{22}=\frac{E_2}{1-\nu_{12}\nu_{21}}, \quad (6d) \qquad Q_{66}=G_{12}, \quad (6e)$$

$$Q_{44}=G_{23}, \quad (6f) \qquad Q_{55}=G_{13}. \quad (6g)$$

The introduction of Eqs. (3) and (4) into Eq. (2) gives five highly coupled fourth-order partial differential equations. The set of equations can be expressed in the following form:

$$K_{ij}x_j=f_i \quad (i,j=1,...,5) \quad \text{and} \quad (K_{ij}=K_{ji}), \quad (7a)$$

where

$$\left\{x_j\right\}^T=\left\{u_1 \;\; u_2 \;\; u_3 \;\; \phi_1 \;\; \phi_2\right\}, \quad (7b)$$

$$\left\{f_i\right\}^T=\left\{0 \;\; 0 \;\; -Q_{mn} \;\; 0 \;\; 0\right\}. \quad (7c)$$

Definitions of $[K_{ij}]$ elements are given in Appendix A. The load term (Q_{mn}) is a uniformly distributed load (the main load definition for pressurized tanks), and is defined as **[11]**:

$$Q_{mn}=\frac{16q}{\pi^2 mn}. \quad (8)$$

4 SOLUTION METHODOLOGY

A tank surface composed of cylindrical and spherical shells can simply be considered to be a doubly curved shell. If part of the tank shell, in the form of a rectangular panel, is inspected separately, the orthotropic shell cannot move in the longitudinal or transversal directions. However, rotations on the edges are possible. It is assumed that these constraints ensure that the following boundary conditions are true for all the edges of the selected shell part.

$$u_3(0,\xi_2)=u_3(a,\xi_2)=u_3(\xi_1,0)=u_3(\xi_1,b)=0, \quad (9a)$$

$$u_1(0,\xi_2)=u_1(a,\xi_2)=u_1(\xi_1,0)=u_1(\xi_1,b)=0, \quad (9b)$$

$$u_2(0,\xi_2)=u_2(a,\xi_2)=u_2(\xi_1,0)=u_2(\xi_1,b)=0, \quad (9c)$$

$$\phi_1(\xi_1,0)=\phi_1(\xi_1,b)=\phi_2(0,\xi_2)=\phi_2(b,\xi_2)=0, \quad (9d)$$

$$M_2(\xi_1,0)=M_2(\xi_1,b)=M_1(0,\xi_2)=M_1(b,\xi_2)=0. \quad (9e)$$

The particular solution to the boundary-value problem of an HSDT-based cross-ply shell assumes amplitudes U_{mn}, V_{mn} *and* W_{mn} at ξ_1, ξ_2, ξ_3 axes, respectively and X_{mn}, Y_{mn} for rotations about ξ_2 and ξ_1 axes. Solution functions are examined at the shell boundaries through the length a and width b of the shell geometry and organized solution functions at the boundaries are settled by equalities [12].

$$u_1(\xi_1,\xi_2)=\sum_{m=0}^{\infty}\sum_{n=1}^{\infty}U_{mn}\Re_1(\xi_1,\xi_2),\quad \begin{matrix}0<\xi_1<a,\\ 0\le\xi_2\le b,\end{matrix} \tag{10a}$$

$$u_2(\xi_1,\xi_2)=\sum_{m=1}^{\infty}\sum_{n=0}^{\infty}V_{mn}\Re_2(\xi_1,\xi_2),\quad \begin{matrix}0\le\xi_1\le a,\\ 0<\xi_2<b,\end{matrix} \tag{10b}$$

$$u_3(\xi_1,\xi_2)=\sum_{m=1}^{\infty}\sum_{n=1}^{\infty}W_{mn}\Re_3(\xi_1,\xi_2),\quad \begin{matrix}0\le\xi_1\le a,\\ 0\le\xi_2\le b,\end{matrix} \tag{10c}$$

$$\varphi_1(\xi_1,\xi_2)=\sum_{m=0}^{\infty}\sum_{n=1}^{\infty}X_{mn}\Re_1(\xi_1,\xi_2),\quad \begin{matrix}0\le\xi_1\le a,\\ 0\le\xi_2\le b,\end{matrix} \tag{10d}$$

$$\varphi_2(\xi_1,\xi_2)=\sum_{m=1}^{\infty}\sum_{n=0}^{\infty}Y_{mn}\Re_2(\xi_1,\xi_2),\quad \begin{matrix}0\le\xi_1\le a,\\ 0\le\xi_2\le b,\end{matrix} \tag{10e}$$

where,

$$\Re_1(\xi_1,\xi_2)=cos(\alpha\xi_1)sin(\beta\xi_2), \tag{11a}$$

$$\Re_2(\xi_1,\xi_2)=sin(\alpha\xi_1)cos(\beta\xi_2), \tag{11b}$$

$$\Re_3(\xi_1,\xi_2)=sin(\alpha\xi_1)sin(\beta\xi_2), \tag{11c}$$

$$\alpha=\frac{m\pi}{a},\qquad \beta=\frac{n\pi}{b}. \tag{11d}$$

The next step is substituting assumed particular solutions (Eq. (10)) into equilibrium Eq. (2). The differentiation procedure for these functions is based on Lebesque integration theory, which introduces boundary Fourier coefficients arising from discontinuities of the particular solutions at the edges. As has been noted by Chaudhuri [10], the boundary Fourier coefficients serve as a complementary solution to the problem under investigation. The partial derivatives, which cannot be obtained by term-wise differentiation, are given by Oktem and Chaudhuri [11], as follows,

$$u_{1,1}=-\sum_{m=1}^{\infty}\sum_{n=1}^{\infty}\alpha U_{mn}\,sin(\alpha\xi_1)sin(\beta\xi_2), \tag{12}$$

$$u_{1,11}=\frac{1}{2}\sum_{m=1}^{\infty}\overline{c_m}\,sin(\beta\xi_2)+$$
$$+\sum_{m=1}^{\infty}\sum_{n=1}^{\infty}\left\{-\alpha^2U_{mn}+\overline{a_n}\gamma_m+\overline{b_n}\delta_m\right\}sin(\alpha\xi_1)cos(\beta\xi_2), \tag{13}$$

$$u_{1,111}=-\sum_{m=1}^{\infty}\sum_{n=1}^{\infty}\alpha\left\{-\alpha^2U_{mn}+\overline{a_n}\gamma_m+\overline{b_n}\delta_m\right\}\times$$
$$\times sin(\alpha\xi_1)sin(\beta\xi_2), \tag{14}$$

$$u_{2,2}=-\sum_{m=1}^{\infty}\sum_{n=1}^{\infty}\beta V_{mn}\,sin(\alpha\xi_1)sin(\beta\xi_2), \tag{15}$$

$$u_{2,22}=\frac{1}{2}\sum_{m=1}^{\infty}\overline{c_m}\,sin(\alpha\xi_2)+$$
$$+\sum_{m=1}^{\infty}\sum_{n=1}^{\infty}\left\{-\beta^2V_{mn}+\overline{c_m}\gamma_n+\overline{d_m}\delta_n\right\}sin(\alpha\xi_1)cos(\beta\xi_2), \tag{16}$$

The boundary Fourier coefficients ($\overline{a_n}$, $\overline{b_n}$) etc., which appear in Eqs. (8) to (12), are defined in Appendix B. The remaining partial derivatives can be obtained by term-wise differentiation.

The resulting equations are supplied by the geometric and natural boundary conditions, which are presented by Oktem and Chaudhuri [11], and are not rewritten here to keep the presentation shorter.

5 NUMERICAL RESULTS AND DISCUSSIONS

Numerical results are presented for composites, for which laminates have a cross-ply [0°/90°] arranged carbon fibres impregnated in an epoxy resin prepreg, with the polyurethane foam core material of varying thicknesses. The doubly-curved shell geometry includes cylindrical and spherical tank forms. The applied loading is a pressure with a value of 18 MPa, which is the maximum storage pressure for LPG carriers [2].

For the numerical solutions, commercially available materials are chosen. The following material properties are provided from their producers. Carbon epoxy prepreg is used for face sheets and generic polyurethane foam for core layers.

Table 1. *Material properties of the face sheets and the core*

Part	Material	Property
Face Sheets	Carbon Epoxy (AS4/3501-6 [0°/90°]s)	E=68.3 GPa, ν=0.05 (at 121 °C)
Core	Polyurethane foam	E=225 MPa, G=67.2 MPa (at 70 °C)

Here E is the in-plane Young's modulus, and G denotes in-plane shear modulus while v is major Poisson's ratio.

In the calculations, the following normalized quantities are defined:

$$u_3^* = (10^3 Eh^3 / p_0 a^4) u_3, \quad (17a)$$

$$M_1^* = (10^3 / p_0 a^2) M_1, \quad (17b)$$

$$\sigma_1^* = 10(h^2 / p_0 b^2) \sigma_1, \quad (17c)$$

in which a and b are the edge length values of the panel, and p_0 denotes the transverse load. For the numerical results presented in the tables and figures, the normalized quantities are computed at the centre of the panel.

Varying values of shallowness ratio R/L (radius / length) and thickness ratio a/h (edge-length / thickness) are considered to show the effect of geometry changes. In addition, the effect of the core thickness is investigated by means of stress distribution through the thickness of the shell.

The solution methodology requires the control of convergence in order to define the required number of terms to include in the equations. Fig. 5 shows the convergence of the normalized central transverse displacement u_3^* and the moment M_1^* of a moderately thick $a/h=10$ symmetric cross-ply $[0°/90°]_s$ sandwich shell, having a core thickness c ratio $a/c=10$ under a pressure loading of 18 MPa. The normalized displacement u_3^* and moment M_1^* exhibit a fast convergence. Nonetheless, the selected number of terms to be used in the numerical analyses is $n=m=40$.

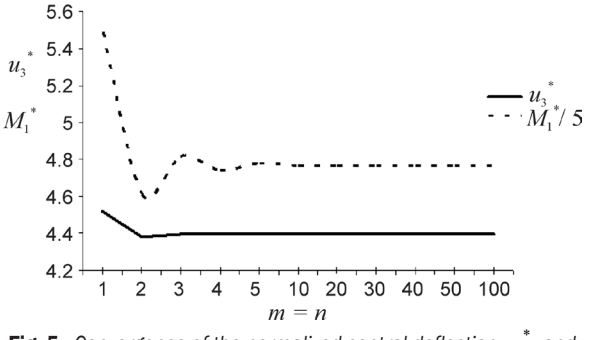

Fig. 5. *Convergence of the normalized central deflection u_3^* and moment M_1^* for a symmetric moderately thick cross-ply $[0°/90°]_s$ sandwich shell*

The obtained results are compared to the results of the counterpart analyses using the first order shear deformation theory (FSDT) and the finite element analyses (FEA). The computer program used for validation purposes is the commercially available FEA software ANSYS. Shell geometry is modeled with R/L=10 shallowness at both radii R_1 and R_2, and with the ANSYS shell 91 element type with the sandwich option activated. Uniformly distributed loading is applied as pressure loading over the shell surface. The FEA layered shell model is presented in Fig. 6.

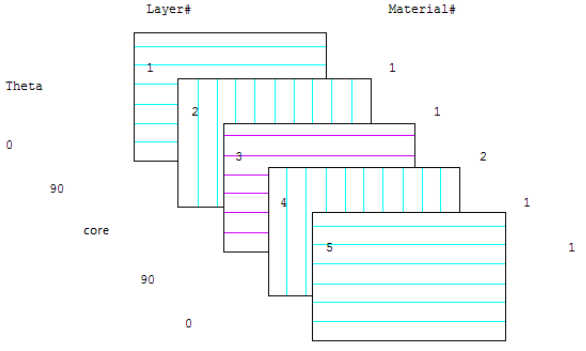

Fig. 6. *Layered element model for a 0°/90°/core/90°/0° laminate*

The results of the present theory are in concordance with FEA and FSDT counterparts, as can be seen in Fig. 7, which compares varying a/h ratios by means of the normalized deflection u_3^* at the centre of the shell for the core material thickness ratio a/c of 10 and 100.

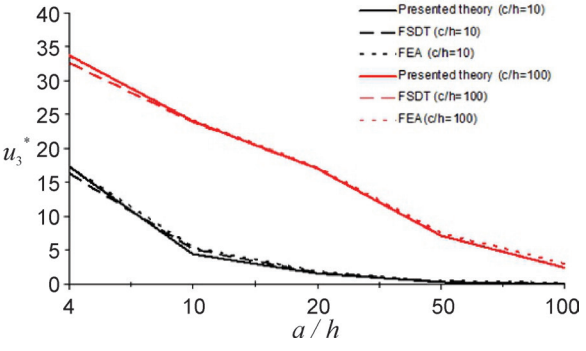

Fig. 7. *Results from the present theory compared to the FEA and FSDT counterparts for varying a / h ratios by means of the normalized deflection u_3^* at the centre of the shell*

The effect of changing the panel dimensions is investigated by analysing the deflection and moment values at the centre of the shell. The results are presented in Fig. 8 according to varying ratios of edge lengths a/b where increasing in this ratio causes the panel to become a beam. Major differences arise as a result of the effect of core material addition that was analyzed through central normalized deflections. Therefore, sandwich shells are suitable not only because they are stiff, but also because they can be

tailored to additional requirements, such as thermal insulation or fire retardancy of the core material.

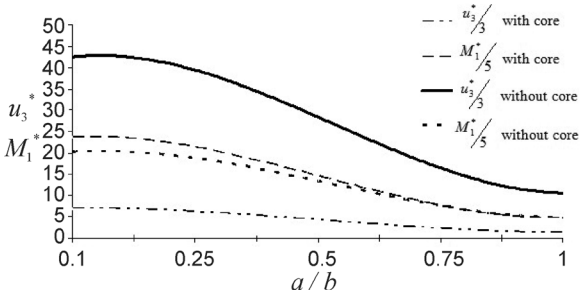

Fig. 8. *Variation of normalized deflection* u_3^* *and moment* M_1^* *with the a / b ratio*

The effect of varying the laminates thickness (Fig. 9) and the core material thickness (Fig. 10) ratios are investigated by analysing the doubly-curved shell centre normalized deflections.

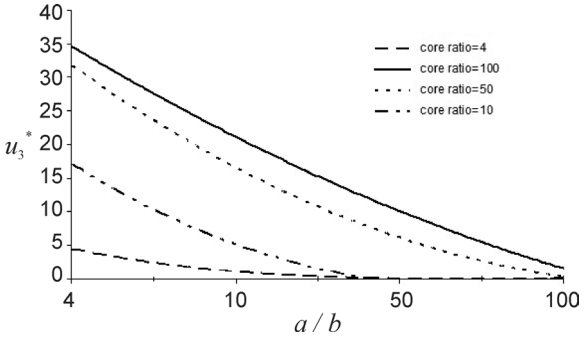

Fig. 9. *Variation of central normalized deflection* u_3^* *at varying face sheets thickness with different core thicknesses*

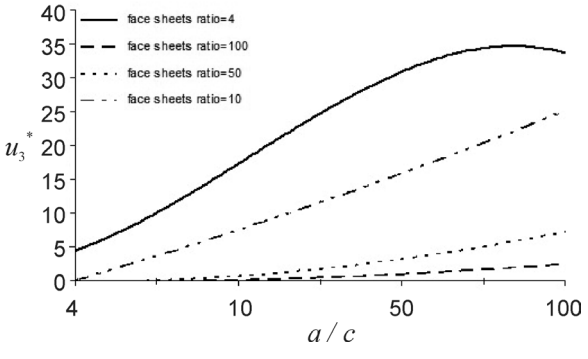

Fig. 10. *Variation of central normalized deflection* u_3^* *at varying core material thickness with different face sheets thicknesses*

The tank geometry curvature, in the vertical and horizontal inclination, is described by the shallowness ratio R/L. Referring to this ratio, the doubly curved panel has two radii R_1 and R_2, as presented in Fig. 3. In the case of a spherical tank, the radii are made equal $R_1 = R_2$, while a cylindrical tank is obtained by letting $R_1 \to \infty$ or $R_2 \to \infty$.

Setting both radii equal to infinity a flat plate is obtained. The effect of the shallowness ratio is presented in Fig. 11, which showing the normalized central deformations at varying R_1/L values for spherical and cylindrical shells.

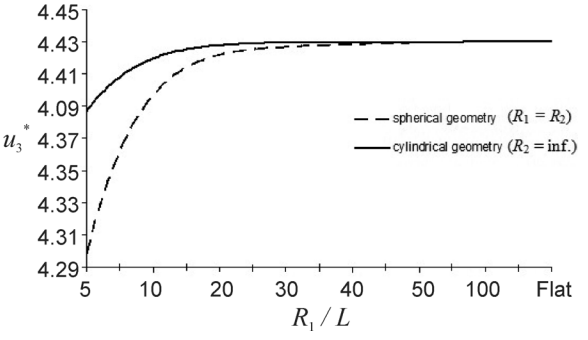

Fig. 11. *Variation of central normalized deflection* u_3^* *at varying shallowness ratios for spherical and cylindrical shells*

Fig. 12 shows the inter-laminar normalized stress values for different core thicknesses; for a moderately thick $a/h = 10$ symmetric [0°/90°/core/90°/0°] shell $R/L = 10$. While normalized stress reaches its maximum value at the top and bottom surfaces, the effect of the core material thickness is observed at the mid-surface of the shell.

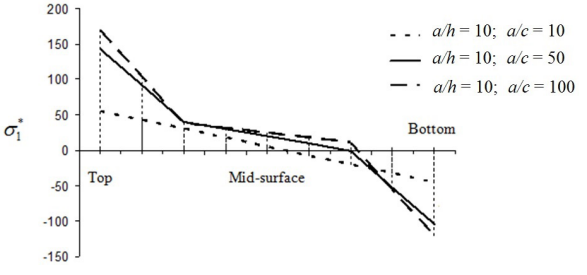

Fig. 12. *Effect of core thickness by means of normalized inter-laminar stress* σ_1^* *distribution at different core thicknesses*

6 CONCLUSIONS

An analytical solution to the problem of deformation of a finite-dimensional, cross-ply, thick, doubly curved sandwich shell is applied to fully pressurized composite LPG tanks. The mathematical model of the problem is solved using the boundary discontinuous generalized double Fourier series approach, and the results are in accordance with FSDT and FEA counterparts. Therefore, the presented analytical

method provides a benchmark solution for cylindrical and spherical fully pressurized composite LPG tanks.

Further results are concluded as follows:

- The predictive assessment of the developed solution methodology is shown by comparing the numerical application results of the FSDT and FEA solutions.
- Although FEA is widely used by various researchers, the present methodology, developed for cylindrical and spherical sandwich shells may be preferred due to its lower computational demand.
- The effect of core layer thickness on the normalized central deflection of the shell is remarkable. Therefore, core layer thickness, as one of the major parameters, can be used for varying LPG tank geometries.
- The effect of geometry, as another main parameter for tank design, has major effects on deflection values. Moreover, the curvature of the shell results in moderate changes on a central deflection.
- The effect of core layer thickness over the inter-laminar stress distribution is also impressive. Increased thicknesses result in a notable decrease on inter-laminar stress distribution.

7 ACKNOWLEDGEMENT

CAD model of LNG carrier that is used in the article for demonstration purposes (Fig.2) is provided by SEFT Ship Design, a leading company on maritime and naval design programs in Turkey. The author would like to express a deep sense of appreciation and gratitude to General Manager Mr Semih Zorlu for his kind cooperation and help.

8 REFERENCES

[1] U.S. Energy Administration Annual Energy Outlook (2014). from *http://www.eia.gov*, accessed on 2015-01-15)

[2] Fujitani, T., Emi, H., Abe, A. (2003). *Ship Design and Construction*. The Society of Naval Architects and Marine Engineers, Jersey City, Chapter 32.

[3] urkish Lloyd (2014). The rules of Turkish Lloyd, *from http://www.turkloydu.org*, accessed on 2015-01-15.

[4] Seft (2014). SEFT Ship Design, *from http://www.seft.com.tr,* accessed on 2015-01-15.

[5] Mouritz, A.P., Gellert, E., Burchill, P., Challis, K. (2001). Review of advanced composite structures for naval ships and submarines. *Composite Structures*, vol. 53, no. 1, p. 21-41, **DOI:10.1016/S0263-8223(00)00175-6**.

[6] Kabir, H.R.H., Al-Khaleefi, A.M., Chaudhuri, R.A. (2001). Free vibration analysis of thin arbitrarily laminated anisotropic plates using boundary-continuous displacement Fourier approach. *Composite Structures*, vol. 53, no. 4, p. 469-476, **DOI:10.1016/S0263-8223(01)00059-9**.

[7] Chen, C.S. (2007). The nonlinear vibration of an initially stressed laminated plate. *Composites: Part B Engineering*, vol. 38, no. 4, p. 437-447, **DOI:10.1016/j.compositesb.2006.09.002**.

[8] Khalili, S.M.R., Davar, A., Fard, K.M. (2012). Free vibration analysis of homogeneous isotropic circular cylindrical shells based on a new three-dimensional refined higher order theory. *International Journal of Mechanical Sciences*, vol. 56, no. 1, p. 1-25, **DOI:10.1016/j.ijmecsci.2011.11.002**.

[9] Youssif, Y.G. (2009). Non-linear design and control optimization of composite laminated doubly curved shell. *Composite Structures*, vol. 88, no. 3, p. 468-480, **DOI:10.1016/j.compstruct.2008.05.020**.

[10] Chaudhuri, R.A. (2002). On the roles of complementary and admissible boundary constraints in Fourier solutions to boundary-value problems of completely coupled rth order PDEs. *Journal of Sound and Vibration*, vol. 251, no. 2, p. 261-313, **DOI:10.1006/jsvi.2001.3913**.

[11] Oktem A.S., Chaudhuri, R.A. (2008). Effect of inplane boundary constraints on the response of thick general (unsymmetric) cross ply laminates. *Composite Structures*, vol. 83, no. 1, p. 1-12, **DOI:10.1016/j.compstruct.2007.03.002**.

[12] Reddy, J.N. (2003). *Mechanics of Laminated Composite Plates and Shells: Theory and Analysis*, 2nd ed. CRC Press, Boca Raton.

9 APPENDIX A

Definitions of $[K_{ij}]$:

$$K_{11} = A_{11}\frac{\partial^2}{\partial\xi_1^2} + A_{66}\frac{\partial^2}{\partial\xi_2^2}, \tag{A1}$$

$$K_{12} = \left(A_{12} + A_{66}\right)\frac{\partial^2}{\partial\xi_1\partial\xi_2}, \tag{A2}$$

$$K_{13} = \left(\frac{A_{11}}{R_1} + \frac{A_{12}}{R_2}\right)\frac{\partial}{\partial\xi_1} - c_1E_{11}\frac{\partial^3}{\partial\xi_1^3} - \left(2c_1E_{66} + c_1E_{12}\right)\frac{\partial^3}{\partial\xi_1\partial\xi_2^2}, \tag{A3}$$

$$K_{14} = \left(B_{11} - c_1E_{11}\right)\frac{\partial^2}{\partial\xi_1^2} + \left(B_{66} - c_1E_{66}\right)\frac{\partial^2}{\partial\xi_2^2}, \tag{A4}$$

$$K_{15} = \left(B_{12} - c_1E_{12} + B_{66} - c_1E_{66}\right)\frac{\partial^2}{\partial\xi_1\partial\xi_2}, \tag{A5}$$

$$K_{22} = A_{66}\frac{\partial^2}{\partial\xi_1^2} + A_{22}\frac{\partial^2}{\partial\xi_2^2}, \tag{A6}$$

$$K_{23}=\left(\frac{A_{12}}{R_1}+\frac{A_{22}}{R_2}\right)\frac{\partial}{\partial\xi_2}-$$
$$-c_1E_{22}\frac{\partial^3}{\partial\xi_2^3}-(2c_1E_{66}+c_1E_{12})\frac{\partial^3}{\partial\xi_1^2\partial\xi_2}, \quad \text{(A7)}$$

$$K_{24}=\left(B_{12}-c_1E_{12}+B_{66}-c_1E_{66}\right)\frac{\partial^2}{\partial\xi_1\partial\xi_2}, \quad \text{(A8)}$$

$$K_{25}=\left(B_{66}-c_1E_{66}\right)\frac{\partial^2}{\partial\xi_1^2}+\left(B_{22}-c_1E_{22}\right)\frac{\partial^2}{\partial\xi_2^2}, \quad \text{(A9)}$$

$$K_{33}=\left[\begin{array}{l}A_{55}-6c_1D_{55}+9c_1^2F_{55}+\\ c_1\left(\frac{E_{12}}{R_1}+\frac{E_{22}}{R_2}\right)+c_1\left(\frac{E_{11}}{R_1}+\frac{E_{12}}{R_2}\right)\end{array}\right]\frac{\partial^2}{\partial\xi_1^2}+$$
$$+\left[A_{44}-6c_1D_{44}+9c_1^2F_{44}+2c_1\left(\frac{E_{12}}{R_1}+\frac{E_{22}}{R_2}\right)\right]\frac{\partial^2}{\partial\xi_2^2}-$$
$$-9c_1^2H_{11}\frac{\partial^4}{\partial\xi_1^4}-2c_1^2(H_{12}+2H_{66})\frac{\partial^4}{\partial\xi_1^2\partial\xi_2^2}-$$
$$-c_1^2H_{22}\frac{\partial^4}{\partial\xi_2^4}-\left[\left(\frac{A_{11}}{R_1^2}+\frac{A_{12}}{R_1R_2}\right)+\left(\frac{A_{12}}{R_1R_2}+\frac{A_{22}}{R_2^2}\right)\right]\square \quad \text{(A10)}$$

$$K_{35}=\left[\begin{array}{l}A_{44}-6c_1D_{44}+9c_1^2F_{44}-\\ \frac{1}{R_1}\left(B_{12}-c_1E_{12}\right)-\frac{1}{R_2}\left(B_{22}-c_1E_{22}\right)\end{array}\right]\frac{\partial}{\partial\xi_2}+$$
$$+c_1\left(F_{22}-c_1H_{22}\right)\frac{\partial^3}{\partial\xi_2^3}+$$
$$+\left[c_1\left(F_{12}-c_1H_{12}\right)+2c_1\left(F_{66}-c_1H_{66}\right)\right]\frac{\partial^3}{\partial\xi_1^2\partial\xi_2}, \quad \text{(A11)}$$

$$K_{35}=\left[\begin{array}{l}A_{44}-6c_1D_{44}+9c_1^2F_{44}-\\ \frac{1}{R_1}\left(B_{12}-c_1E_{12}\right)-\frac{1}{R_2}\left(B_{22}-c_1E_{22}\right)\end{array}\right]\frac{\partial}{\partial\xi_2}+$$
$$+c_1\left(F_{22}-c_1H_{22}\right)\frac{\partial^3}{\partial\xi_2^3}+$$
$$+\left[c_1\left(F_{12}-c_1H_{12}\right)+2c_1\left(F_{66}-c_1H_{66}\right)\right]\frac{\partial^3}{\partial\xi_1^2\partial\xi_2}, \quad \text{(A12)}$$

$$K_{44}=\left[D_{11}-2c_1F_{11}+c_1^2H_{11}\right]\frac{\partial^2}{\partial\xi_1^2}+$$
$$+\left[D_{66}-2c_1F_{66}+c_1^2H_{66}\right]\frac{\partial^2}{\partial\xi_2^2}-$$
$$-\left(A_{55}+6c_1D_{55}+9c_1^2F_{55}\right), \quad \text{(A13)}$$

$$K_{45}=\left[\begin{array}{l}D_{12}-c_1F_{12}+D_{66}-c_1F_{66}-\\ c_1\left(F_{12}-c_1H_{12}\right)-c_1\left(F_{66}-c_1H_{66}\right)\end{array}\right]\frac{\partial^2}{\partial\xi_1\partial\xi_2}, \quad \text{(A14)}$$

$$K_{55}=\left[D_{66}-2c_1F_{66}+c_1^2H_{66}\right]\frac{\partial^2}{\partial\xi_1^2}+$$
$$+\left[D_{22}-2c_1F_{22}+c_1^2H_{22}\right]\frac{\partial^2}{\partial\xi_2^2}-$$
$$-A_{44}+3c_1D_{44}+3c_1\left(D_{44}-3c_1F_{44}\right), \quad \text{(A15)}$$

where;

$$\left(A_{ij},B_{ij},D_{ij}\right)=\sum_{k=1}^{N}\int_{\xi_{k-1}}^{\xi_k}Q_{ij}^{(k)}\left(1,z,z^2\right)dz, \quad \text{(A16)}$$

$$\left(E_{ij},F_{ij},H_{ij}\right)=\sum_{k=1}^{N}\int_{\xi_{k-1}}^{\xi_k}Q_{ij}^{(k)}\left(z^3,z^4,z^6\right)dz, \quad \text{(A17)}$$

$$c_1=-\frac{4}{3h^2}. \quad \text{(A18)}$$

10 APPENDIX B

Definition of boundary Fourier coefficients

$$\overline{a_n}=\frac{4}{ab}\int_0^b\left[u_1\left(a,\xi_2\right)-u_1\left(0,\xi_2\right)\right]cos\left(\beta\xi_2\right)d\xi_2, \quad \text{(B1)}$$

$$\overline{b_n}=-\frac{4}{ab}\int_0^b\left[u_1\left(a,\xi_2\right)-u_1\left(0,\xi_2\right)\right]cos\left(\beta\xi_2\right)d\xi_2, \quad \text{(B2)}$$

$$\overline{c_m}=\frac{4}{ab}\int_0^a\left[u_{2,2}\left(\xi_1,b\right)-u_{2,2}\left(\xi_1,0\right)\right]sin\left(\alpha\xi_1\right)d\xi_1, \quad \text{(B3)}$$

$$\overline{d_m}=-\frac{4}{ab}\int_0^a\left[u_{2,2}\left(\xi_1,b\right)+u_{2,2}\left(\xi_1,0\right)\right]sin\left(\alpha\xi_1\right)d\xi_1. \quad \text{(B4)}$$

Strojniški vestnik - Journal of Mechanical Engineering 62(2016)1, 41-50

DOI:10.5545/sv-jme.2015.3051 Original Scientific Paper
Received for review: 2015-09-21
Received revised form: 2015-11-03
Accepted for publication: 2015-11-19

The Influence of Extrusion Ratio on Contact Stresses and Die Elastic Deformations in the Case of Cold Backward Extrusion

Tomaž Pepelnjak[1,*] – Mladomir Milutinović[2] – Miroslav Plančak[2] – Dragiša Vilotić[2] – Saša Randjelović[3] – Dejan Movrin[2]

[1] University of Ljubljana, Faculty of Mechanical Engineering, Slovenia
[2] University of Novi Sad, Faculty of Technical Sciences, Serbia
[3] University of Niš, Mechanical Engineering Faculty, Serbia

In this paper, the distribution of contact stresses along the die-workpiece interface as well as elastic deformation behavior of the die in the cold backward extrusion of steel billets have been investigated both experimentally and numerically. For the experiments, a special tooling set including a pin load cell measuring device was designed and made. Contact stresses were recorded at various points in time and at various locations during the extrusion process, i.e. for different punch strokes (part's bottom thickness). The research focus was on determining the extrusion ratio's influence on the distribution of the contact stresses and therefore the experiments were performed using five punches of different head diameters. In the next step, based on the measured contact stresses, radial displacements of the inner die wall were calculated by applying Lame's equation. Furthermore, an extended finite element analysis of the investigated extrusion process was carried out using Simufact.forming software. The results of numerical simulations for the contact stresses were compared with experiments. The benefits and weaknesses of the pin load cell measuring technique and Lame's formula when it is employed for determination of the die elastic deformation were also examined, as well as were the contribution of the die elastic deformation to dimensional errors of the extruded parts.

Keywords: backward extrusion, contact stresses, die elastic deformation, pin load cell, finite element method

Highlights

- *Direct measurement of die loading.*
- *Die loading analysis - experimental and numerical.*
- *Analytical model for the calculation of elastic deformation of the die.*
- *Influence of extrusion ratio on die loading.*

0 INTRODUCTION

Cold extrusion is a forming technology that enables mass production of parts in a wide range of shapes and dimensions with increased mechanical properties and narrow tolerances, at lower costs. This is why the main consumers of cold extruded parts are the automotive, railway, aircraft, and military industries, in which cold extruded components are integral components of assemblies where dynamic load, and high levels of reliability and human safety are critical considerations [1] and [2].

In cold extrusion processes, the tool set is exposed to high contact stresses, which, in certain cases, may be limiting factors in applying this technology [3]. This is especially true for extruded steel samples. A high level of internal pressure and especially local stress concentration directly affect die wear occurrence, tooling damage and failure [4] as well changes in die geometry [5] which altogether result in poor part accuracy [6] and tool life [7]. The tooling concept, design, and manufacturing procedure also depend on the amount of acting stresses [8]. Therefore, in order to reduce problems and to design a tool set suitable for cold extrusion, tool loading should be thoroughly researched, particularly radial stresses at the die wall-workpiece interface [9]. A better understanding of the stress state in the die means greater possibilities for optimizing its design.

The stress state in the tooling elements during cold extrusion depends primarily on the die and punch geometry, material properties of the workpiece, and process conditions [2]. The stress state can be determined using several approaches. Basic information about tool set loading (stress distribution along the workpiece boundaries) may be obtained by theoretical methods (slab method, slip line, upper bound, etc.) [10]. This is the fastest and simplest way, but it is limited to a few cases of simple workpiece geometry. Furthermore, most of the theoretical solutions for contact stresses in extrusion are derived based on a number of assumptions and simplifications, which, in turn, may lead to a significant deviation from the real values.

A significant improvement in die stress analysis and design procedure has been achieved by introducing and developing numerical methods and computer-aided engineering (CAE) software. Simulation based on the finite element method (FEM) has made it possible to calculate the stress distribution

*Corr. Author's Address: University of Ljubljana, Faculty of Mechanical Engineering, Aškerčeva 6, SI-1000 Ljubljana, Slovenia, tomaz.pepelnjak@fs.uni-lj.si

at different cross sections of the die with the features of their shape and thermo-mechanical conditions taken into account [11] and [12], as well as to predict die damages and estimate tool life [13], to analyze die elastic deformation and the effects on part dimensional accuracy [14], and to optimize die geometry and pre-stressing procedures [15]. In some cases, FEM analysis is combined with certain methods of physical modeling [16] and artificial intelligence [17]. The goal is to gain more reliable data about loading, pressures and boundary conditions, which are then used as an input data for the simulation.

Experimental results for contact stresses are essential to verify the analytical and numerical calculations. For this reason, a lot of efforts have been invested in the development of experimental techniques and devices for determining contact stresses ranging from simple sensors and tooling with holes up to membrane system, profile foil method, pin load cell method, and strain gauges [18] and [19].

The main objective of this paper is to experimentally determine the intensity and distribution of the contact (radial) stress on the inner die wall in the case of backward cup extrusion of steel specimens for a wide range of the extrusion ratios and at the various points in the process development (various bottom thicknesses of the can). For that purpose a measuring device based on the pin load cell technique and special tooling with a set of inserts of different thicknesses have been designed and made. The pin load cell technique is one of the most reliable experimental methods for measuring contact stresses in metal forming operations since the measuring device is in direct contact with the extruded material [19]. This yields a dynamic output, which simulates the non-steady process conditions that are typical in these processes and enables the measurement of both normal and tangential stresses. This technique characterizes a relatively simple measuring procedure since minimal modifications in the design of the tool set are needed. Basic details of the pin load techniques and some technical problems associate with its use are elaborated in this paper. Furthermore, an extensive analysis of the stress-strain state of the extrusion die including the process simulation was performed employing Simufact.forming software based on FEM. Finally, based on the measured contact stresses, the die elastic deformations in the radial direction were calculated by using Lame's equation and compared with FEM results in order to evaluate the accuracy of this approach. Relevant data related to the stress-stain state of the extrusion die are essential to properly design both the die and process parameters. Therefore, the findings could also be valuable to engineers in the forming industry in addition to the academic community.

1 THE PIN LOAD CELL MEASURING TECHNIQUE

The principal scheme of the pin load cell technique and a photo of the device assembly are given in Figs. 1 and 2, respectively.

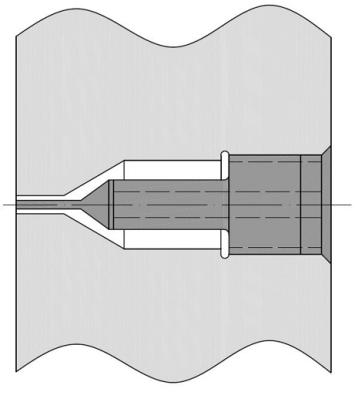

Fig. 1. *Pin load cell built into the die wall*

The pin load cell (Fig. 2) device consists of a small cylindrical pin (1), strain gauge (2), and threads (3). The cylindrical pin passes through the designated hole in the die body and its head/tip (top surface) is aligned with the inner surface of the die wall thus enabling full contact with the workpiece material. During the forming process, the workpiece material pushes (presses) the pin head causing elastic compression of the pin and remaining part of the cell. This compression is measured by strain gauges (2) attached to the lower part of the cell.

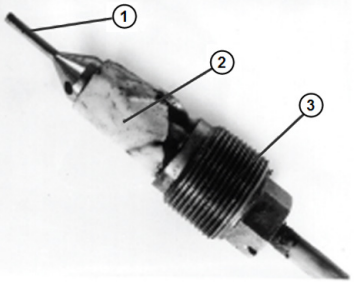

Fig. 2. *Pin load cell device with main components: (1) pin, (2) strain gauge, (3) thread*

The effectiveness of this technique and the accuracy of the measured contact stress depends on several factors, one of which is the friction occuring between the pin and die hole. It comes from tangential

stresses acting on the pin head during the forming process. Since the calibration procedure does not take into account friction force (pre-calibration is performed only using normal force), any pressure drop due to friction cannot be detected. In order to reduce this friction and measurement uncertainty, the clearance between the pin and the die hole should be as large as possible. However, this may lead to another problem – the risk of the workpiece material being extruded in the gap between pin and hole. This is an undesirable feature, because it hampers the pin movement inside the hole. So, a compromise has to be made regarding the radial clearance between pin and hole.

The axial pin head position relative to the die surface during the forming process is very sensitive to the rigidity of the pin assembly and the die (Fig. 3). The difference in the rigidity may cause more or less deviation of the measured contact stress from the real value. If the pin head and die surface are leveled before deformation ($\Delta h = 0$, Fig. 3), then the following situations are possible during deformation:

a) The rigidity of the pin assembly is greater than the rigidity of the die. Therefore the die deforms elastically more than the pin assembly and the pin protrudes from the die ($+\Delta h$). This results in a measured value that is higher than the actual one as the pin is not only loaded by the material directly above its head (N), but also by the surrounding material.

b) The rigidity of the pin assembly is less than the rigidity of the die. In this case the pin head is below the die surface ($-\Delta h$) and indicates lower stress values as it is loaded by only a portion of the material above its head (N), whereas the surrounding area of the die undergoes loading from (M).

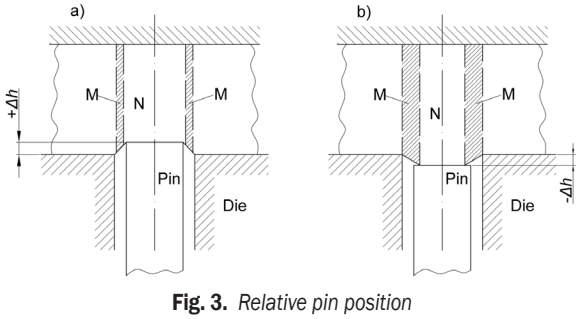

Fig. 3. *Relative pin position*

c) The rigidity of the pin assembly and the die are equal. The same rigidity yields the same elastic deformations i.e. the pin head and die surface are the same level (Δh=0) and the pin produces an output which gives the correct values of the normal contact stress. This is considered to be an ideal case.

2 EXPERIMENTAL

Measuring the radial contact stresses using the pin load cell device at different points on the die wall during backward extrusion is possible in two ways:

1. using a tool with two or more pin load cells built into the die wall;
2. using a tool with only one pin load cell and replaceable die bottoms of various thickness.

The main drawback of the first variant with two or more pin loads is weakening of the die. Therefore, in the present investigation, the second option is chosen.

The tooling set used in the experiment is shown in Fig. 4. Five different die bottoms of various thicknesses are used in order to simulate five different contact points between the workpiece and the die. The locations (the axial distance from the bottom of the measuring points (A – E) are given in Fig. 5. At each point, the measurement was repeated for five different instantaneous positions of the punch i.e. the punch strokes (s = 2 mm, 4 mm, 10 mm, 14 mm and 18 mm, see Fig. 5). The face shape of the punch was a flat/conical face shape and designed according to the recommendation of the International Cold Forging Group [2].

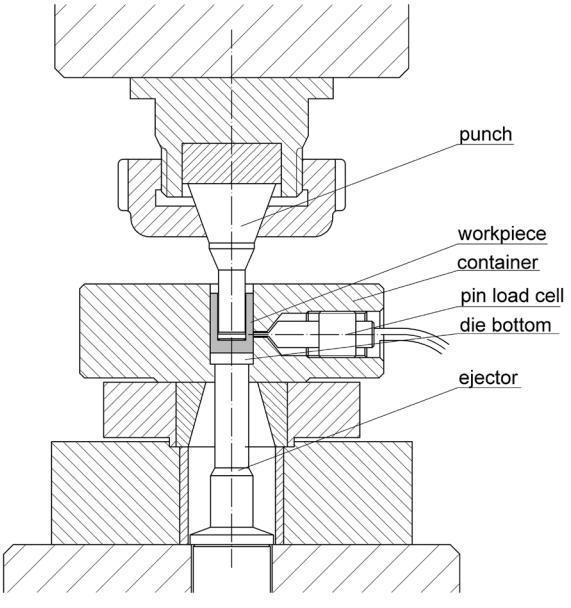

Fig. 4. *Scheme of the tooling*

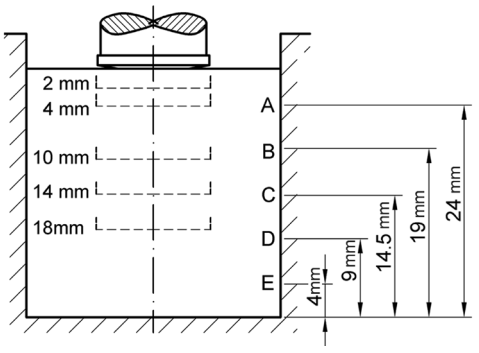

Fig. 5. *Locations of measuring points*

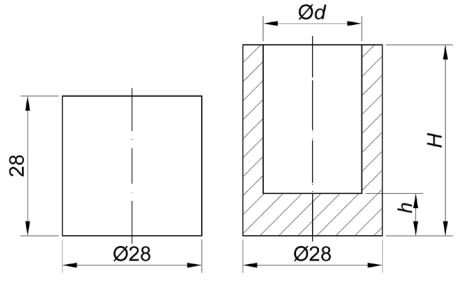

Fig. 6. *Billet and workpiece geometry*

Cylindrical billets (Ø28 mm × 28 mm) made from low carbonated steel (1.0401 according to EN 10027-2 **[20]**) were used in the experiment. All billets were soft annealed and phosphate coated, with molybdenum disulphide (MoS_2) applied as a lubricant. The geometry of the billet and workpiece is given in Fig. 6. The inner diameter of the workpiece was also varied at five levels according to the Table 1, in which the corresponding values of the extrusion ratio and true strain are given. The punches and die were made from tool steel 1.2601 according to **[20]**, the hardness after heat treatments were 60HRC and 58HRC, respectively.

Table 1. *Punch geometry and process parameters*

Punch diameter d [mm]	12	14.25	16.85	18.80	20.33
Extrusion ratio $e_p = A_0/(A_0-A_1)$	1.22	1.35	1.57	1.82	2.11
True strain $\varepsilon = \ln(A_0/(A_0-A_1))$	0.2	0.3	0.45	0.6	0.75

3 FEM ANALYSES

Backward extrusion was also investigated by numerical simulation using a commercial software package and FEM. The applied software enables detailed analysis of forming processes from different aspects including simulation of tool behavior. Recent developments of remeshing methods and advances in computational technology have further upgraded capability and efficiency of this technique and the software, as well as the accuracy of the obtained results **[21]**.

The focus of the FEA is on the die radial stress distribution and load, which effect the elastic deformation of the die during the investigated process. During simulation, an axially-symmetric 2D FEM model of the backward extrusion was used. The modeling procedure started with the creation of a 3D model of the tooling and workpiece in CAD software SolidEdge which was then imported into the simulation package. Elastic-plastic material behavior for the workpiece was chosen as the punch and the dies were treated as elastic bodies. The flow curve in the analytic form necessary for FEM simulation was obtained by the Rastegaev compression test. A suitable tool steel from the simulation database was selected for the punch and die material. The meshing procedure was initially performed under different mesh criteria as well as different sizes and types of elements with the goal of checking the convergence of the numerical solution. Finally, after a few iterations, the advancing Front Quad mesher and the quad elements with a size of 1 mm for the workpiece, as well "quadtree mesher" and the quad elements of 2.1 mm for the die and the punch were chosen. The remeshing of the starting elements was executed in the most highly deformed zones of the workpiece at every five increments in order to minimize the effect of tool penetration through the elements due to large workpiece deformations. Coupled thermo-mechanical FEM analysis is performed under low friction conditions ($\mu = 0.09$).

4 RESULTS

4.1 Radial Stresses at the Container Wall

Radial stress distributions at the container wall for five different instantaneous punch positions (2 mm, 4 mm, 10 mm, 14 mm, and 18 mm) and five different punch diameters (12 mm, 14.25 mm, 16.85 mm, 18.80 mm, and 20.33 mm), obtained by FE analysis and experimentally, are shown in Figs. 7 to 11. The experimental distribution curves were obtained based on measurements taken at 5 points on the wall, according to Fig. 5.

As an example (Fig. 7), if the punch with a diameter of 12 mm ($e_p = 1.22$, $\varepsilon = 0.2$) travels for 4 mm, the value of the radial stress at point "D" of the

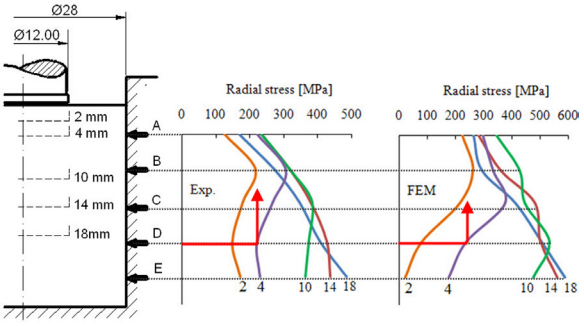

Fig. 7. *Distribution of radial stresses at inner die wall vectors for e_p = 1.22 (ε =0.2)*

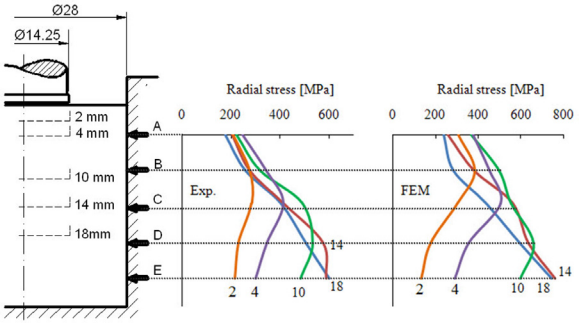

Fig. 8. *Distribution of radial stress at inner die wall for e_p =1.35 (ε =0.3)*

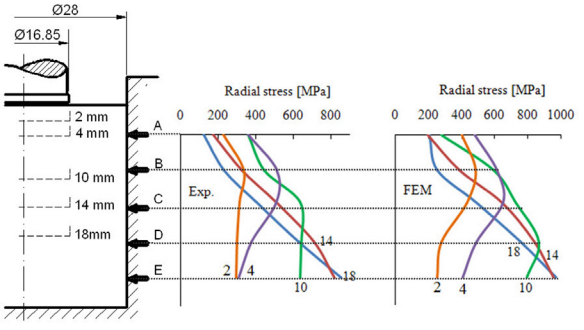

Fig. 9. *Distribution of radial stress at inner die wall for e_p =1.57 (ε =0.45)*

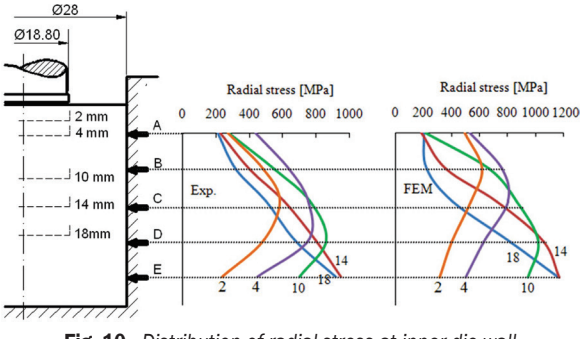

Fig. 10. *Distribution of radial stress at inner die wall for e_p =1.82 (ε =0.6)*

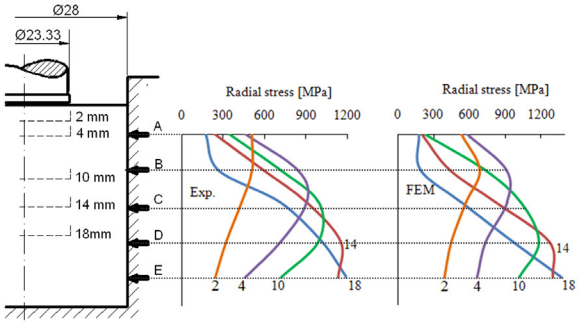

Fig. 11. *Distribution of radial stress at inner die wall for e_p =2.11 (ε =0.75)*

container wall is 220 MPa (experimental), i.e. 240 MPa (FEM).

Generally, it could be concluded that every point on the container wall is subjected to radial stress whose value is changeable and depends on the instantaneous position of the punch head. The maximal amount of σ_r at a given point appears at the moment when the punch head is at a certain distance from this position and corresponds to the point of maximal contact pressure. Basically, a higher σ_r corresponds to a higher extrusion ratio e_p. The highest σ_r values always occur at the end of the backward extrusion process, i.e. when the punch has reached its final position (in the current study this is the 18 mm punch stroke). Fig. 12 shows the relationship between the maximal radial stress at the container wall $\sigma_{r,max}$ and the extrusion ratio e_p obtained by FE and experimentally. It can be seen that this stress increases from the initial value of 484 MPa (Exp.) i.e. 588 MPa (FEM) to the absolute maximal amount of 1195 MPa (Exp.) and 1372 MPa (FEM), respectively.

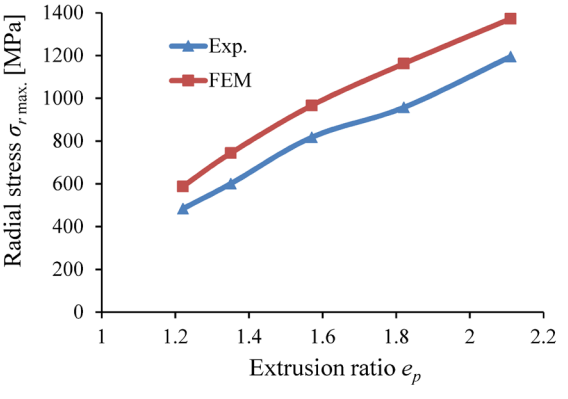

Fig. 12. *Maximal radial stresses against extrusion ratio*

A comparison between FE and the experimental results shows that the FE analysis gives somewhat

higher σ_r values (15 % to 20 %) than the experimental measurements. This discrepancy can be attributed to inaccurate calibration of the pin load cell, friction between the pin and pin hole, as well as to the improper modeling of materials and boundary conditions in FEA.

4.2 Die Elastic Deformation

Contact pressure acting on the die wall results in its elastic deformation. Positive elastic radial displacement of the internal die wall introduces positive dimensional errors to both the inner and outer diameter of the extruded cup [6]. In addition, since the contact pressure is variable along the axial direction, the radial displacement of the internal die wall also vary, i.e. the die wall profile will differ from the nominal one. Therefore, an exact prediction of die elastic behavior during forming process is a key factor for improving the accuracy of cold formed components [22].

If radial contact stresses on the inner die wall are known, then die radial displacement (Δr) can be evaluated using Lame's formula, Eq. (1) [14]. The formula was originally derived for determination of the stress-strain state in the case of a thick cylinder subjected to internal pressure only, but it is often used to solve different engineering problems in the area of elastic mechanics [18]. In this paper, the profile of the inner die wall was determined by substituting the measured contact stresses into Lame's formula.

Thus the elastic radial displacement is:

$$\Delta r = r \cdot e_\theta = \frac{p_i \cdot r^2}{E\left(R^2 - r^2\right)}\left[\left(1-\nu\right)+\left(1+\nu\right)\frac{R^2}{r^2}\right]r, \quad (1)$$

where p_i is internal pressure (at inner surface $p_i = -\sigma_r$), e_θ circumferential strain, r inner diameter of the die, R outer diameter of the die, E Young's modulus of the die material (E = 210 GPa) and ν Poisson's ratio (ν = 0.29).

The layout of the die wall radial elastic displacements for different punch positions (punch stroke s) in the case of the extrusion ratio e_p = 2.11 (ε = 0.75) obtained by FEM simulation is depicted in Fig. 13. Pictures show that the change in the die geometry is most evident on the part of the inner die wall (and zone around) where maximal radial stresses act. This region moves down, expanding radially with the punch stroke (see also Fig. 11). In contrast, the rest of the die volume remains almost undeformed during

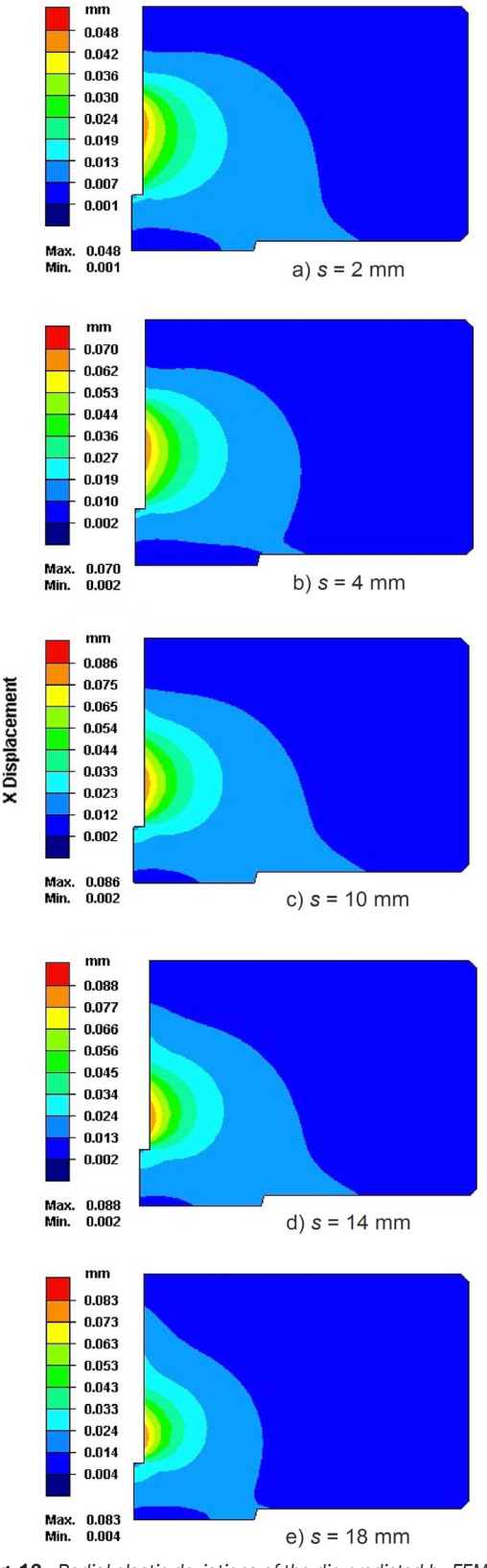

Fig. 13. *Radial elastic deviations of the die predicted by FEM (extrusion ration e_p = 2.11)*

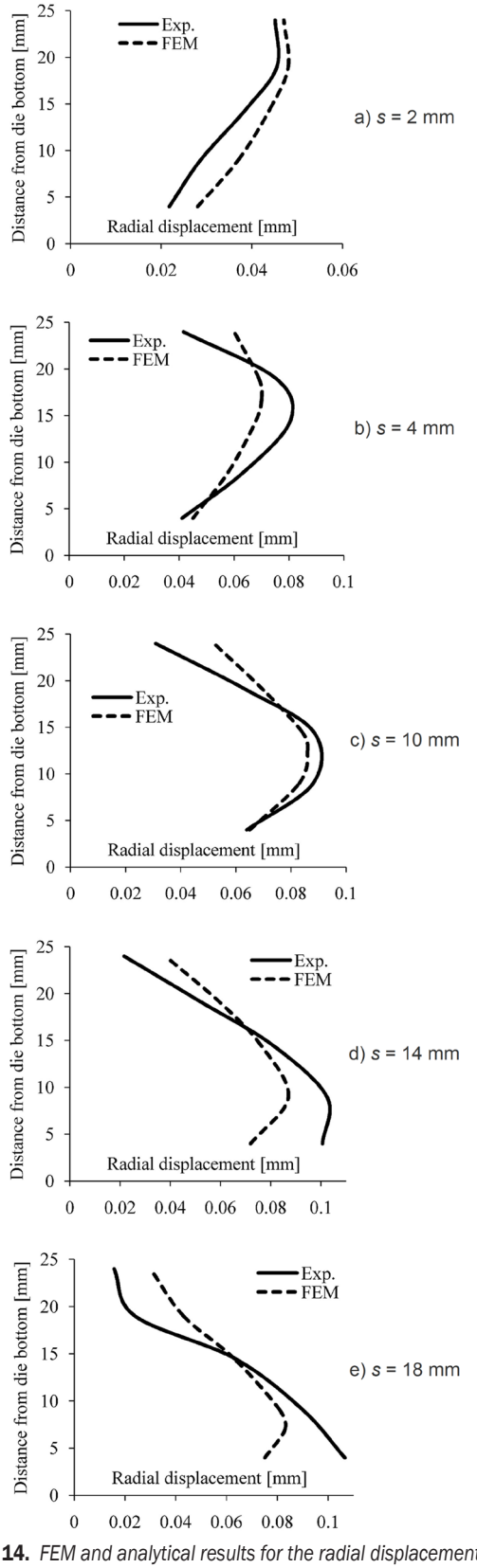

Fig. 14. *FEM and analytical results for the radial displacement of the inner die wall (e_p = 2.11)*

the entire extrusion process. As expected, the minimal die displacement occurs at the outer die wall.

A comparison of Δr values predicted by FEM and obtained analytically by Eq. (1), for e_p = 2.11, is given in Fig. 14. In Eq. (1), the experimental values of radial stress p_i are substituted. As it can be seen, the analytically calculated die profile is directly proportional to the experimentally obtained pressure distribution, as the rest of the Eq. (1) is constant. The maximum radial displacement (Δr = 0.1065 mm) is related to the maximum punch stroke (s = 18 mm) and to the point of maximal measured radial stress. On the other hand, the profile predicted by FEM indicates that there is some discrepancy in the distribution of radial strain and radial stress. These differences arise with the punch stroke. Maximal displacement of the internal die wall (Δr = 0.088 mm) is not found at the maximal punch stoke (s = 18 mm) and the point of the maximal predicted radial stress (Fig. 11), but rather at the punch stroke s = 14 mm. The reason for this is the die geometry, i.e. an increase in die stiffness in the area near the die bottom due to reduction of the die inner diameter. For a punch stroke of 18 mm the point of maximum radial stress is closer to the die bottom compared to the punch stroke of 14 mm and thus the maximal radial deformation is smaller.

The change in die stiffness along the axial axis could not be taken into account in Eq. (1), which has a negative effect on the accuracy of the solution. Furthermore, Lame's formula is developed with the assumption that any section of the cylinder will remain plane before and after the application of pressure, i.e. that strain along the axial axis is constant. Since this precondition is not met here it can be considered as an additional source of inaccuracy in the analytical solution.

Another drawback of the analytical solution is related to the impossibility of considering die surface hardness, which influences the die elastic behavior significantly. The results are generally higher values of the maximal radial displacement (except for s = 2 mm) compared to the FEM ones (Fig. 14) even though experimentally recorded values of the contact stresses are lower than FEM predicted (Fig. 11). This can be attributed to strong intermolecular bonds, which occur in the case of hardened material due to which both local elasto-plastic and overall elastic deformation are considerably reduced, as well as the influence of local peaks of contact stresses to the surface curvature. A much better illustration of the hardening effect on material elastic behavior is given in Fig. 15, where the radial displacements of the die made from hardened (Fig. 15b real case) and non-hardened (Fig.

15a demo case) material (predicted by FEM, punch stroke 18 mm) are shown. Comparing both results, the difference in the maximum values is more than obvious.

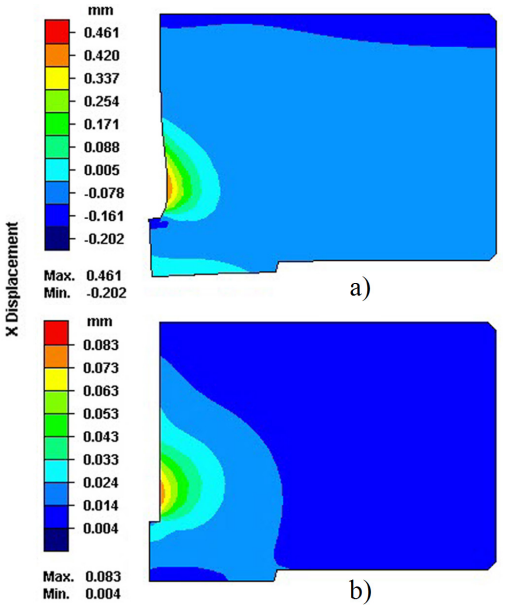

Fig. 15. *Radial displacement of the die in the case of non-hardened (a) and hardened (b) material (e_p = 2.11, s = 18 mm)*

Table 2 shows the maximal elastic displacements of the inner die wall (Δr_{max}) for all five extrusion ratios and related in terms of international tolerance grade (IT) in order to display the influence of elastic deviation of the inner die wall on workpiece dimensional errors more transparently. Note that the maximal radial deviation of the inner die wall, i.e. the workpiece's outer surface, corresponds to IT8 to IT11 grades, which could be considered as a significant loss of accuracy. Therefore, in order to obtain proper dimensions of the final part, the elastic deformation of the die must be taken into account when designing the extrusion process. It should be noted that loss of tolerance of the workpiece is even greater than indicated in Table 2 due to the material elastic recovery after ejecting the workpiece from the die (Fig. 16).

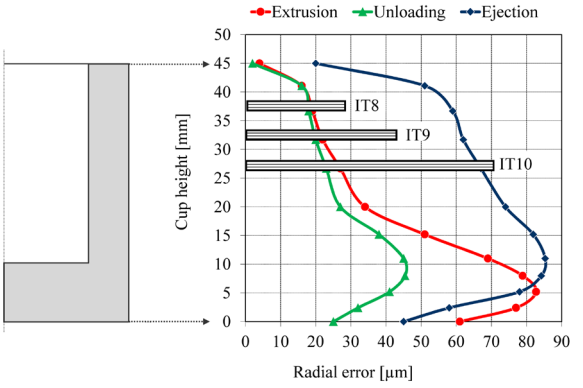

Fig. 16. *FEM predicted radial errors of the extruded cup (punch stroke s = 18 mm; e_p = 2.11)*

5 CONCLUSIONS

Knowledge of die loading, especially contact pressure distribution along the die-workpiece interface, is one of the key factors for the correct design of a cold extrusion process. Loading influences both die life and the accuracy of the formed part.

In this paper, an efficient procedure to measure contact radial stresses on the inner die wall at various points in time and at various locations during the backward extrusion process is presented. For this purpose, a special device (a pin load cell inserted in the die with replaceable bottoms of various thicknesses) was designed. Experiments were performed using steel billets, with punches of different diameters.

Table 2. *Maximal radial deviation of the die inner wall*

		Δr_{max} [mm] (s = 2 mm)	Δr_{max} [mm] (s = 4 mm)	Δr_{max} [mm] (s = 10 mm)	Δr_{max} [mm] (s = 14 mm)	Δr_{max} [mm] (s = 18 mm)
e_p = 2.11	Exp.	0.045 (IT10)	0.080 (IT11)	0.088 (IT11)	0.102 (IT11)	0.106 (IT11)
	FEM	0.048 (IT10)	0.070 (IT10)	0.086 (IT11)	0.088 (IT11)	0.083 (IT11)
e_p = 1.82	Exp.	0.051 (IT10)	0.067 (IT10)	0.076 (IT11)	0.084 (IT11)	0.081 (IT11)
	FEM	0.042 (IT9)	0.056 (IT10)	0.068 (IT10)	0.069 (IT10)	0.065 (IT10)
e_p = 1.57	Exp	0.030 (IT9)	0.045 (IT10)	0.057 (IT10)	0.073 (IT11)	0.076 (IT11)
	FEM	0.032 (IT9)	0.045 (IT10)	0.057 (IT10)	0.057 (IT10)	0.054 (IT10)
e_p = 1.35	Exp.	0.025 (IT9)	0.037 (IT9)	0.048 (IT10)	0.052 (IT10)	0.053 (IT10)
	FEM	0.025 (IT8)	0.034 (IT9)	0.044 (IT10)	0.046 (IT10)	0.042 (IT9)
e_p = 1.22	Exp.	0.019 (IT8)	0.027 (IT8)	0.034 (IT9)	0.039 (IT9)	0.043 (IT9)
	FEM	0.017 (IT7)	0.025 (IT8)	0.030 (IT9)	0.036 (IT9)	0.035 (IT9)

The influence of the punch position on the value and location of the maximal radial stress has been investigated. Furthermore, the analyzed process was simulated using Simufact.forming software.

Experimental and FEM results indicate that the radial stress distribution on the die wall surface during the extrusion is non-uniform. The values of the radial stress depend on the punch position and increases with increases in the punch stroke, whereas the peak is always located at the point just below the instantaneous position of the punch head. The influence of the extrusion ratio on the stress intensity is also noticeable. When e_p increases, the peak value increases too: there is a more than twofold difference in the maximal radial stresses for the minimal (e_p = 1.22) and maximal (e_p = 2.11) extrusion ratio. A comparison of the FEM and experimental findings shows that the FEM predictions are 15 % to 20 % higher. There is very good agreement in the form of the stress distribution.

Another aim of the paper was to verify whether Lame's theory can accurately determine the elastic deformation of the extrusion dies. The results for the radial displacement of the inner die wall obtained by FEM and analytically by substituting the experimental values for the radial stress in Lame's formula differ significantly. This can be explained by the failure of Lame's equation to take into account different parameters such as variable die geometry and material hardness effect. Hence, it can be concluded that this solution is best applied in cases where the die has a simple geometry (uniform inner section profile) and uniform distribution of radial stress along the die wall, while for dies having complex shapes a more accurate theoretical model or different techniques like FEM are needed. Loss of tolerance due to the die elastic deformation may reach IT11 grade.

6 ACKNOWLEDGEMENTS

The authors thank the CEEPUS program for helping with mobility within the framework of the network CIII-HR-0108.

7 REFERENCES

[1] Vilotić, D., Plančak, M., Kuzman, K., Milutinović, M., Movrin, D., Skakun, P., Luzanin, O. (2007). Application of net shape and near-net shape forming technologies in manufacture of roller bearing components and cardan shafts. *Journal for Technology of Plasticity*, vol. 32, no. 1-2, p. 87-104.

[2] Altan, T., Ngaile, G., Shen, G. (eds.) (2004). *Cold and Hot Forging: Fundamentals and Application*s. ASM International, Materials Park.

[3] Groenbaek, J., Hinsel, Ch. (2001) The importance of optimized pre-stressing with regard to the tool performance in precision forging. *3rd International Conference on Industrial Tool*s, Celje, p. 41-48.

[4] Hayakawa, K., Nakamura, T., Tanaka, S. (2004) Analysis of fatigue crack initiation and propagation in cold forging tools by local approach of fracture. *Materials Transaction*s, vol. 45, no. 2, p. 461-468, **DOI:10.2320/matertrans.45.461**.

[5] Lee, Y.S., Lee, J.H., Choi, J.U., Ishikawa, T. (2002). Experimental and analytical evaluation for elastic deformation behaviors of cold forging tool. *Journal of Materials Processing Technology,* vol. 127, no. 1, p. 73–82, **DOI:10.1016/S0924-0136(02)00268-6**.

[6] Lee, Y.S. Lee, J.H., Kwon, Y.N., Ishikawa, T. (2004) Analysis of elastic characteristics at the die and workpiece to improve the dimensional accuracy for cold forged part. *Journal of Materials Processing Technology*, vol. 153-154, p. 1081-1088, **DOI:10.1016/j.jmatprotec.2004.04.291**.

[7] Lange, K., Cser, L., Geiger, M., Kals, J.A.G. (1992). Tool life and tool quality in bulk metal forming. *CIRP Annals - Manufacturing Technology*, vol. 41, no. 2,, p. 667-675, **DOI:10.1016/S0007-8506(07)63253-3**.

[8] Milutinović, M., Movrin, D., Pepelnjak, T. (2012) Theoretical and experimental investigation of cold hobbing processes in cases of cone-like punch manufacturing. *The International Journal of Advanced Manufacturing Technology*, vol. 58, no. 9, p. 895-906, **DOI:10.1007/s00170-011-3457-5**.

[9] Randjelović, S., Manić, M., Trajanović, M., Milutinović, M., Movrin, D. (2012). The impact of die angle on tool loading in the process of cold extruding steel. *Materials and Technology*, vol. 46, no. 2, p. 149-154.

[10] Lange, K. (ed.) (1985) *Handbook of Metal Forming*, McGraw-Hill Inc., New York

[11] Behrens, B.-A., Bouguecha, A., Raedt, H.W., Hadifi, T. (2010). Numerical investigations on the fatigue failure of forging tools due to thermo-mechanical cyclic loading. *International Journal of Material Forming*, vol. 3, suppl. 1, p. 339-342, **DOI:10.1007/s12289-010-0776-2**.

[12] Brnic, J., Turkalj, G., Lanc, D., Canadija, M., Brcic, M., Vukelic, G., Munjas, N. (2013). Testing and analysis of X39CrMo17-1 steel properties. *Construction and Building Materials*, vol. 44, p. 293-301, **DOI:10.1016/j.conbuildmat.2013.02.080**.

[13] Geiger, M., Falk, B. (2001) Prediction of service life and failure probability of cold forging tools. *CIRP Annals - Manufacturing Technology*, vol. 50, no. 1, p. 173–176, **DOI:10.1016/S0007-8506(07)62098-8**.

[14] Long, H. (2006) Quantitative evaluation of dimensional errors of formed components in cold backward cup extrusion. *Journal of Materials Processing Technology*, vol. 177, no. 1-3, p. 591-595, **DOI:10.1016/j.jmatprotec.2006.04.079**.

[15] Kwan, C.T., Wang, C.C. (2011). An optimal pre-stress die design of cold backward extrusion by RSM Method. *Structural Longevity*, vol. 15, no. 1, p. 25-32.

[16] Vazquez, V., Altan, T. (2000). New concepts in die design - physical and computer modeling applications. *Journal of*

Materials Processing Technology, vol. 98, no. 2, p. 212-223, **DOI:10.1016/S0924-0136(99)00202-2**.

[17] Bingöl, S., Ayer, O., Altinbalik, T. (2015). Extrusion load prediction of gear-like profile for different die geometries using ANN and FEM with experimental verification. *The International Journal of Advanced Manufacturing Technology*, vol. 76, no. 5, p. 983-992, **DOI:10.1007/s00170-014-6328-z**.

[18] Milutinović, M. (2013). *Investigation of Part Accuracy in Cold Bulk Metal Forming Processes*, PhD thesis. University of Novi Sad, Faculty of Technical Sciences, Novi Sad.

[19] Vilotić, D., Plančak, M. (2011) Experimental tooling for contact stress measurement in bulk metal forming processes. *Journal for Technology of Plasticity*, vol. 36, no. 1, p. 9-16, **DOI:10.2478/v10211-011-0004-1**.

[20] EN-10027-2 (1992). *Designation Systems for Steels – Part 2: Steel Numbers*. European Committee for Standardisation, Brussels.

[21] Labergere, C., Rassineux, A., Saanouni, K. (2008) Improving numerical simulation of metal forming processes using adaptive remeshing technique. *International Journal of Material Forming*, vol. 1, suppl. 1, p.539-542, **DOI:10.1007/s12289-008-0255-1**.

[22] Milutinović, M., Vilotić, D., Pepelnjak, T. (2014). Part dimensional errors in free upsetting due to the elastic springback. *Tehnički vjesnik - Technical Gazette*, vol. 21, no. 1, p. 135-140.

Strojniški vestnik - Journal of Mechanical Engineering 62(2016)1, 51-59

DOI:10.5545/sv-jme.2015.3039 Original Scientific Paper
Received for review: 2015-09-21
Received revised form: 2015-12-07
Accepted for publication: 2015-12-10

An Algorithm of Form Deviation Calculation in Coordinate Measurements of Free-Form Surfaces of Products

Marek Magdziak*
Rzeszow University of Technology, Faculty of Mechanical Engineering and Aeronautics, Poland

The article presents the new method of form deviation calculation in the case of coordinate measurements of free-form surfaces of workpieces. The proposed algorithm of form deviation evaluation is based on the interpolation process of corrected measured points. Corrected measured points are the results of probe radius correction process applied in the coordinate measuring technique. The interpolation is conducted by using of the Lagrange and Chebyshev methods. The developed algorithm of deviation calculation can be implemented in most commercial software cooperating with a coordinate measuring machine. In the article the results of numerical and experimental investigations connected with the proposed algorithm are presented. The numerical investigations concern the simulation of contact coordinate measurements of products, which can be conducted on a coordinate measuring machine. The measured products are composed of free-form surfaces characterized by various curvature and consequently various degree of geometric complexity. The experimental investigations were conducted in order to verify the results of simulation studies. The presented method improves the accuracy of measurements of free-form surfaces of products.

Keywords: coordinate measuring technique, free-form surface, interpolation, form deviation

Highlights

- *The new method of form deviation calculation is presented.*
- *The algorithm is based on the interpolation of points by using of the Lagrange and Chebyshev methods.*
- *The shown algorithm improves the accuracy of measurements of free-form surfaces.*
- *The new method is compared to existing algorithms of form deviation assessment.*
- *The developed algorithm can be implemented in measurement software.*

0 INTRODUCTION

The coordinate measuring technique plays very important role in modern manufacturing processes of products. That technique can be used for example in reverse engineering processes, where the coordinate measuring technique can be used in order to digitize a product. The digitalization is performed at the beginning of a reverse engineering process of an object. Workpieces measured using the coordinate measuring technique can be produced by means of machining or rapid prototyping techniques. Measured products can be characterized by regular geometric shapes or can be composed of free-form surfaces [1] to [3]. Measurements of free-form surfaces can be divided into data acquisition and data processing [4]. The article concerns issues connected with the second stage of measurements – data analyzing.

Free-form surfaces are used in automotive and aerospace industries [5]. The examples of products with free-form surfaces, which can be measured using the coordinate measuring technique, are car body parts, turbine blades of aircraft engines and optic elements used in imaging systems [5] and [6]. The paper [5] contains the classification of free-form shape applications. The results of measurements of a machined free-form mould insert of an optical lens are presented in the paper [4]. The measurements were conducted by using of the intrinsic feature-based pattern analysis method dedicated to measuring ultra-precision free-form surfaces. Savio et al. [7] presented the results of measurements of a turbine blade. The aim of investigations was to establish the traceability of free-form measurements on coordinate measuring machines. The analyzed turbine blade was measured by using of different parameters associated with, for example, scanning speed and points density.

There can be distinguished a number of coordinate measuring gages, which can be used during coordinate measurements of curvilinear surfaces of most measured products. The examples of such measuring instruments are [5] and [8]:

- contact coordinate measuring machines (CMMs),
- redundant coordinate measuring gages (coordinate measuring arms, laser trackers),
- non-contact coordinate measuring machines (CMMs equipped with non-contact probing systems, measuring machines based on the photogrammetry, the laser triangulation or the computed tomography).

For measuring free-form optics very accurate coordinate measuring systems should be used. In the

*Corr. Author's Address: Rzeszow University of Technology, al. Powstańców Warszawy 12, 35-959 Rzeszów, Poland, marekm@prz.edu.pl

case of contact measurements CMMs with a resolution in nanometer range should be applied. Moreover, optical objects composed of free-form surfaces can be measured by using of probing systems mounted in ultra-precision manufacturing machines [6].

The accuracy of measurements with the use of above mentioned coordinate measuring gages can be influenced by the following factors:

- geometrical deviations of coordinate measuring instruments,
- deviations of measured products,
- environmental conditions in quality control departments,
- the inaccuracy of a probing system,
- applied measurement strategies,
- available algorithms included in measurement software cooperating with e.g. CMMs.

That factors are the sources of coordinate measurement uncertainty. Some of the mentioned factors are included in the standard [9], which concerns the method of determining the uncertainty of a coordinate measurement with the use of calibrated workpieces or measurement standards. The article contains an analysis of some issues connected with a measurement strategy and the inaccuracy of algorithms which are the part of commercial software of coordinate measuring gages.

Measurement software of modern coordinate measuring instruments may include, for example, various methods of probe radius correction process. That algorithms are intended to the calculation of coordinates of corrected measured points on the basis of coordinates of indicated measured points, which represent the center of a stylus tip of a contacting probing system. The corrected measured points should represent, as much as it is possible, the real shape of measured objects. The process of probe radius correction is the basis for contact coordinate measurements with the use of coordinate measuring machines or coordinate measuring arms. The real shape of a measured object has significant impact on the accuracy of coordinate measurements of free-form surfaces of workpieces. The wrong direction along which the probe radius correction process is conducted leads to the calculation of wrong coordinates of corrected measured points and consequently wrong measurement data [5]. There can be distinguished a large number of probe radius correction methods.

Liang and Lin [10] proposed the method for probe radius correction of a measuring probe stylus tip in the case of measuring curvilinear surfaces of products. That method consists in determining the set of triangles defined by indicated measured points localized on adjacent measurement paths. The unit normal vector which is being sought for a given point is computed in result of vector multiplication of vectors representing two sides of related triangle.

The authors of the paper [11] presented a method for determining the direction of probe radius correction based on measurements of two groups of points, each of them containing two points located at the other sides of a given indicated measured point at which a correction vector is being sought. Each group of points represents an individual, different direction of a measured surface and defines some individual vector. The direction for probe radius correction is computed using vector multiplication of already generated vectors determined from the information about the above mentioned two groups of points.

The references [12] and [13] present a method for computing a corrected measured point in the case of measurements of curves with a scanning measuring probe. The related algorithm uses subsequent locations of a measuring probe stylus tip working in a scanning mode. Based on those subsequent locations there is created an approximate outline of a measured profile by joining arcs being parts of a measuring stylus tip in its successive locations. The approximated corrected measured point, associated with an indicated measured point in a given location and setting of a measuring probe, is computed in the middle of an arc being a segment of the approximated outline of a measured profile.

The mentioned methods of a probe radius correction process are focused on identifying corrected measured points and do not take into account the algorithms of calculation of form deviations of measured workpieces, which can be composed of free-form surfaces. In the article the new method of assessing the accuracy of curvilinear surfaces of workpieces is presented. The proposed method may supplement developed methods of computing of corrected measured points.

In the next parts of the article selected existing methods of assessing form deviations, which are available in the chosen commercial software of a CMM and the results of performed investigations are presented. The simulation investigations concern the comparison of selected algorithms of product accuracy verification. The proposed method was compared to the existing methods of calculation of form deviations, which are available in the selected commercial software cooperating with a coordinate measuring machine. The simulation investigations were conducted with the use of arbitrarily selected workpieces containing free-form surfaces. On the

basis of gained results of performed research the statistical analysis was done.

The experimental investigations were conducted in order to verify the gained results of numerical research. They were performed by using of a selected coordinate measuring machine and different measurement parameters. The last parts of the paper contain the discussion and the conclusions regarding the results of conducted investigations and the possibility of using the proposed method of form deviation calculation in the coordinate measuring technique.

1 THE EXISTING METHODS OF ASSESING FORM DEVIATIONS

There is a large number of measurement software cooperating with coordinate measuring gages. In the second section of the article the existing methods of assessing form deviations are described in the case of the widely used Calypso measurement software, which is produced by the Carl Zeiss company.

The user of the considered measurement software is able to compute the values of a form deviation of free-form surfaces, which are the part of a measured object, by using of the following methods of form deviation calculation [14]:

- **a deviation in a nominal vector direction** – a local deviation is measured at each nominal point in the direction of a normal vector up to the intersection with an actual curve, which represents corrected measured points (the method denoted as the first method in the next parts of the article);
- **an actual-nominal deviation** – a local deviation is measured as the distance between the point located on an actual curve and a nominal curve (the method denoted as the second method).

The described methods of form deviation calculation were used during the investigations. Based on the recommendations of the producer the user of the measurement software should use in many measuring applications in the coordinate measuring technique mainly the first method of form deviation calculation. However, in that method, when measured free-form surfaces have the shape significantly different from the nominal one, the results of calculation of a form deviation substantially depend on the number of measured points [14].

In the case of the first method the point lying on a measured curve, which represents the real form of a measured product, is not the same point whose coordinates are registered by using of a coordinate measuring machine. The number of measured points in the first method of form deviation calculation is different than the number of points measured by using of a CMM. Similarly in the case of form deviation calculation based on measured points in the second method the number of nominal points does not correspond to the number of points, which is used in the case of the first method of form deviation calculation (Fig. 1). The information about the coordinates of both nominal and measured points is available in the 2D curve and 3D curve measurement elements. When increasing the number of measured points the accuracy of calculation of form deviations based on nominal points in the first method is getting higher. Unfortunately, the drawback of using this measurement software is that the user has no information about the type of a free-form curve which approximates measured points.

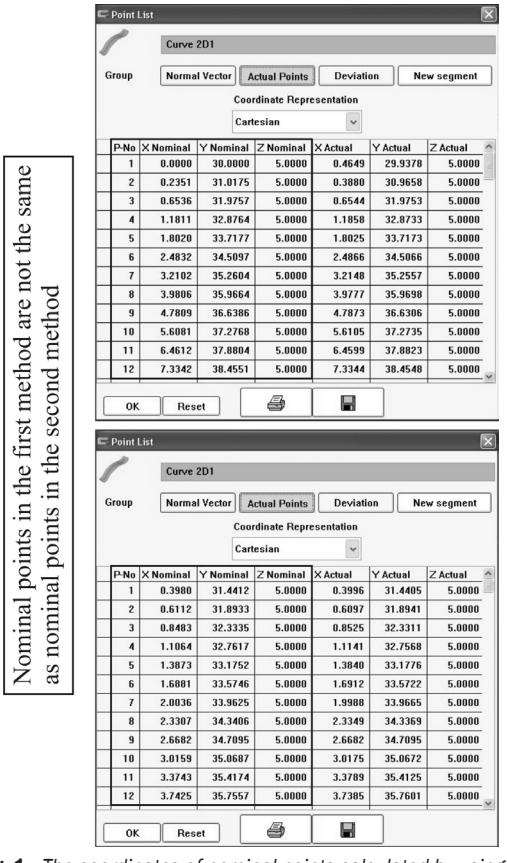

Fig. 1. *The coordinates of nominal points calculated by using of the first and the second methods*

2 THE NEW METHOD OF FORM DEVIATION CALCULATION

The new method of form deviation calculation of free-form surfaces of products is based on the evaluation of a local deviation, similar to the first method,

at nominal points of a measured workpiece. The application of the proposed method is presented on the basis of the Calypso measurement software. The considered method requires the information included in the 2D curve and 3D curve measurement elements, which are available in that software. The required information is exported from the above mentioned elements during the calculation of a form deviation using the first and the second methods. However, the new method can be implemented not only in the Calypso software. The data necessary for the proposed algorithm can be obtained from most measurement software.

The usage of the type of a measurement element depends most of all on the shape of a measured object. The 2D curve and 3D curve measurement elements have different normal vectors perpendicular to a surface of a measured product at its nominal points. When using the 2D curve measurement element normal vectors lie in a single plane. Therefore, that element does not take into account the curvature of a measured surface around measured free-form curves. The 3D curve element includes the information about the shape of a measured curvilinear surface near the section plane used to create the considered measurement element. Consequently, the 3D curve measurement element has the possibility of using normal vectors not lying in a single plane. Moreover, the 3D curve element allows the use of a nonuniform distribution of nominal points along measured free-form profiles based on their curvature.

In the new method of form deviation calculation the information about the coordinates of nominal points is exported from the above mentioned measurement elements when using the first commercial method of deviation estimation. The coordinates of corrected measured points are imported to the proposed method of form deviation calculation when using the second method. The proposed method includes all measured points obtained by using of a coordinate measuring machine.

The new method of form deviation calculation enables the interpolation of corrected measured points by using of the Lagrange and Chebyshev methods. That method divides points measured by a coordinate measuring machine into groups composed of five measured points. Those groups are interpolated using two mentioned interpolation methods. Therefore, there are constructed the groups of polynomial curves of a fourth degree, which represent the real shape of a measured workpiece in its individual cross-sections. In the next stage of the proposed method, after calculating interpolation curves, the deviations between nominal points and intersection points are calculated. The intersection points are created using interpolation curves and lines perpendicular to the measured profile of a workpiece at its nominal points. Therefore, the proposed method of form deviation estimation uses the information, apart from the coordinates of nominal and measured points, about normal vectors to free-form curves at nominal points. This information is taken from the first method of form deviation calculation. The user of the proposed method has the possibility of choosing the interpolation method of corrected measured points of free-form surfaces of products.

In the case of five interpolated measured points the interpolation function $F(x)$ and the base polynomials $T_0(x)-T_4(x)$ are written, using the Chebyshev interpolation method, with the following equations:

$$F(x)=a_0T_0(x)+a_1T_1(x)+a_2T_2(x)+ \\ +a_3T_3(x)+a_4T_4(x), \tag{1}$$

$$\begin{cases} T_0(x)=1 \\ T_1(x)=x \\ T_2(x)=2x^2-1 \\ T_3(x)=4x^3-3x \\ T_4(x)=8x^4-8x^2+1 \end{cases}. \tag{2}$$

The interpolation function is defined in the interval $\langle a,b\rangle$. Therefore, the interpolation polynomial should be scaled using the following equation:

$$x=\frac{2}{b-a}t-\frac{a+b}{b-a}. \tag{3}$$

In the case of the Lagrange interpolation method and five interpolated corrected measured points with coordinates (x_i,y_i) the interpolation function $L(x)$ is written with Eqs. (4) and (5).

$$L(x)=y_0L_0(x)+y_1L_1(x)+y_2L_2(x)+ \\ +y_3L_3(x)+y_4L_4(x). \tag{4}$$

The created method of form deviation calculation can be implemented as the new one in commercial software of a coordinate measuring machine. For example, the implementation can be done using the parameter coded measurements (PCM) module. That module has the possibility of using external applications, which take into account the proposed method.

$$\begin{cases} L_0(x) = \dfrac{(x-x_1)(x-x_2)(x-x_3)(x-x_4)}{(x_0-x_1)(x_0-x_2)(x_0-x_3)(x_0-x_4)} \\ L_1(x) = \dfrac{(x-x_0)(x-x_2)(x-x_3)(x-x_4)}{(x_1-x_0)(x_1-x_2)(x_1-x_3)(x_1-x_4)} \\ L_2(x) = \dfrac{(x-x_0)(x-x_1)(x-x_3)(x-x_4)}{(x_2-x_0)(x_2-x_1)(x_2-x_3)(x_2-x_4)} \\ L_3(x) = \dfrac{(x-x_0)(x-x_1)(x-x_2)(x-x_4)}{(x_3-x_0)(x_3-x_1)(x_3-x_2)(x_3-x_4)} \\ L_4(x) = \dfrac{(x-x_0)(x-x_1)(x-x_2)(x-x_3)}{(x_4-x_0)(x_4-x_1)(x_4-x_2)(x_4-x_3)} \end{cases}. \quad (5)$$

3 THE MEASURED WORKPIECES

There were performed the simulation investigations of coordinate measurements of selected products. The numerical research was done in order to verify the possibilities of using the developed algorithm of form deviation calculation. For each considered object there were extracted four free-form curves (Fig. 2).

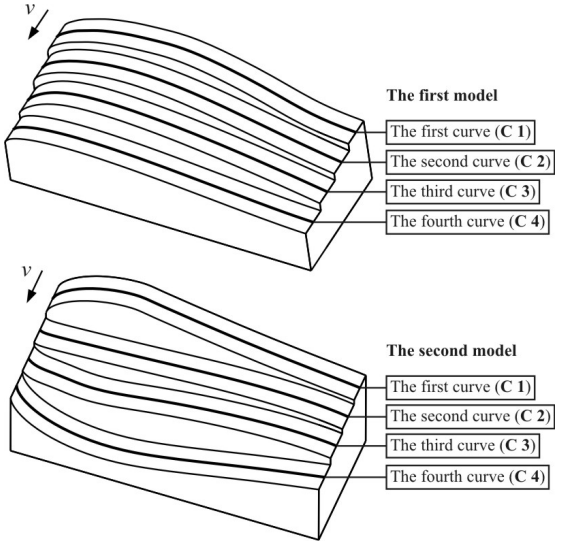

Fig. 2. *The models of workpieces used during investigations*

The measured workpieces had free-form surfaces with varying curvature. The nominal models were created with the use of the CATIA software and were imported into the measurement software in order to perform the simulation of coordinate measurements.

4 THE SIMULATION INVESTIGATIONS

The numerical investigations concerned coordinate measurements of considered objects (Fig. 2) on a coordinate measuring machine. The 2D curve measurement element was used during simulations. That element was chosen due to the lack of curvature along directions denoted as *v* of analyzed curvilinear surfaces of measured products. There was used the uniform distribution of nominal and measured points along free-form surfaces of measured workpieces. The uniform distribution of nominal points along analyzed free-form profiles (denoted as **C 1** – **C 4**) was the result of using the 2D curve measurement element.

The used measurement element enables the equal distance between nominal points. The number of nominal points was equal 100. The distances between measured points were equal: (0.1, 0.25, 0.5, 0.75, 1) mm. During conducted simulations the measured points were generated by using of the following dispersion: (±0.01, ±0.05, ±0.1) mm around nominal profiles. The dispersion of measured points results from the inaccuracy of manufacturing processes of measured workpieces and the inaccuracy of coordinate measurements of analyzed objects. The dispersion was applied in order to guarantee the randomness of results of measurements. In the case of the inaccuracy of machining processes randomly distributed points symbolized the real shape of the measured workpiece.

The investigations were conducted for three separate methods of form deviation calculation. The first two methods were described in the section 1 in detail. Those methods are based on nominal (the first method denoted as **N** in Tables 1 and 2) and measured (the second method – **R**) points at which local deviations are calculated. Additionally, in the case of the commercial method based on nominal points outliers were removed (**NC**). The way of removing outliers resulted from the algorithm of measurement data analysis which is available in the Calypso software. The outliers were removed in order to reduce the evaluated form deviations and make them correspond, as much as it is possible, to the assumed dispersion.

The third considered method was the new one, which is based on the interpolation process of groups of five neighboring points by using of the Lagrange (**L**) and Chebyshev (**CH**) methods. In the case of the proposed algorithm of form deviation calculation outliers were removed as well. The selected results of numerical investigations for selected considered models of measured products, distances between measured points and their dispersion are presented in Tables 1 and 2. The results concern the form deviations of contour. The form deviations should be equal to twice the maximum local deviations. Therefore, the

Table 1. *The results of numerical investigations for the first model*

	Distance [mm]	C	N [mm]	NC [mm]	R [mm]	CH [mm]	L [mm]
Dispersion = ±0.01 [mm]	0.1	1	0.0211	0.0211	0.0200	0.0249	0.0247
		2	0.0225	0.0225	0.0200	0.0235	0.0286
		3	0.0234	0.0234	0.0200	0.0247	0.0314
		4	0.0236	0.0236	0.0199	0.0249	0.0249
	0.25	1	0.2947	0.0208	0.0200	0.0235	0.0235
		2	0.3559	0.0210	0.0200	0.0342	0.0278
		3	0.2409	0.0245	0.0200	0.0313	0.0312
		4	0.7923	0.0202	0.0200	0.0257	0.0257
	0.5	1	1.0667	0.2126	0.0199	0.0329	0.0329
		2	1.1698	0.3232	0.0199	0.0192	0.0192
		3	0.7241	0.2015	0.0198	0.0247	0.0247
		4	2.0499	0.0223	0.0199	0.0284	0.0284
	0.75	1	2.8797	0.0234	0.0199	0.0277	0.0277
		2	2.8222	0.0987	0.0193	0.0220	0.0220
		3	1.7194	0.0855	0.0199	0.0256	0.0257
		4	4.3864	0.8286	0.0200	0.0246	0.0246
	1	1	5.2684	1.9676	0.0200	0.0264	0.0264
		2	4.9068	0.0901	0.0200	0.0279	0.0279
		3	2.8898	1.0925	0.0199	0.0270	0.0270
		4	8.3676	0.0958	0.0195	0.0266	0.0266
Dispersion = ±0.05 [mm]	0.1	1	0.0985	0.0985	0.0999	0.1068	0.1076
		2	0.1183	0.1183	0.1000	0.1236	0.1259
		3	0.1027	0.1027	0.1000	0.1329	0.1326
		4	0.0961	0.0961	0.0999	0.1357	0.1357
	0.25	1	0.3259	0.1123	0.0996	0.1207	0.1207
		2	0.2960	0.1010	0.0998	0.1579	0.1578
		3	0.1417	0.1417	0.0988	0.1324	0.1324
		4	0.7969	0.1167	0.0996	0.1586	0.1586
	0.5	1	1.0544	0.2497	0.0999	0.1234	0.1234
		2	1.2080	0.2662	0.0999	0.1260	0.1260
		3	0.6985	0.1182	0.0997	0.1404	0.1404
		4	2.2498	0.1093	0.0992	0.1356	0.1356
	0.75	1	2.8061	0.1157	0.0990	0.1170	0.1170
		2	2.8009	0.0983	0.0996	0.1332	0.1332
		3	1.6364	0.1164	0.0989	0.1223	0.1223
		4	4.5283	0.9895	0.0987	0.1494	0.1494
	1	1	5.1625	1.7798	0.0988	0.1076	0.1076
		2	4.9732	0.1259	0.1000	0.1168	0.1168
		3	2.8029	1.0193	0.0999	0.1424	0.1424
		4	8.6740	0.1130	0.0998	0.1503	0.1503

Table 2. *The results of numerical investigations for the second model*

	Distance [mm]	C	N [mm]	NC [mm]	R [mm]	CH [mm]	L [mm]
Dispersion = ±0.01 [mm]	0.1	1	0.0226	0.0226	0.0200	0.0271	0.0297
		2	0.0228	0.0228	0.0200	0.0311	0.0326
		3	0.0217	0.0217	0.0200	0.0319	0.0316
		4	0.0222	0.0222	0.0200	0.0279	0.0314
	0.25	1	0.3532	0.0195	0.0198	0.0281	0.0281
		2	1.2584	0.0473	0.0200	0.0281	0.0282
		3	0.3015	0.0216	0.0200	0.0299	0.0298
		4	0.2324	0.0235	0.0200	0.0250	0.0250
	0.5	1	0.9350	0.0216	0.0200	0.0227	0.0227
		2	2.7444	0.0211	0.0199	0.0264	0.0264
		3	1.0067	0.2815	0.0199	0.0276	0.0275
		4	0.7279	0.2128	0.0198	0.0292	0.0292
	0.75	1	2.1434	0.1330	0.0200	0.0229	0.0229
		2	6.8376	0.0213	0.0199	0.0242	0.0246
		3	2.6960	0.2268	0.0200	0.0292	0.0292
		4	1.8546	0.0558	0.0199	0.0257	0.0257
	1	1	3.7017	0.0690	0.0198	0.0305	0.0305
		2	6.9805	0.0241	0.0198	0.0252	0.0252
		3	5.0106	0.0208	0.0198	0.0246	0.0246
		4	3.3280	1.1266	0.0198	0.0281	0.0281
Dispersion = ±0.1 [mm]	0.1	1	0.2110	0.2110	0.1999	0.2524	0.2524
		2	0.2382	0.2382	0.1998	0.2622	0.2623
		3	0.2028	0.2028	0.1999	0.2653	0.2449
		4	0.2132	0.2132	0.1998	0.2968	0.3040
	0.25	1	0.5360	0.2122	0.1997	0.2650	0.2646
		2	1.1383	0.1986	0.1991	0.3100	0.3100
		3	0.2262	0.2262	0.1988	0.3212	0.3212
		4	0.3476	0.2348	0.1997	0.2322	0.2322
	0.5	1	0.8834	0.2207	0.1994	0.2553	0.2553
		2	2.5056	0.2234	0.2000	0.2618	0.2618
		3	1.0715	0.1942	0.1973	0.2235	0.2235
		4	0.7557	0.2549	0.1986	0.2942	0.2942
	0.75	1	1.9975	0.2786	0.1989	0.2868	0.2868
		2	7.7736	0.2377	0.1992	0.3145	0.3145
		3	2.8244	0.3449	0.1983	0.2491	0.2491
		4	1.9309	0.2232	0.1953	0.2268	0.2268
	1	1	3.5546	0.2057	0.1959	0.2541	0.2541
		2	6.6456	0.3950	0.1991	0.2679	0.2679
		3	5.0134	0.2047	0.1999	0.2125	0.2125
		4	3.2780	0.2084	0.1999	0.2806	0.2806

form deviations should be equal respectively: (0.02, 0.1, 0.2) mm.

5 THE STATISTICAL ANALYSIS

In the case of the new method of form deviation calculation, which can be used during coordinate measurements of workpieces composed of free-form surfaces, the statistical analysis was conducted. The analysis was done in order to compare the values of computed deviations, which are estimated by using of two methods of interpolation – the Lagrange and the Chebyshev methods available in the proposed method of deviation estimation. Those interpolation methods are used in order to calculate the form deviations of free-form surfaces of measured products.

The statistical analysis was conducted for the randomly chosen values of form deviations, which were selected from all results of numerical investigations obtained for the different measured workpieces, dispersion of corrected measured points and the distances between measured points. The measured objects, dispersion and distances used during the statistical analysis of gained results are shown in Tables 3 and 4. The analysis was done for deviations calculated at all nominal points of analyzed profiles.

Table 3. *The results of statistical analysis for the first model*

	Curve	Dispersion [mm]	Distance [mm]	P-Value [%]
The test of homogeneity of mean	1	±0.01	0.1	22.4
	4	±0.05	1	98.9
The test of homogeneity of variance	1	±0.01	0.1	22.5
	4	±0.05	1	78.6

Table 4. *The results of statistical analysis for the second model*

	Curve	Dispersion [mm]	Distance [mm]	P-Value [%]
The test of homogeneity of mean	3	±0.01	0.25	95.7
	3	±0.1	0.1	97.9
The test of homogeneity of variance	3	±0.01	0.25	97.0
	3	±0.1	0.1	90.3

In the first stage of analysis the comparison tests of arithmetical means of deviations calculated with the use of the Lagrange and Chebyshev methods were conducted. The null hypothesis in that stage of analysis concerned the equality of arithmetical means of deviations estimated using two above mentioned interpolation methods. The analysis of variance (known as ANOVA) was used. The level of significance was set at 5 %. The critical values p obtained on the basis of statistical analysis are presented in Tables 3 and 4. All critical values are greater than the assumed level of significance. It means that there is no basis to reject the null hypothesis of equality of arithmetical means of deviations calculated by using of two considered algorithms of interpolation. Therefore, the results gained by using of considered interpolation methods do not differ significantly from each other.

In the next stage of statistical analysis the tests of homogeneity of variance were conducted. The Levene's test was used. The used test can be implemented when there is no certainty about the normal distribution of measured deviations at all nominal points. The null hypothesis concerned the equality of variances, which were calculated when using two interpolation algorithms based on the Lagrange and Chebyshev methods. The level of significance was equal 5 %, similarly to the first stage of analysis. The statistical tests gave the critical values greater than the used level of significance as well. The results of calculations are presented in Tables 3 and 4. Therefore, there is no basis to reject the null hypothesis of equality of variances, which were calculated by using of considered interpolation methods available in the proposed method of form deviation calculation.

6 THE EXPERIMENTAL INVESTIGATIONS

The experimental investigations concerned real contact coordinate measurements of the profile **C 1** in the case of the first product (Fig. 2) by using of the coordinate measuring machine ACCURA II equipped with the measuring probe VAST XT (Fig. 3) and the Calypso inspection software. The selected accuracy parameters of the applied measuring system are the following:

- $E_{L,MPE} = 1.6 + L/333$ μm,
- $P_{FTU,MPE} = 1.7$ μm,
- $MPE_{Tij} = 2.5$ μm,
- $MPT_{tij} = 50$ s.

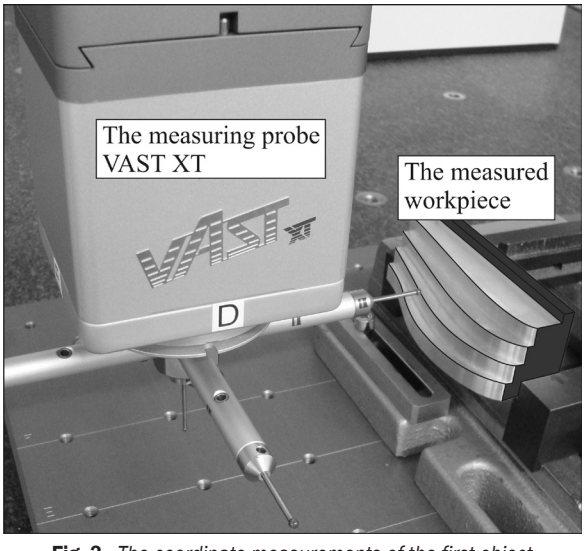

Fig. 3. *The coordinate measurements of the first object*

The measured product was made of aluminum alloy and machined by using of the DMU 100 monoBLOCK CNC machine tool. Similar to the simulation studies there was used the uniform distribution of nominal and measured points. The measurements were performed with the use of different

scanning velocities, denoted as v_s and distances between measured points, denoted as d. There were used the following measurement parameters:

- v_s = 10 mm/s, 20 mm/s, 30 mm/s,
- d = (0.5, 1, 1.5, 2, 2.5, 3) mm.

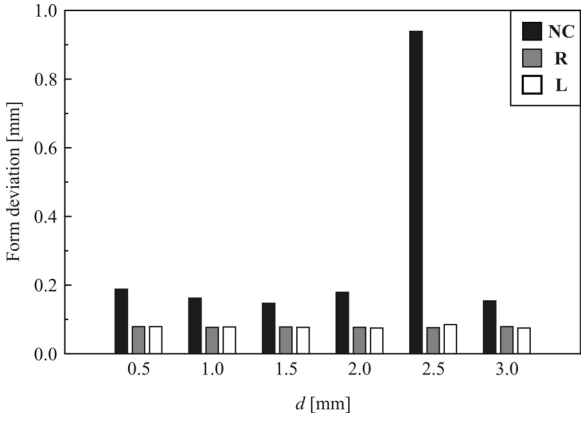

Fig. 4. *The results of experimental research for v_s = 10 mm/s*

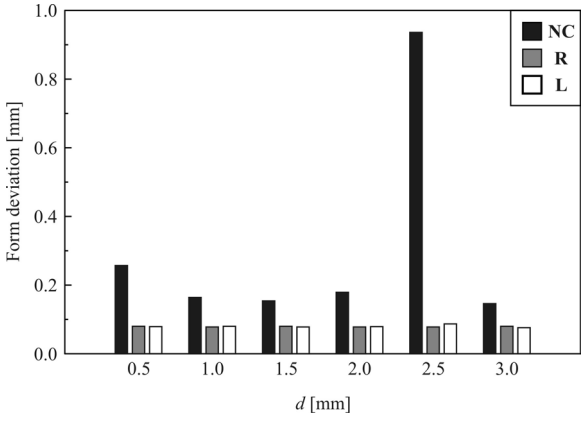

Fig. 5. *The results of experimental research for v_s = 20 mm/s*

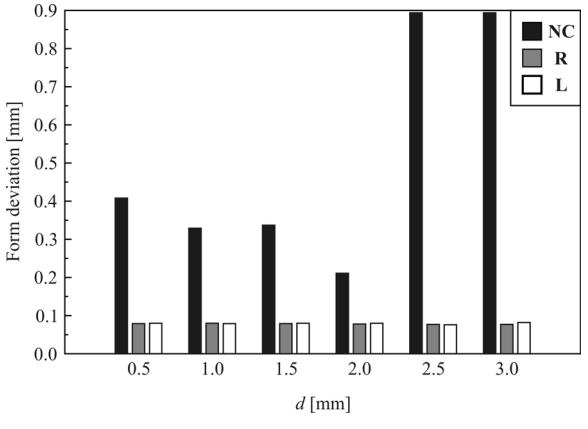

Fig. 6. The results of experimental research for v_s = 30 mm/s

Moreover, the coordinate measurements were conducted by using of the same algorithms of form deviation calculation like those used during the simulation investigations. They were based on nominal points (**NC**), measured points (**R**) and the Lagrange interpolation method (**L**). The method **L** was applied during the experimental research because, based on the results of statistical analysis, there are no significant differences between two analyzed interpolation algorithms. The results of performed experimental research are presented in Figs. 4 to 6.

7 DISCUSSION

The new method of form deviation calculation was verified during the simulation and experimental investigations. It should be expected that the calculated form deviations of analyzed free-form surfaces of products in numerical investigations should correspond to the assumed dispersion of measured points. However, the experiments showed that the values of a form deviation similar to the values of a range were gained only in the case of the second method of form deviation calculation, which is based on measured points. In the case of other considered methods, which use nominal points to calculate form deviations of curvilinear surfaces, values of a form deviation exceed values of a range of generated measured points.

The results of conducted numerical research indicate that there is no influence of the distance between measured points on the values of a form deviation in the case of the proposed method of form deviation calculation. That is the advantage of the new algorithm. When using the first method of form deviation calculation, available in the commercial software of e.g. coordinate measuring machines, the calculated form deviations increase with decreasing the number of measured points. In the case of the first method removing outliers causes lower values of a form deviation but not correspond to the dispersion in all analyzed cases.

The conducted statistical analysis of selected results of simulation investigations shows that there are no significant differences between two interpolation methods available in the proposed method of form deviation calculation when comparing the gained values of a deviation.

The experimental investigations confirm the results of numerical research. The form deviations calculated by using of the proposed method are lower than the values of a deviation calculated with the use of the method **NC** available in the commercial inspection software. The deviations calculated using the algorithm based on the Lagrange interpolation

method are close to the values of a deviation gained by using of the method **R**. Based on the results of numerical research, the method **R** can be considered as the reference one. Moreover, the deviations calculated by using of the method **NC** are dependent largely on the applied scanning velocities and distances between measured points.

8 CONCLUSIONS

In the article the new method of form deviation calculation was presented. The proposed algorithm is based on the interpolation process of corrected measured points with the use of the Lagrange and Chebyshev methods. The proposed method of form deviation calculation achieved better results of investigations than the method based on nominal points in the Calypso software.

The advantage of the proposed method is the possibility of choosing the appropriate algorithm of interpolation of measured points. In the case of the considered measurement software a user cannot select other methods of interpolation of corrected measured points besides the default available algorithm.

The additional advantage of the developed algorithm is that it can be implemented in most measurement software. In the case of the Calypso software the implementation can be realized by using of the PCM module. The user is able to apply the external user-defined procedure and execute user programs under its control. Such approach gives the user enhanced possibilities to analyze the results of coordinate measurements.

9 REFERENCES

[1] Mansour, G. (2014). A developed algorithm for simulation of blades to reduce the measurement points and time on coordinate measuring machine (CMM). *Measurement*, vol. 54, p. 51-57, **DOI:10.1016/j.measurement.2014.03.046**.

[2] Poniatowska, M. (2012). Deviation model based method of planning accuracy inspection of free-form surfaces using CMMs. *Measurement*, vol. 45, no. 5, p. 927-937, **DOI:10.1016/j.measurement.2012.01.051**.

[3] Uhlmann, E., Abackerli, A.J., Schützer, K., Lepikson, H.A., Helleno, A.L., Papa, M.C.O., del Conte, E.G., Mewis, J. (2014). Simulation and analysis of error impact on freeform surface milling. *The International Journal of Advanced Manufacturing Technology*, vol. 70, no. 1, p. 607-620, **DOI:10.1007/s00170-013-5280-7**.

[4] Cheung, C.F., Kong, L.B., Ren, M.J., Whitehouse, D., To, S. (2012). Generalized form characterization of ultra-precision freeform surfaces. *CIRP Annals - Manufacturing Technology*, vol. 61, no. 1, p. 527-530, **DOI:10.1016/j.cirp.2012.03.015**.

[5] Savio, E., De Chiffre, L., Schmitt, R. (2007). Metrology of freeform shaped parts. CIRP Annals - Manufacturing Technology, vol. 56, no. 2, p. 810-835, **DOI:10.1016/j.cirp.2007.10.008**.

[6] Fang, F. Z., Zhang, X. D., Weckenmann, A., Zhang, G. X., Evans, C. (2013). Manufacturing and measurement of freeform optics. *CIRP Annals - Manufacturing Technology*, vol. 62, no. 2, p. 823-846, **DOI:10.1016/j.cirp.2013.05.003**.

[7] Savio, E., Hansen, H.N., De Chiffre, L. (2002). Approaches to the calibration of freeform artefacts on coordinate measuring machines. *CIRP Annals - Manufacturing Technology*, vol. 51, no. 1, p. 433-436, **DOI:10.1016/S0007-8506(07)61554-6**.

[8] Mehrad, V., Xue, D., Gu, P. (2013). Prediction of surface reconstruction uncertainties for freeform surface inspection. *Measurement*, vol. 46, no. 8, p. 2682-2694, **DOI:10.1016/j.measurement.2013.04.025**.

[9] EN ISO 15530:2011. *Geometrical product specifications (GPS) - Coordinate measuring machines (CMM): Technique for determining the uncertainty of measurement - Part 3: Use of calibrated workpieces or measurement standards*. International Organization for Standardization, Geneva.

[10] Liang, S.R., Lin, A.C. (2002). Probe-radius compensation for 3D data points in reverse engineering. *Computers in Industry*, vol. 48, no. 3, p. 241-251, **DOI:10.1016/S0166-3615(02)00038-6**.

[11] Vosniakos, G.C., Giannakakis, T. (2003). Reverse engineering of simple surfaces of unknown shape with touch probes: scanning and compensation issues. *Proceedings of the Institution of Mechanical Engineers, Part B: Journal of Engineering Manufacture*, vol. 217, no. 4, p. 563-568, **DOI:10.1243/095440503321628233**.

[12] Wozniak, A., Balazinski, M., Mayer, R. (2007). Application of fuzzy knowledge base for corrected measured point determination in coordinate metrology. *Annual Meeting of the North American Fuzzy Information Processing Society*, p. 135-139, **DOI:10.1109/NAFIPS.2007.383825**.

[13] Woźniak, A., Mayer J.R.R., Bałaziński, M. (2009). Stylus tip envelop method: corrected measured point determination in high definition coordinate metrology. *The International Journal of Advanced Manufacturing Technology*, vol. 42, no. 5, p. 505-514, **DOI:10.1007/s00170-008-1615-1**.

[14] *Calypso. Carl Zeiss, software documentation*. (2010), Carl Zeiss Industrielle Messtechnik, Oberkochen.

Strojniški vestnik - Journal of Mechanical Engineering 62(2016)1, 60-75

DOI:10.5545/sv-jme.2015.2905 Review Scientific Paper
Received for review: 2015-07-23
Received revised form: 2015-11-10
Accepted for publication: 2015-12-10

A Review of the Extrapolation Method in Load Spectrum Compiling

Jixin Wang* – Hongbin Chen – Yan Li – Yuqian Wu – Yingshuang Zhang
Jilin University, School of Mechanical Science and Engineering, China

Load spectrum is the basis of fatigue analysis and life prediction in engineering, and load extrapolation is an essential procedure in determining a long-term load spectrum from a short-term one. Selecting a proper extrapolation method is of great significance when considering various forms and characteristics of load. Over the past few decades, several load extrapolation methods have been proposed, therefore the reasonability and accuracy of a load spectrum extrapolated using different methods should be of great concern. This paper conducts a literature review of commonly used extrapolation methods and proposes some future areas of research. The critical factors, the advantages and disadvantages, and the application ranges of extrapolation methods are summarized using literature and illustrations to provide guidance when selecting a method. In the future, more methods and applications of extrapolation methods will be able to be explored with the further development of statistics and computer software technology.
Keywords: short-term load spectrum, long-term load spectrum, load extrapolation, parametric extrapolation, nonparametric extrapolation, quantile extrapolation

Highlights
- *This paper is focused on reviewing the commonly used extrapolation methods in load spectrum compiling in engineering;*
- *The extrapolation methods are classified as the parametric extrapolation method, the nonparametric extrapolation method and the quantile extrapolation method;*
- *Characteristics of each extrapolation method are summarized using literature and illustrations;*
- *The guidance when selecting an extrapolation method and some research prospects in this field are proposed.*

0 INTRODUCTION

In engineering, many mechanical structures and components are subjected to complex and random loads, which determine the fatigue reliability and life of the machinery [1] and [2]. Thus, it is indispensable to conduct fatigue analysis and life prediction of the structures and components based on a load spectrum [3] and [4]. Currently, a load spectrum is widely used in the fields of aerospace [5] and [6], vehicle [7] and [8], wind power [9] and [10], construction machinery [11] and [12], and so on [13] and [14]. In practice, a long-term load spectrum contains the complete load information, but it is difficult to be directly measured due to the restrictions of testing technology, as well as time and cost. Therefore, it is necessary to obtain a long-term load spectrum based on a short-term one.

The traditional load spectrum compiling method multiplies a short-term load spectrum with a constant proportionality coefficient [15] to [17]. Since only the data measured in a finite time is repeated, the extreme loads that cannot be measured and have a greater impact on damage are ignored. Load extrapolation methods can overcome the above limitation of the traditional method. With the development of statistics and computer software, new methods have been applied to load extrapolation. In load spectrum compiling, results may vary from each other with different extrapolation methods. Therefore, selecting an appropriate load extrapolation method is very important, but that is difficult in practice. For a better understanding of the methods and to provide selection guidance, several commonly used extrapolation methods are reviewed and summarized based on the literature and illustrations in this paper.

The extrapolation methods are classified as the parametric extrapolation method (PE), nonparametric extrapolation method (NPE) and quantile extrapolation method (QE). In PE, sample data is supposed to obey a known distribution, and the parameters in the function are estimated according to the load sample. In NPE, an extrapolated result is obtained because the density distribution with an arbitrary shape can be received based on a nonparametric density estimation. When the sample data has different load characteristics due to different working conditions and different operating behaviors in the testing process, QE can break the data into a series of clusters and computes the damage of each rainflow matrix. The literature and illustrations are presented to evaluate the extrapolation methods and the characteristics of various extrapolation methods, such as the critical factors, the advantages and disadvantages, and the application ranges, are summarized. Some potential research prospects are

*Corr. Author's Address:School of Mechanical Science and Engineering, Jilin University, Changchun, China, 1518051537@qq.com

also discussed. The aim of this review is to be all encompassing, but this is an impossible task, so we apologize for any omissions.

1 EXTRAPOLATION METHODS

1.1 Parametric Extrapolation Method (PE)

Fitting sample data with a distribution function and estimating the parameters are included in PE. Due to the different types of sample data, PE is divided into the parameter-estimate extrapolation method (PEE) and the extreme-value extrapolation method (EVE).

1.1.1 Parameter-Estimate Extrapolation Method (PEE)

PEE is a traditional extrapolation method and extrapolates a short-term load spectrum counted from a measured load time history. PEE includes one-dimension extrapolation, in which only amplitudes accompanied by the frequencies are extrapolated, and the two-dimensional extrapolation extrapolates both the means and amplitudes together with the frequencies **[18]** to **[20]**. In practice, the two-dimensional extrapolation method is commonly used and the process is reviewed as follows:

1. Preprocess the measured load

   The preprocessing mainly includes discretizing the analog signal, filtering the digital signal, eliminating the trend item, checking and eliminating the abnormal peaks **[21]**.

2. Transform the load time history into a short- term load spectrum.

   The rainflow counting method (RCM) is frequently used in PEE **[16]** and **[18]**. RCM, which was proposed by Matsuiski and Endo more than 50 years ago and developed in the following decades **[22]** and **[23]**, is a procedure for determining the damaging load cycles in a load time history **[24]**, and the cycles are usually summed into bins referenced by their mean values and amplitudes. For examples, in Wang et al. **[25]**, the outfield load spectrum was divided into one main cycle and four sub cycles by RCM.

3. Fit the amplitudes and mean values with distribution functions.

   The relationship between the mean values and frequencies usually obeys a normal distribution **[20]**. Meanwhile, the relationship between the amplitudes and frequencies usually obeys a Weibull distribution **[26]**.

   When the assumed variables obey a two-dimensional normal distribution, a probability density function is introduced by Holling and Mueller **[27]**:

$$f(x,y)=\frac{1}{2\pi\sigma_1\sigma_2\sqrt{1-\rho^2}}\times e^{\frac{-1}{2(1-\rho^2)}\left(\frac{(x-\mu_1)^2}{\sigma_1^2}-2\rho\frac{(x-\mu_1)(y-\mu_2)}{\sigma_1\sigma_2}+\frac{(y-\mu_2)^2}{\sigma_2^2}\right)}, \quad (1)$$

where μ_1, μ_2 are the mathematical expectations of x and y, respectively, σ_1, σ_2 are the standard deviations of x and y, respectively, and ρ is the correlation coefficient. In the equation, μ_1, μ_2, σ_1, σ_2, ρ are all constants, and $\sigma_1>0$, $\sigma_2>0$, $-1<\rho<1$.

When the assumed variables obey a three-parameter Weibull distribution, the probability density function is **[28]** and **[29]**:

$$f(x)=\frac{\alpha}{\beta-\varepsilon}\left(\frac{x-\varepsilon}{\beta-\varepsilon}\right)^{\alpha-1}\exp\left[-\left(\frac{x-\varepsilon}{\beta-\varepsilon}\right)^{\alpha}\right], \quad (2)$$

where x is the amplitude of the measured load, α is the shape parameter, β is the scale parameter, which equals to the value of the characteristic load, ε is the location parameter (minimum of the load). The parameters of Weibull distribution can be verified by the correlation coefficient optimization method introduced by Fu and Gao **[30]**, and the parameter estimation methods are mainly involved in Nagode and Fajdiga **[26]**.

4. Perform the correlation and ergodic examinations on the two functions in step 3 **[20]**.

   After these four steps, the joint probability density function is obtained. The probability 10^{-6} is usually chosen as the probability that the maximum load occurs **[31]**. The cumulative frequencies of all working conditions are calculated when the total cumulative frequency reaches 10^6. The calculation formula to expand the frequency is **[32]**:

$$N_i^{'}=kN_i, \quad (3)$$

where $N_i^{'}$ is the load cumulative frequency of the condition i after the extrapolation; N_i is the load cumulative frequency of the condition i before the extrapolation; k is the extending factor, $k=10^6/N$, N is the total load cumulative frequency before the extrapolation and can be calculated with Eq. (4) **[18]** and **[32]**:

$$N=N^{'}\int_{S_{a1}}^{S_{a2}}\int_{S_{m1}}^{S_{m2}}f(x,y)\,dx\,dy, \quad (4)$$

where S_{a1} and S_{a2} are the lower and upper limits of a load amplitude integration, respectively; S_{m1} and

S_{m2} are the lower and upper limits of a load mean integration, respectively; N' is the load frequency of all conditions after extrapolation; $f(x,y)$ is the joint probability density function of the mean and amplitudes; x is the amplitude of the load; and y is the mean of the load.

5. Compile the long-term two-dimension load spectrum [20].

The process includes the amplitude classification, the mean classification, and the calculation of all cycle numbers. For convenience of the load spectrum application, it is necessary to transform the two-dimensional load spectrum into a one-dimensional one, which only describes the relationship between the amplitudes and frequencies. Thus, to transform the fluctuation of the mean equivalent to the amplitude, the Goodman diagram [33] is applied.

Through the above main process of PEE, the practical long-term load spectrum can be obtained. Some literature takes similar extrapolation concepts into use. In Nagode and Fajdiga [34], the scatter of a loading spectrum is extrapolated and a new process is created. Punee and Lance [35], based on the limited field data, employed statistical load extrapolation methods by estimating necessary probability distributions to predict the design loads. Nagode et al. [36] introduced two appropriate parametric models and compared them with the nonparametric methods. Agarwal and Manuel [37] extensively researched the design load spectrum of an off-store wind driven generator. With limited sample data, the obvious wave heights on wind speed were fitted by a Weibull distribution and the mean wind speed were fitted by a Rayleigh distribution, then the relevant parameters were estimated and the possible wind regimes were extrapolated.

The tail-fitting of the amplitude distribution in PEE draws little attention, which may lead to uncertainty in the fatigue analysis and life prediction based on the extrapolation results. Veers and Winterstein [10] discussed the mean, spread and tail behavior of the distribution of rainflow-range load amplitudes to approximate the distribution functions. The third moment is the skewness that provides detailed information on the tail behavior of the distribution. They improved the accuracy and reliability of the results by fitting the wind speed and turbulence intensity for various conditions, and the method provided useful information on the nature of the behavior. Moriarty et al. [38] also verified that the higher-order moment, such as the skewness of the extreme distribution, seriously influences the extrapolated long-term loads.

1.1.2. Extreme-Value Extrapolation Method (EVE)

EVE is based on the extreme value theory (EVT) [39]. In EVE, the load spectrum made up of extreme values is extrapolated. Johannesson and Thomas [17] and Johannesson [40] divided EVE into two branches: the extrapolation in the time domain (EVET, based on the extraction methods of block maxima method and peak over threshold [41]) and in the rainflow domain (EVER, based on extraction method of level upcrossings [10]). So the process of EVE is divided into two steps: extract extreme values from a load time history and fit the extracted data.

First of all, the data extraction methods are reviewed:

Block maxima method (BMM): It divides the continuous data $X_1, X_2, \ldots, X_n$, into groups according to the interval length l, and then extracts the high maxima $M_{l,1}, M_{l,2}, \ldots, M_{l,k}$ of each group to constitute the extreme value sample. Fig. 1, which was structured according to this principle [42], shows that the key point of this method is to determine the block size reasonably [42]. This will result in a biased estimation if the block is too narrow; on the contrary, it will lead to an increase in the variance because of the lack of extreme values. Moreover, only extreme values are used in each block, which results in a low rate of data utilization, thus a large sample size is necessary.

The research on block size determination is important and the block size is usually set as one year [43] to [45].

Peak over threshold (POT): The first step is selecting the threshold level u (including $u_{\max}$ and $u_{\min}$) under certain conditions. Then the exceedances under $u_{\min}$ and the exceedances over $u_{\max}$ are extracted from the data, and the constitution of a new sample is made up of the exceedances. The samples of the loads $X_1, X_2, \ldots, X_n$ are assumed to be independent and obey the same distribution. Fig. 2, which was structured according to this principle [38] and [46], shows that X_i will be described as the super-threshold, $Y_i = |X_i - u|$ is the exceedance, and n_u as the numbers transcending the threshold, if $X_i > u_{\max}$ or $X_i < u_{\min}$. By POT, the maxima above the threshold $u_{\max}$ and the minima below the threshold $u_{\min}$ are randomly regenerated, and only these extreme values will be extrapolated.

For the threshold, on one hand, the level must be high enough so that only true peaks, with Poisson arrival rates, are selected. Small values for the threshold will lead to a biased estimation [47]. On the

other hand, the level must be low enough to ensure that sufficient data will be selected to guarantee an accurate estimation of the distribution parameters, and the variance of the parameters will be decreased [47]. Johannesson [40] suggested a simple method that sets the threshold equal to the square root of the cycle number in the signal and works well in many cases [48].

Other threshold-selection methods have also been proposed, for example, Davison [49], Ledermann et al. [50] and Walshaw [51].

Level upcrossings (LU): According to Johannesson and Thomas [17], LU is proposed to obtain the maxima and minima of the load cycles, then determine the limiting shape of the rainflow matrix (RFM) and estimate the limiting RFM G [17]:

$$G=\left(g_{ij}\right)_{i,j=1}^{n}, \tag{5a}$$

$$g_{ij}=\lim_{z\to\infty}\frac{E[f_{ij}]}{z}, \tag{5b}$$

where the elements f_{ij} of F_z are the number of rainflow cycles in distance z, with a minimum in class i and a maximum in class j. F_z is the rainflow matrix in distance z.

This approach is based on an asymptotic theory for the crossings of extreme (high and low) levels. First, obtain a measured RFM F [17]:

$$F=\left(f_{ij}\right)_{i,j=1}^{n}, \tag{6}$$

where f_{ij} is the number of the cycle with minimum i and maximum j.

Then, calculate the LU from F and determine a suitable threshold. The level upcrossings spectrum is calculated as follows [17]:

$$N=\left(n_k\right)_{k=1}^{n}, \tag{7}$$

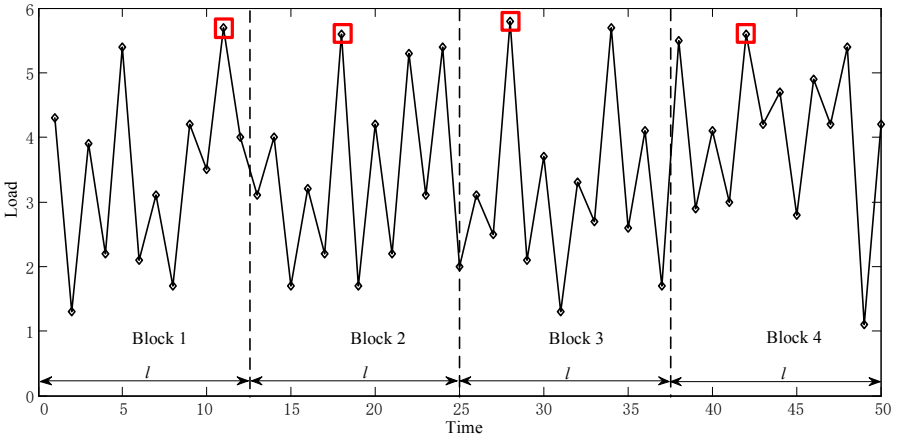

Fig. 1. *Schematic diagram of BMM*

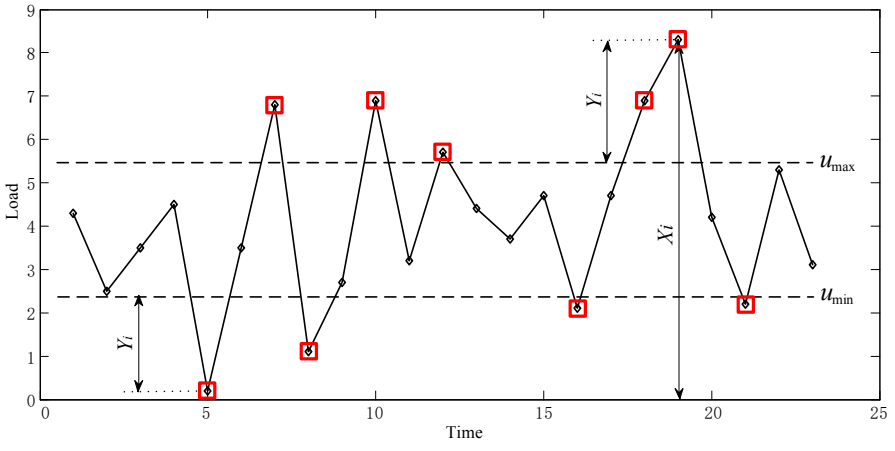

Fig. 2. *Schematic diagram of POT*

where n_k is the accumulative cycle number from the load level i below k to the load level j above k: $n_k = \sum_{i<k<j} f_{ij}$.

After reviewing the extraction methods, the fitting process will be described.

In the time domain, POT is more frequently used, and taking it as an example in this section: the load threshold is u and the load exceedances above or below u usually obey the Generalized Pareto distribution (GPD), introduced by Pickands [52], Cerrini et al. [53] and Lourenco [54]. The cumulative distribution function for GPD is [53]:

$$F(x)=1-\left[1-\frac{k}{\alpha}(x-u)\right]^{1/k}, \quad (8)$$

where u is the predetermined threshold, x is the measured load, $x-u$ is the exceedance, k is the shape parameter, and α is the scale parameter.

When $k=0$, the GPD turns into an exponential distribution [53]:

$$F(x)=1-\exp\left(-\frac{m}{\alpha}\right), \quad (9)$$

where $m=|x-u|$ is the 'mean exceedance'.

When the exceedances obey the exponential distribution, the estimated parameter is the mean of the exceedances [53]:

$$m=\frac{1}{N}\sum_{i=1}^{N} Z_i, \quad (10)$$

where Z_i is the exceedance, N is the number of exceedances.

The parameter estimations for the GPD have been discussed by Davison [49], Hosking and Wallis [55], as well as Smith [56].

In the rainflow domain, the shape of the level upcrossing intensity above the threshold is estimated. The level upcrossing obeys GPD and the estimates of the parameters in GPD are calculated using relative estimation techniques [17]. Then, an estimate of the cumulative RFM is calculated as [17]:

$$n_{ij}=\frac{n_i n_j}{n_i+n_j}, \quad (11)$$

Thus, the corresponding estimation of the RFM F^{rfc} is [17]:

$$F^{rfc}=\left(f_{ij}\right)_{i,j=1}^{n}, \quad (12)$$

where f_{ij} is the cumulative frequency number from the load level i to the load level j, $f_{ij}=n_{i+1,j-1}-n_{i,j-1}-n_{i+1,j}+n_{i,j}$.

The main process of EVE has been sketched out and the practical operation is conducted based on the technical software package, for example, WAFO [57]. Johannesson [40] conducted the 100-fold extrapolation and compared the extrapolated load spectrum with the 100 repetitions of the measured load spectrum, then it was found that the extrapolation result was more reasonable because it agreed well with the observed load spectrum. Due to the uncertainty of wind conditions, the extreme load on a wind turbine is usually difficult to determine. In 2008, Collani et al. [58] put forward a reliable method named LEXPOL [59] to solve the problem. For the sake of different environments, Agarwal and Manuel [60] deduced the long-term loads with POT and a three-parameter Weibull distribution, then a good extrapolated result was obtained. A quadratic distortion of the Gumbel distribution was introduced by Natarajan et al. [61] and Natarajan and Holley [62] and it was used to fit the tail of the extreme loads on a wind turbine. Based on this method, the finite sample data was extrapolated to 50 years. In addition, an extrapolation method based on the mean and standard deviation of extreme values was proposed by Moriarty [63], where subjectivity of the parametric extrapolation was avoided.

1.2 Nonparametric Extrapolation Method (NPE)

NPE, which was proposed by Dressler et al. in 1996 [64], uses a nonparametric statistical approach to get the statistical probability distribution. In NPE, the nonparametric density estimation reduces the subjectivity of empirical hypothesis because it makes no assumptions on the distribution of the sample data. As a result, the extrapolated load spectrum is not influenced by the characteristics of the sample data.

The kernel estimation can be employed for nonparametric density estimation [65] and [66]. The estimation transforms a discrete histogram of sample data into a probability distribution.

Suppose $X_1, X_2, ..., X_n$ are observed samples from a common distribution with density $f(\cdot)$. The kernel density estimation (KDE) of $f(\cdot)$ is [64]:

$$\hat{f}_h(x)=\frac{1}{nh}\sum_{i=1}^{n} K\left(\frac{x-X_i}{h}\right), \quad (13)$$

where K is the kernel function and h is the bandwidth.

To assure the reasonability of the KDE function $\hat{f}_h(x)$, kernel K satisfies [64]:

$$K(x)\geq 0, \quad \int_{-\infty}^{+\infty} K(x)dx=1, \quad (14)$$

The main process of NPE is as follows [66]:

1. Transform the measured load time history into a rainflow counted histogram.
2. Select the appropriate kernel function and bandwidth, then use the nonparametric method in combination with the Monte Carlo method [67] to extrapolate the RFM that is obtained from the lifecycle one.
3. Reconstruct a new load spectrum from the RFM lifecycle.

For NPE, a lot of research was conducted on the selection of the kernel function and bandwidth. Wang et al. [68] proposed a selection method for the kernel function and the multi-criteria decision making technique was successfully used to solve the problem of the kernel function selection. For the bandwidth selection, Heidenreich et al. [69] reviewed the bandwidth selections for the kernel density estimation and some of the methods can be used in NPE. Sheather [70] proposed two kinds of bandwidth determination methods: Sheather-Jones plug-in bandwidth and least squares cross validation. The Sheather-Jones plug-in bandwidth was widely used because of its overall good performance, but this method was prone to be over-smoothing in some situations. As a supplement, it was solved by the least squares cross validation. Besides, Bayesian methods [71] and [72] were used to estimate the adaptive bandwidth and adaptive bandwidth matrix in univariate and multivariate KDEs.

For the applications of NPE, Dressler et al. [64] transformed the discrete rainflow matrix into a smooth function that is more accessible with a kernel density estimator. In the literature, the RFM is seen as two-dimensional histograms of the opening and closing points of hystereses, and can only be described by a nonparametric method due to its arbitrary shapes. Socie [73] employed nonparametric kernel smoothing techniques to transform the discrete rainflow histogram of cycles into a probability density histogram and extrapolated the short-term measured load to an expectedly long-term one. The key role of the bandwidth in KDE is also indicated in the literature. Johannesson [17] considered that kernel smoothing is a feasible smoothing technique and well-established statistical method for nonparametric estimation. A kernel smoother method is also proposed to estimate the RFM for the cycles with small and moderate amplitudes. Mattetti et al. [74] extrapolated the RFM by NPE in carrying out of accelerated structural tests of tractors.

1.3 Quantile Extrapolation Method (QE)

Considering the influences of different working conditions and operating behaviours in engineering, load extrapolation is difficult. Under these circumstances, the quantile extrapolation method (QE) is capable of taking various conditions and behaviors into consideration and optimizing the extrapolation results.

The main process of QE is as follows [64]:

1. Break the data set of the rainflow-counted histogram into a series of clusters $B_1, B_2, ..., B_m$ with similar variables and damages.
2. Compute the damage of each original RFM R by Miner's rule. Damage vectors [64]:

$$(D_1(R_1), ..., D_m(R_1))$$
$$\vdots$$
$$(D_1(R_n), ..., D_m(R_n))$$

are obtained for all original RFMs, where $R_1, R_2, ..., R_n$ represent the influence of various conditions and behaviors.

3. Estimate the expected damage for the x% quantile. The quantile damage vector $(q_1, q_2, ..., q_m)$, which describes the damage distribution between the individual clusters of the rainflow matrix, is used to construct the rainflow matrix. The original rainflow matrix is superposed such that [64]:

$$R_G = R_1 + \cdots + R_n. \tag{15}$$

4. Construct and extrapolate the corresponding RFM into a matrix, the extrapolation of the resulting matrix [64] is:

$$R_E = extrapol(R_G), \tag{16}$$

where R_E represents the extrapolated result and is made up of the basic process and peak values.

Socie and Pompetzki [66] described a method for statistically extrapolating a single measured service load time history to an expected long-term load spectrum. Because of the difference between operating behaviors, the extrapolation method was extended to combine data from several users. The extrapolated load spectrum would represent more severe users in the population and the optimization effect was obvious. Mattetti et al. [74] introduced a method for an accelerated test on tractors and employed QE to calculate rainflow matrices for 20 tasks repeated in five different working forms. In the selected sample, the 95th percentile of the most damaging conditions are considered.

In load spectrum compiling, QE is usually combined with other extrapolation methods and it is also an important component in computer software.

1.4 Classification of the Extrapolation Methods

The extrapolation methods are integrated into one figure for clarity. As shown in Fig. 3, the classifications and pivotal elements of the methods are reflected.

2 CASE ANALYSIS

In this section, some illustrations and examples are displayed to evaluate and demonstrate the extrapolation methods.

2.1 Case Analysis of PEE

In PEE, distributions of the sample data affect the extrapolation results [26]. In this section, the load on an axle shaft of a loader powertrain was taken as the research object. According to the obvious segment working characteristics of a loader, the operation process was divided into six sections. In this paper, the load on the axle shaft in the spading and the no load backward sections were illustrated to verify the characteristics of PEE. Amplitudes of the load with different characteristics and distributions were focused on. The Weibull distribution was employed, with the fitting results shown in Fig. 4 and Fig. 5. Compared with Fig. 4a, the fitting in middle of Fig. 5a diverges from the distribution function more remarkably. In Fig. 5b, the tail of the fitting seriously diverges from the skew line, as in Fig. 5c. Based on the comparison, the conclusion is that the fitting between the function and load in the spading section is better. So, when PEE is applied to extrapolating the load on an axle shaft with different characteristics, the repeatability of the result will be influenced. Therefore, the distributions of the sample data will influence the fitting error in PEE, and the fitting error will lead to an inaccuracy in the extrapolation results.

2.2 Case Analysis of EVE

In EVE, both the data extracting and fitting function selection will affect the extrapolation results. During the data extracting process, selection of the threshold or block size is important [75] to [78], as this will influence the data utilization ratio and the distribution characteristics of the extreme values. Fitting precisions vary from each other due to different load characteristics, thus the extrapolation results of EVE are dependent on the fitting precisions. Several examples will illustrate the influences of different thresholds on the fitting precisions.

In this section, the load on an axle shaft of a loader powertrain in the spading section was used. The automatic threshold selection method, which was proposed in Thompson [79], was adopted to determine the original threshold. In data processing, based on the sample data, 2897.3 Nm was set as the automatic threshold and the number of extreme values was 5734, thus 5734 exceedances were calculated. With GPD, the exceedances were fitted with the parameters estimated by the maximum likelihood method, and the results are shown in Fig. 6.

In order to reflect the effects of thresholds on fitting precisions, 2000 Nm and 3500 Nm were selected as the other thresholds to extract values, thus

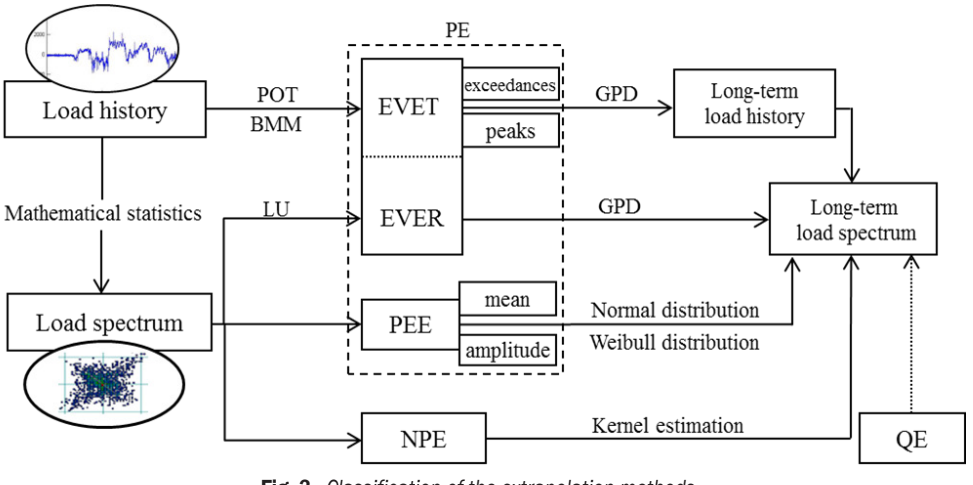

Fig. 3. *Classification of the extrapolation methods*

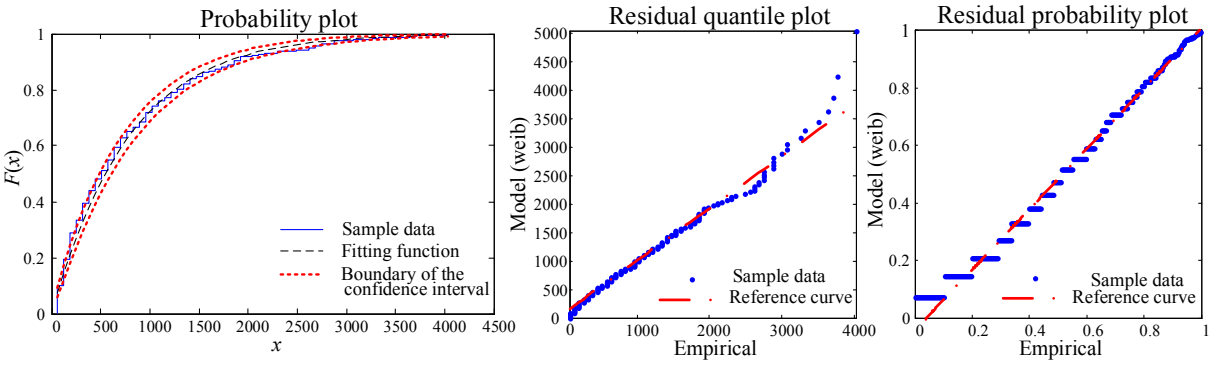

Fig. 4. *Fitting results between the distribution and load the in spading section*

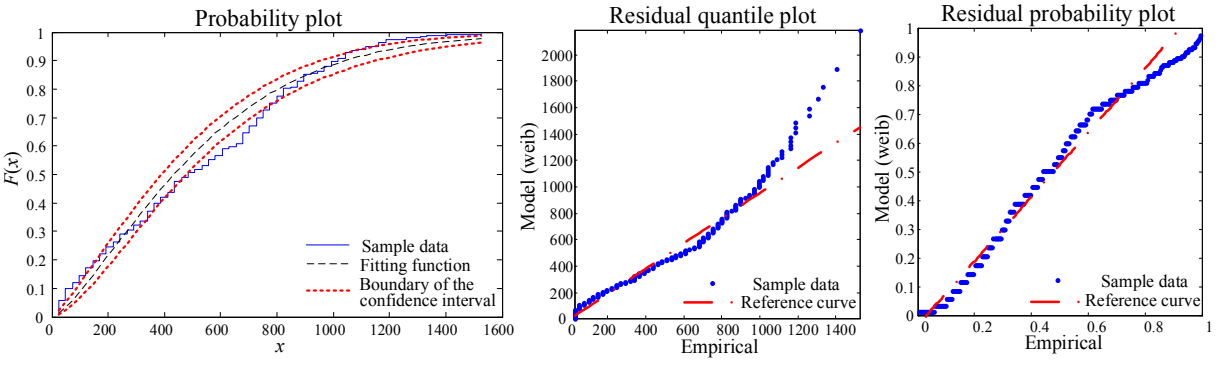

Fig. 5. *Fitting results between the distribution and load in the no load backward section*

the values were fitted with the same distribution and parameter estimation method. The fitting results are shown in Fig. 7 and Fig. 8. Compared with Fig. 6, the deviations between the data points (the extreme values) and the fitting distribution in Fig. 7 and Fig. 8 are obvious, especially in plot a and b of the figures. So, with different thresholds, the fitting precisions are different, which will influence the results from EVE. On the basis of the comparison, the significance of selecting the threshold or block size is verified.

The influence of the distribution function on the extrapolation results also needs to be considered. In Johannesson [17], GPD was used to extrapolate the simulated Markov load with the maximum likelihood estimation and the result was shown in Fig. 9a [17]. Thus, the exponential distribution was adopted to extrapolate the same load, the result was shown in Fig. 9b [17]. Making a comparison between the two parts in Fig. 9, the exponential tail in Fig 9b yields a straight line in the log-scale that tends to overestimate the intensity for extreme crossings [17]. Therefore, the conclusion can be drawn that GPD gives a better extrapolation and thus verifies the importance of selecting a suitable distribution function.

There are two branches in EVE: EVET and EVER. Making a comparison of the two branches, it is easy to find some distinctions, such as the application domains, the fitting functions and the types of the extrapolation results.

In Johannesson [40], EVET and EVER were both applied to extrapolate the load of a train and a car, respectively, and the results are show in Fig. 10.

Fig. 10 allows some comparisons between EVET and EVER to be noted [40]:

1. EVET generates the extrapolated load cycle directly based on the measured load time history, so the outcome is more reliable;
2. EVET is more robust because it is only on the basis of EVT, while the EVER uses an additional extreme value approximation for the shape of the rainflow matrix;
3. The limitation in the extrapolation multiple of EVET is that the extrapolated result is an N-fold extrapolated load. In EVER, the extrapolated result is a limited rainflow matrix, which represents infinite repetitions.
4. Results extrapolated by EVET are usually adopted into a fatigue test or as the input load

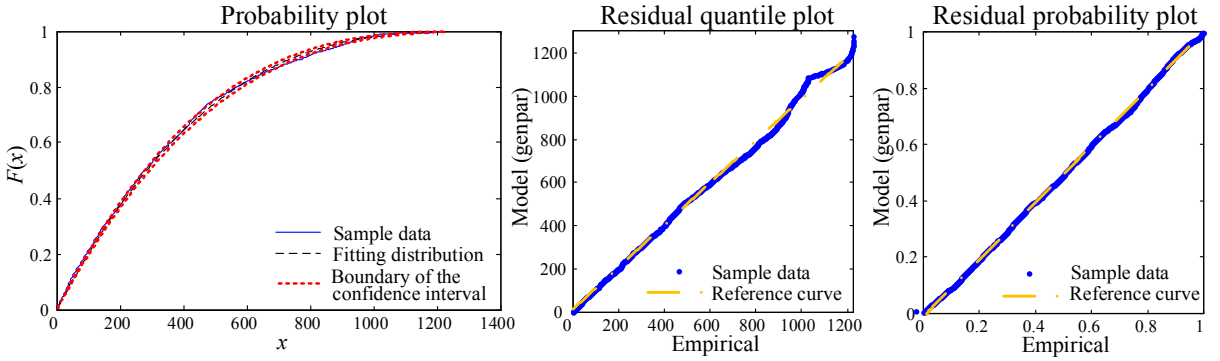

a) b) c)

Fig. 6. *Threshold u = 2897.3, fitting results*

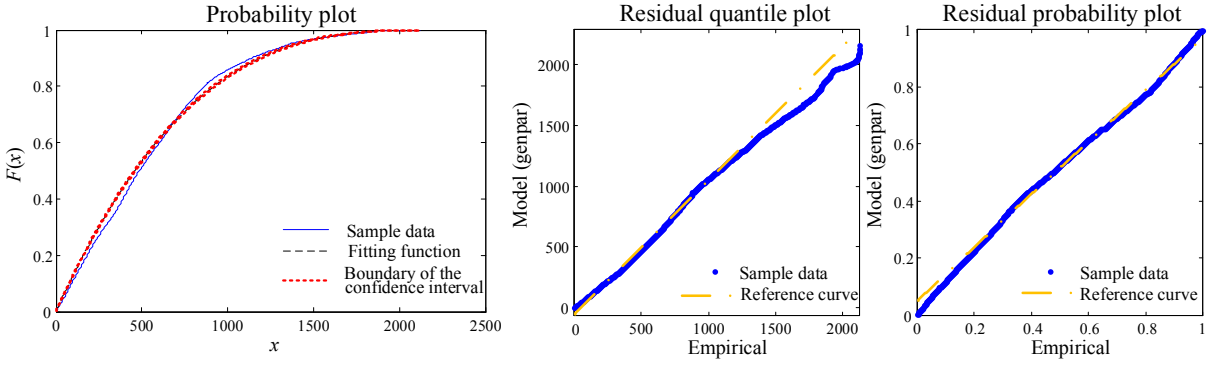

a) b) c)

Fig. 7. *Threshold u = 2000, fitting results*

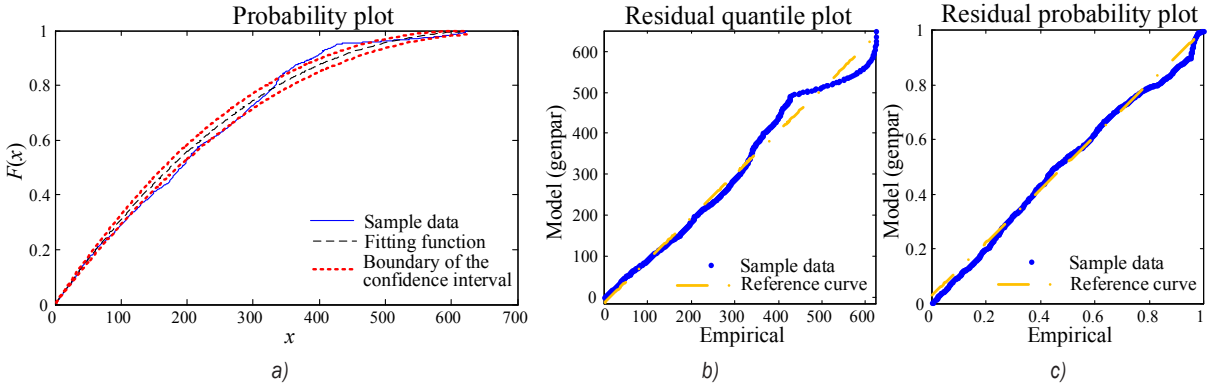

a) b) c)

Fig. 8. *Threshold u = 3500, fitting results*

for life prediction. However, if the target is to extrapolate a load spectrum and acquire the relationship between the load and frequencies over the whole life, EVER will be an appropriate selection because it has high efficiency and it can estimate the shape of the load spectrum for an infinitely long measurement. Sometimes, the extrapolation results can be transformed. Load in the time domain can be transformed into rainflow domain by RCM. The Markov method **[80]** can also be used to transform the load from the rainflow domain to the time domain. However, the accuracy of the results will be influenced during the transforming process.

2.3 Case Analysis of NPE

In NPE, kernel estimation provides a convenient way to estimate the probability density [65] and [81]. In kernel estimation, both kernel function [68] and bandwidth [66] are of great concern.

In Wang et al. [68], the selection of the kernel function was considered. Four kinds of kernel functions were illustrated; the extrapolation results are shown in Fig. 11 using these kernel functions. [68]. As shown in Fig. 11, the results based on different kernel functions vary from each other, especially the extrapolated extreme loads.

When NPE was first proposed by Dressler et al. in 1996 [64], the importance of bandwidth was emphasized and this was also confirmed in the following research [64], [66] and [82]. Compared with the kernel function, extrapolation results are more sensitive to the bandwidth [64] and [66]. So far, only two kinds of bandwidths are commonly applied to data extrapolation. They are the fixed and the adaptive bandwidth [64] and [66]. In this section, in order to verify the influence of the bandwidths on the probability density, a fixed bandwidth with different values will be discussed. As shown in Fig. 12, the solid line represents the probability density based on the automatic fixed bandwidth hs=0.5187, where the other two lines represent the densities with the bandwidths hs=0.2 and hs=1 respectively. As shown in Fig. 12, when the bandwidth equals 0.2, the double-peak occurred at the peak of the density and the fluctuation in the second half was obvious. When the bandwidth increases to 1, the maximum density declined to a large extent. So, with different bandwidths, the probability density, which is directly related to the extrapolation result, makes a big difference.

2.4 Case Analysis of QE

Based on the former discussion on QE, the principle in Dressler et al. [64] is important and comprehensive. In Dressler et al. [64], based on four figures (Figs. 10 to 13 in K. Dressler et al. [64]), the importance and

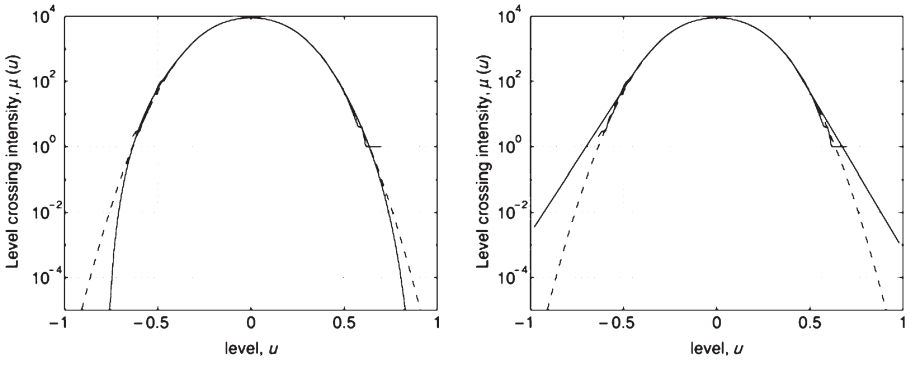

a) b)

Fig. 9. *Extrapolation of level upcrossing intensity; a) with GPD; b) with EXP* [17]

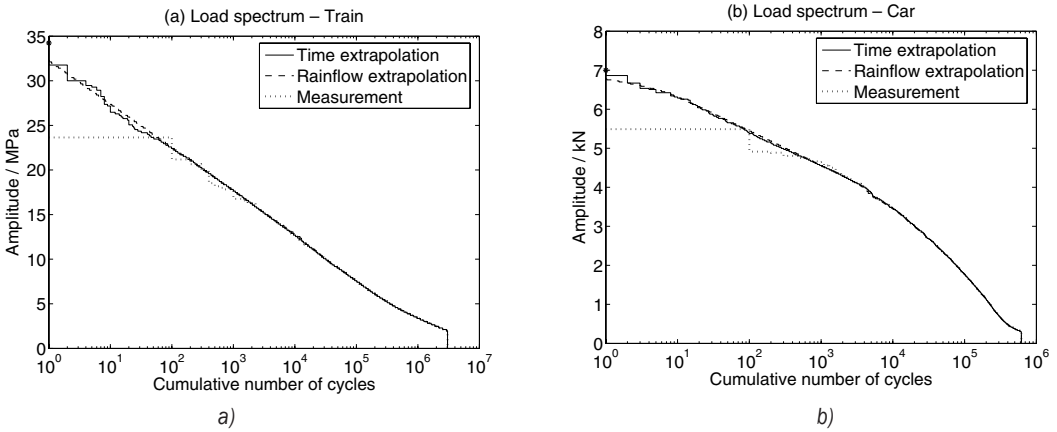

a) b)

Fig. 10. *100 times extrapolation, comparing time and rainflow domain methods* [40]

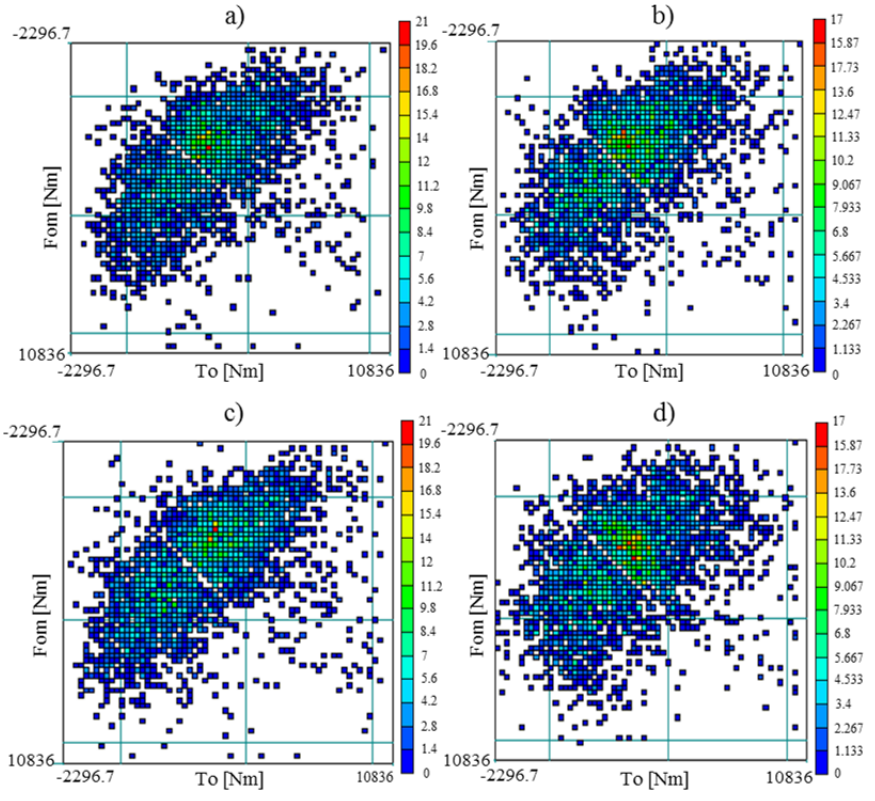

Fig. 11. *Comparison among extrapolated results based on different kernel functions; a) circular; b) mean-basedellipse; c) range-based ellipse; d) epanechekov*

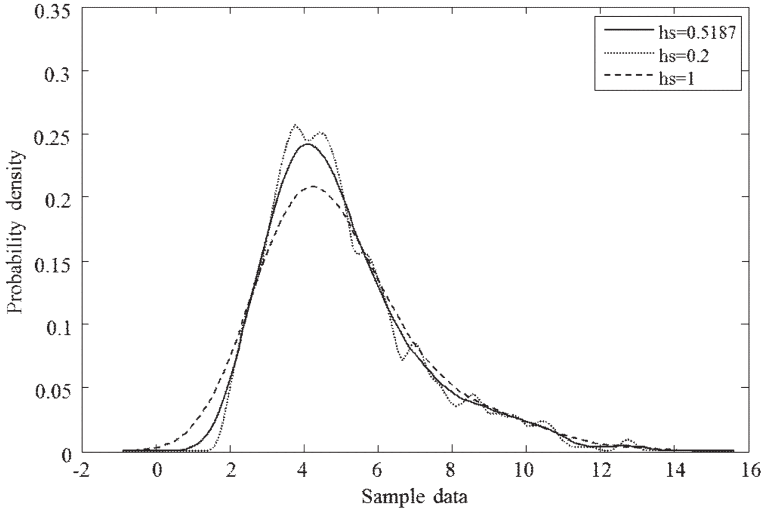

Fig. 12. *Probability density distribution with different bandwidths*

necessity of QE were confirmed, and determinations of the clusters were shown.

The choice of the solution parameters in QE was also emphasized in Dressler et al. [64]. On one hand, the extrapolation results are highly dependent on the determination of the clusters $B_1, B_2, ..., B_m$, which can be adjusted according to different conditions or be defined invariant of the data analyzed. On the other hand, it is important to test the resultant vectors for Gaussian distribution and the determination of the x% matrix will be much easier with the vectors.

3 SUMMARIES OF THE EXTRAPOLATION METHODS

Characteristics of the extrapolation methods are summarized from three aspects (the critical factors, the advantages and disadvantages, and the application ranges of each extrapolation method) based on the previous sections.

3.1 Critical Factors

Critical factors in each extrapolation method are summarized in Table 1. These factors are mentioned and emphasized in the preceding part based on the literature and illustrations.

3.2 Advantages and Disadvantages

Based on the literature and illustrations, the advantages and disadvantages of each extrapolation method are summarized in Table 2.

Table 1. *Critical factors in each extrapolation method*

Extrapolation method	Critical factor
PEE	Distribution prediction of the sample data Selection of the distribution function Parameter estimation
EVE	Threshold or block size determination Distribution prediction of the sample data Selection of the distribution function Parameter estimation
NPE	Selection of the kernel function Bandwidth determination
QE	Data characteristics judgment and breaking Resultant vectors test

3.3 Application Ranges

Different extrapolation methods have their own application ranges. In practice, the application ranges of a certain extrapolation method are not categorical. A method has to be selected on the basis of the practical situation. Application ranges of the methods in this paper are mainly based on the load characteristics and extrapolation purposes, which are summarized as follows.

PEE: For sample data, when the stationary test for a certain distribution is qualified, PEE will be an appropriate selection. However, when convenience and efficiency of data processing is required instead of the accuracy, PEE can be considered. For example, in Xiang [20], the distributions of the load amplitudes and mean values fit well with the fitting functions and they are independent, so PEE is adopted.

EVE: EVE is a proper choice in circumstances where the sample data is composed of extreme load. For example, the data in the fields of wind speed and engineering machinery could be extrapolated by EVE. Furthermore, if the purpose is to produce a load time history for fatigue test and fatigue life evaluation, EVET is a better choice because it is capable of extrapolating the load time history directly. EVER is more applicable for accurate load spectrum extrapolation of large load cycles. EVER is also an appropriate choice in circumstances where the load spectrum can be modeled as a Gaussian or Markov model.

NPE: NPE is limited by the sample size of large load cycles. If the sample size is enough, NPE may be a better choice. For extrapolating medium and small load cycles, NPE can be used. When it is difficult to

Table 2. *Advantages and disadvantages of each extrapolation method*

Extrapolation method	Advantages	Disadvantages
PEE	• Computes efficiently [20] and [7]; • Considers the influences of both mean value and amplitude of the sample data [19] and [20].	• Relies on the distribution of the measured data; • There is subjectivity in selecting a parameter-estimate method [26].
EVET	• Gets a load time history directly; • Generated sequence of cycles is realistic; • Robust; • Considers the influence of extreme values.	• The block size and threshold selection has a great influence on the extrapolation accuracy. • Relies on distributions of the sample data ;
EVER	• Estimates the shape of the load spectrum for an infinitely long measurement; • Available for large cycles.	• Produces a rainflow matrix and needs to be converted into a time signal; • Choice of the threshold is difficult. • Relies on distributions of the sample data;
NPE	• Independent of the distributions of the sample data [64]; • Effective estimation of the load spectrum with arbitrary shapes [64].	• Large amount of sample data is needed [64] and [66]; • The kernel function and bandwidth selection is influential.
QE	• The extrapolated samples consider the influence of different conditions and operating behaviours.	• Influential step is breaking the sample data into a series of clusters [64].

define the model of the distribution accurately or there is little dependence on the distribution of the sample data, NPE may be a good choice. For example, in the field of vehicles, the load may be extrapolated by NPE [68].

QE: When different working conditions and operating behaviors are considered, QE will be useful in data processing. For example, due to the complex working conditions of engineering machinery, the load in the field may be extrapolated with QE [4].

4 DISCUSSIONS

Due to the limited paper length, there are some deficiencies in this review. For example, in PE, some other distribution functions should be reviewed, such as the logarithmic normal distribution in PEE and the Rayleigh distribution in EVE. In EVE, the importance of the threshold or block size is verified, but the selecting methods of the threshold or block size should be further discussed. In NPE, the influence of bandwidths on the density distribution is verified, but the difference between the adaptive and fixed bandwidth requires further comparison, and which one is better for a certain situation is not concluded. For QE, where different working conditions are concerned, the process and details of combining QE with other methods are not fully reviewed. Furthermore, one purpose of this review is to provide guidance on selecting an appropriate load extrapolation method for a certain case. In this review, only part of the guidance is involved, so further research on completing the guidance may be useful.

5 CONCLUSIONS

Load extrapolation provides a feasible and reliable approach to obtaining a long-term load spectrum for fatigue analysis and life prediction in engineering. Several commonly used extrapolation methods are reviewed in this paper. Some conclusions are as follows:

1. PEE and EVE are both included in PE. PEE is based on the distributions of the sample data. Specific distribution functions are employed to fit and the parameters in the functions are estimated according to the sample data. The PEE process is simple and efficient, but some errors may arise in the results;
2. EVE is based on EVT. Extreme values obtained by extraction methods such as BMM, POT, and LU are extrapolated by a process similar to PEE, but the distribution functions are usually different. EVE is valid for the load time history with large load cycles, but selecting a proper threshold or block size usually requires further consideration;
3. For extrapolating small and moderate loads, NPE can be applied accompanied by kernel estimation. There is no need to predict the distributions of the sample data and estimate the parameters of the functions in NPE. The rationality of the results extrapolated by NPE is directly influenced by the kernel function and bandwidth, especially the latter;
4. The extrapolation methods mentioned above could be combined with QE when the influences of different working conditions and operating behavior are considered. In QE, determining the solution parameters is an important step.

Some potential future research directions are also predicted:

First, a difference between the extrapolated and measured load always exists, thus an evaluation criterion should be set to evaluate the difference, which may provide important guidance for selecting the appropriate method. Second, the references and applications are mainly about the field of engineering in this review. In fact, extrapolation is being used in many other fields, such as weather prognosis, hydrological forecasting, and financial analysis. Methods from other fields can be borrowed and adopted in another field. In addition, limited by the physical circumstances in engineering, many load spectra have maximum or minimum limits. Extrapolating the sample data appropriately within these limits is challenging. Therefore, research on the appropriate extrapolation may provide another way to optimize the results.

6 ACKNOWLEDGEMENTS

This work was supported by National Natural Science Foundation of China (No. 51375202 and 51075179).

7 REFERENCES

[1] Rychlik, I. (1996). Fatigue and stochastic loads. *Scandinavian Journal of Statistics*, vol. 23, no. 4, p. 387-404.

[2] Maisch, M., Bertsche, B., Hettich, R. (2006). An approach to online reliability evaluation and prediction of mechanical transmission components. *International Journal of Automation and Computing*, vol. 3, no. 2, p. 207-214, **DOI:10.1007/s11633-006-0207-5.**

[3] Bandemer, H. (1980). Statistical analysis of reliability and life-testing models. Theory and Methods. *Journal of Applied*

Mathematics and Mechanics, vol. 60, no. 10, p. 544, **DOI:10.1002/zamm.19800601021**.

[4] Zhang, Y.S. (2014). *Research on the Load Spectra Acquisition and Application of Loader Powertrain*, PhD Thesis, Jilin University, Changchun. (in Chinese)

[5] Owczarek, W., Rodzewicz, M. (2009). Investigations into glider chassis load spectrum. *Fatigue of Aircraft Structures*, no. 1, p. 150-169, **DOI:10.2478/v10164-010-0014-x**.

[6] Katcher, M. (1973). Crack growth retardation under aircraft spectrum loads. *Engineering Fracture Mechanics*, vol. 5, no. 4, p. 793-818, **DOI:10.1016/0013-7944(73)90052-0**.

[7] Rui, Q., Wang, H.Y. (2011). Frequency domain fatigue assessment of vehicle component under random load spectrum. *Journal of Physics: Conference Series*, vol. 305, no. 1, p. 1-9, **DOI:10.1088/1742-6596/305/1/012060**.

[8] Zhang, L.P., Guo, L.X. (2011). The vehicle dynamic load identification under the excitation of random road surface. *Advanced Materials Research*, vol. 299-300, p. 255-259, **DOI:10.4028/www.scientific.net/amr.299-300.255**.

[9] Moriarty, P.J., Holley, W.E., Butterfield, S. (2002). Effect of turbulence variation on extreme loads prediction for wind turbines. *Journal of Solar Energy Engineering*, vol. 124, no. 4, p. 387–395, **DOI:10.1115/1.1510137**.

[10] Veers, P.S., Winterstein, S.R. (1998). Application of measured load to wind turbine fatigue and reliability analysis. *Journal of Solar Energy Engineering*, vol. 120, no. 4, p. 233-239, **DOI:10.1115/1.2888125**.

[11] Wang, J.X., Liang, Y.L., Wang, Z.Y., Wang, N.X., Yao, M.Y., Sun, Y.F. (2011). Test and compilation of load spectrum of hydraulic cylinder for earth moving machinery. *Advanced Science Letters*, vol. 4, no. 6-7, p. 2022-2026, **DOI:10.1166/asl.2011.1661**.

[12] Wang, J., Hu, J., Wang, N., Yao, M., Wang, Z. (2012). Multi-criteria decision-making method-based approach to determine a proper level for extrapolation of Rainflow matrix. *Proceedings of the Institution of Mechanical Engineers, Part C: Journal of Mechanical Engineering Science*, vol. 226, no. 5, p. 1148-1161, **DOI:10.1177/0954406211420212**.

[13] Yamada, K., Cao, Q., Okado, N. (2000). Fatigue crack growth measurements under spectrum loading. *Engineering Fracture Mechanics*, vol. 66, no. 5, p. 483-497, **DOI:10.1016/S0013-7944(99)00143-5**.

[14] O'Connor, A., Caprani, C., Belay, A., (2002). Site-specific probabilistic load modeling for bridge reliability analysis. *Assessment of Bridges and Highway Infrastructure*, p. 97-104.

[15] Heuler, P., Klatschke, H., (2005). Generation and use of standardized load spectra and load–time histories. *International Journal of Fatigue*, vol. 27, no. 8, p. 974-990, **DOI:10.1016/j.ijfatigue.2004.09.012**.

[16] Johannesson, P., Speckert, M. (eds.) (2013). *Guide to Load Analysis for Durability in Vehicle Engineering*. John Wiley & Sons Ltd, Chichester, **DOI:10.1002/9781118700518**.

[17] Johannesson, P., Thomas, J.J., (2001). Extrapolation of rainflow matrices. *Extremes*, vol. 4, no. 3, p. 241-262, **DOI:10.1023/A:1015277305308**.

[18] Chen, A.Y., Gao, Z.T. (1986). Statistical treatment of two-dimensional random fatigue loads and its application. *Journal of Beijing Institute of Aeronautics and Astronautics*, no. 1, p. 75-85, **DOI:10.13700/j.bh.1001-5965.1986.01.009**. (in Chinese)

[19] Ling, J., Gao, Z. T., (1992). The statistical treatment for fatigue loads of a mechanical structure under multi-operating conditions. *Journal of Mechanical Strength*, vol. 14, no. 2, p. 31-34. (in Chinese)

[20] Xiang, C.L. (2007). *Dynamics of Armored Vehicle Transmission System*, National Defense Industry Press, Beijing.

[21] Jia, H.B. (2009). *Study on the Test and Generation Methods about Load Spectrum of Wheel Loader Driveline*. Jilin University, Changchun.

[22] Downing, S.D., Socie, D.F. (1982). Simple rainflow counting algorithms. *International Journal of Fatigue*, vol. 4, no. 1, p. 31-40, **DOI:10.1016/0142-1123(82)90018-4**.

[23] Hong, N. (1991). A modified rainflow counting method. *International Journal of Fatigue*, vol. 13, no. 6, p. 465-469, **DOI:10.1016/0142-1123(91)90481-d**.

[24] Rice, R.E. (1988). F*atigue Design Handbook, 2nd edition*, AE-10, Society of Automotive Engineers.

[25] Wang, R.Q., Wei, J.M. Hu, D.Y., Shen, X.L, Fan, J, (2013). Investigation on experimental load spectrum for high and low cycle combined fatigue test. *Propulsion and Power Research*, vol. 2, no. 4, p. 235-242, **DOI:10.1016/j.jppr.2013.11.004**.

[26] Nagode, M., Fajdiga, M. (1998). A general multi-modal probability density function suitable for the rainflow ranges of stationary random processes. *International Journal of Fatigue*, vol. 20, no. 3, p. 211-223, **DOI:10.1016/s0142-1123(97)00106-0**.

[27] Holling, D., Mueller, A. (1973). Accelerated fatigue-testing improvements from road to laboratory. *SAE Automobile Engineering Meeting*, vol. 2, p. 730564, **DOI:10.4271/730564**.

[28] Weibull, W., (1961). *Fatigue Testing and Analysis of Results*. Macmillan Company, New York.

[29] Bethea, R.M., Rhinehart, R.R. (1991). *Applied Engineering Statistics*. Marcel Dekker, New York.

[30] Fu, H.M., Gao, Z.T. (1990). An optimization method of coefficient optimization for determining a three-parameter Weibull distribution. *Acta Aeronautica et Astronautica Sinica*, vol. 11, no. 7, p. 323-327. (in Chinese)

[31] IEC 61400-1 (2005). *Wind turbines-Part 1: Design requirements. 3rd edition*. International Electrotechnical Commission, Geneva

[32] Liu, Y., Zhang X. F., Wang Z.Y., Liu Q.S., Wang J.X. (2011). Contrast of extrapolations in compiling load spectrum. *Modern Manufacturing Engineering*, no. 11, p. 8-11.

[33] Nicholas, T., Zuiker, J.R. (1996). On the use of the Goodman diagram for high cycle fatigue design. *International Journal of Fatigue*, vol. 80, no. 2, p. 219-235, **DOI:10.1007/bf00012670**.

[34] Nagode, M., Fajdiga, M. (1998). On a new method for prediction of the scatter of loading spectra. *International Journal of Fatigue*, vol. 20, no. 4, p. 271-277, **DOI:10.1016/S0142-1123(97)00135-7**.

[35] Punee, A., Lance, M. (2008). The influence of the joint wind-wave environment on offshore wind turbine support structure loads. *Journal of Solar Energy Engineering*, vol. 130, no. 3, p. 17, **DOI:10.1115/1.2931500**.

[36] Nagode, M., Klemenc, J., Fajdiga, M., (2001). Parametric modelling and scatter prediction of rainflow matrices.

International Journal of Fatigue, vol. 23, no. 6, p. 525-532, **DOI:10.1016/s0142-1123(01)00007-x**.

[37] Agarwal, P., Manuel, L. (2008). Extreme loads for an offshore wind turbine using statistical extrapolation from limited field data. *Wind Energy*, vol. 11, no. 6, p. 673-684, **DOI:10.1002/we.301**.

[38] Moriarty, P.J., Holley, W.E., Butterfield, S.P., (2004). Extrapolation of Extreme and Fatigue Loads Using Probabilistic Methods. National Renewable Energy Laboratory, Golden, **DOI:10.2172/15011693**.

[39] Gumbel, E. (1958). *Statistics of Extremes*. Columbia University Press, New York.

[40] Johannesson, P. (2006). Extrapolation of load histories and spectra. *Fatigue & Fracture of Engineering Materials & Structures*, vol. 29, no. 3, p. 201-207, **DOI:10.1111/j.1460-2695.2006.00982.x**.

[41] Toft, H.S., Søensen, J.D., Veldkamp, D. (2011). Assessment of load extrapolation methods for wind turbines. *Journal of Solar Energy Engineering*, vol. 133, no. 2, **DOI:10.1115/1.4003416**.

[42] Smith, R.L. (1986). Extreme value theory based on the largest annual events. *Journal of Hydrology*, vol. 86, no. 1-2, p. 27-43, **DOI:10.1016/0022-1694(86)90004-1**.

[43] Mudersbach, C., Jensen, J. (2010). Nonstationary extreme value analysis of annual maximum water levels for designing coastal structures on the German North Sea coastline, *Journal of Flood Risk Management*, vol. 3, no. 1, p. 52-62, **DOI:10.1111/j.1753-318x.2009.01054.x**.

[44] Villarini, G., Smith, J.A., Serinaldi, F., Ntelekos, A.A. (2011). Analyses of seasonal and annual maximum daily discharge records for central Europe. *Journal of Hydrology*, vol. 399, no. 3-4, p. 299-312, **DOI:10.1016/j.jhydrol.2011.01.007**.

[45] Marty, C., Blanchet, J. (2012). Long-term changes in annual maximum snow depth and snowfall in Switzerland based on extreme value statistics. *Climatic Change*, vol. 111, no. 3, p. 705-721, **DOI:10.1007/s10584-011-0159-9**.

[46] Ragan, P., Manuel, L. (2008). Statistical extrapolation methods for estimating wind turbine extreme loads. *Journal of Solar Energy Engineering*, vol. 130, no. 3, p. 1-19, **DOI:10.1115/1.2931501**.

[47] Gonzalez, J., Rodriguez, D., Sued, M. (2013). Threshold selection for extremes under a semiparametric model. *Statistical Methods & Applications*, vol. 22, no. 4, p. 481-500, **DOI:10.1007/s10260-013-0234-7**.

[48] Ghosh, S., Resnick, S. (2010). A discussion on mean excess plots. *Stochastic Processes and their Applications*, vol. 120, no. 8, p. 1492-1517, **DOI:10.1016/j.spa.2010.04.002**.

[49] Davison, A.C. (1984). Modelling excesses over high thresholds, with an application. *Statistical Extremes and Applications*, vol. 131, p. 461-482, **DOI:10.1007/978-94-017-3069-3_34**.

[50] Ledermann, W. (ed.) (1990). *Handbook of Applicable Mathematics Volume 7: Supplement*, Wiley-Interscience, Chichester.

[51] Walshaw, D. (1994). Getting the most from your extreme wind data: a step by step guide. *Journal of Research of the National Institute of Standards & Technology*, vol. 99, no. 4, p. 399–411, **DOI: 10.6028/jres.099.038**.

[52] Pickands, J. (1975). Statistical inference using extreme order statistics. *Annals of Statistics*, vol. 3, no. 1, p. 119-131, **DOI:10.1214/aos/1176343003**.

[53] Cerrini, A., Johannesson, P., Beretta, S., (2006). Superposition of maneuvers and load spectra extrapolation. Keogh, P.S. (ed.) *Applied Mechanics and Materials*, no. 5-6, p. 255-262, **DOI:10.4028/www.scientific.net/amm.5-6.255**.

[54] Lourenco, C.M. (2014). Specification test for threshold estimation in extreme value theory. *Journal of Operational Risk*, vol. 9, no. 2, p. 23-37.

[55] Hosking, J.R.M., Wallis, J.R. (1987). Parameter and quantile estimation for the generalized Pareto distribution. *Technometrics*, vol. 29, no. 3, p. 339-349, **DOI:10.1080/00401706.1987.10488243**.

[56] Smith, R.L. (1984). Threshold methods for sample extremes. *Statistical Extremes and Applications,* vol. 131, p. 621-638, **DOI:10.1007/978-94-017-3069-3_48**.

[57] WAFO Group. (2011). *WAFO—a Matlab Toolbox for analysis of random waves and loads, tutorial for WAFO 2.5. Mathematical Statistics*, Lund University, Lund.

[58] Collani, E., Binder, A., Sans, W., Heitmann, A., Al-Ghazali, K. (2008). Design load definition by LEXPOL. *Wind Energy*, vol. 11, no. 6, p. 637-653, **DOI:10.1002/we.290**.

[59] LEXPOL Version 1.0. TÜV Nord, from *http://www.tuev-nord.de/english/42708.asp*, accessed on 2008-10-03.

[60] Agarwal, P., Manuel, L. (2008). Empirical wind turbine load distributions using field data. *Journal of Offshore Mechanics and Arctic Engineering*, vol. 130, no. 1, p. 244-245, **DOI:10.1115/1.2827937**.

[61] Natarajan, A., Holley, W.E., Penmatsa, R., Brahmanapalli, B.C. (2008). Identification of contemporaneous component loading for extrapolated primary loads in wind turbines. *Wind Energy*, vol. 11, no. 6, p. 577-587, **DOI:10.1002/we.304**.

[62] Natarajan, A., Holley, W.E., (2008). Statistical extreme loads extrapolation with quadratic distortions for wind turbines. *Journal of Solar Energy Engineering*, vol. 130, no. 3, **DOI:10.1115/1.2931513**.

[63] Moriarty, P. (2008). Safety-factor calibration for wind turbine extreme loads. *Wind Energy*, vol, 11, no. 6, p. 601-612, **DOI:10.1002/we.306**.

[64] Dressler, K., Gründer, B., Hack, M., Köttgen, V.B. (1996). Extrapolation of rainflow matrices. *SAE Technical*, p. 960569.

[65] Silverman, B.W. (1986). *Density Estimation for Statistics and Data Analysis*. Chapman and hall, New York, **DOI:10.1007/978-1-4899-3324-9**.

[66] Socie, D., Pompetzki, M. (2004). Modeling variability in service loading spectra. *Journal of ASTM International*, vol. 1, no. 2, p. 46-57, **DOI:10.1520/stp11278s**.

[67] Newman, M.E.J., Barkema, G.T. (1999). *Monte Carlo Methods in Statistical Physics*. Oxford University Press, Oxford.

[68] Wang, J.X., Liu, Y. Zeng, X.H. Zhou, Z.P. Wang, N.X., Shen, W.H. (2013). Selection method for kernel function in nonparametric extrapolation based on multi-criteria decision-making technology. *Mathematical Problems in Engineering*, vol. 2013, **DOI:10.1155/2013/391273**.

[69] Heidenreich, N.-B., Schindler, A., Sperlich, S., (2013). Bandwidth selection for kernel density estimation: a review of

fully automatic selectors. *Advances in Statistical Analysis*, vol. 97, no. 4, p. 403-433, **DOI:10.1007/s10182-013-0216-y**.

[70] Sheather, S.J. (2004). Density estimation. *Statistical Science*, vol. 19, no. 4, p. 588-597, **DOI:10.1214/088342304000000297**.

[71] Gangopadhyay, A., Cheun, K. (2002). Bayesian approach to the choice of smoothing parameter in kernel density estimation. *Journal of Nonparametric Statistics*, vol. 14, no. 6, p. 655-664, **DOI:10.1080/10485250215320**.

[72] Zougab, N., Adjabi, S., Kokonendji, C.C., (2014). Bayesian estimation of adaptive bandwidth matrices in multivariate kernel density estimation. *Computational Statistics & Data Analysis*, vol. 75, p. 28-38, **DOI:10.1016/j.csda.2014.02.002**.

[73] Socie, D. (2001). Modelling expected service usage from short-term loading measurements. *International Journal of Materials and Product Technology*, vol. 16, no. 4-5, p. 295-303, **DOI:10.1504/ijmpt.2001.001272**.

[74] Mattetti, M., Molari, G., Sedoni, E. (2012). Methodology for the realization of accelerated structural tests on tractors. B*iosystems Engineering*, vol, 113, no. 3, p. 266-271, **DOI:10.1016/j.biosystemseng.2012.08.008**.

[75] Beirland, J., Teugels, J.L., Vynckier, P. (1996). *Practical Analysis of Extreme Values*, Leuven University Press, Leuven.

[76] Draisma, G., de Haan, L., Peng, L., Pereira, T.T. (1999). A bootstrap-based method to achieve optimality in estimating the extreme-value index. *Extremes*, vol. 2, no. 4, p. 367-404, **DOI:10.1023/A:1009900215680**.

[77] Dress, H., Kaufmann, E. (1998). Selecting the optimal sample fraction in univariate extreme value statistics. *Stochastic Processes and Their Applications*, vol. 75, no. 2, p. 149-172, **DOI:10.1016/s0304-4149(98)00017-9**.

[78] Dupuis, D.J. (1998). Exceedances over high thresholds: A guide to threshold selection. *Extremes*, vol. 1, no. 3, p. 251-261, **DOI:10.1023/A:1009914915709**.

[79] Thompson, P., Cai, Y., Reeve, D., Stander, J. (2009). Automated threshold selection methods for extreme wave analysis. *Coastal Engineering*, vol. 56, no. 10, p. 1013-1021, **DOI:10.1016/j.coastaleng.2009.06.003**.

[80] Rychlik, I. (1996). Simulation of load sequences from rainflow matrices: Markov method. *International Journal of Fatigue*, vol. 18, no. 7, p. 429-438, **DOI:10.1016/0142-1123(96)80001-z**.

[81] Scott, D.W. (1992). *Multivariate Density Estimation: Theory, Practice, and Visualization*, John Wiley & Sons, New York, **DOI:10.1002/9780470316849**.

[82] Mugdadi, A.R., Ahmad, I.A., (2004). A bandwidth selection for kernel density estimation of functions of random variables. *Computational Statistics & Data Analysis*, vol. 47, no. 1, p. 49-62, **DOI:10.1016/j.csda.2003.10.013**.

List of reviewers who reviewed manuscripts in 2015

Boris Aberšek, Slovenia
Bojan Ačko, Slovenia
Mike Adams, UK
Dragan Aleksendrić, Serbia
Hafiz Muhammad Ali, Pakistan
Luis F. Almeida, Brazil
Abdullah Altin, Turkey
Miha Ambrož, Slovenia
Ciril Arkar, Slovenia
Fausto Arpino, Italy
Kamil Arslan, Turkey
Viktor P. Astakhov, USA
Ayyanar Athijayamani, India
Csobán Attila, Hungary
Önder Ayer, Turkey
Aleš Babnik, Slovenia
Tom Bajcar, Slovenia
Ivan Bajsić, Slovenia
Pedro P. Balestrassi, Brazil
Jože Balič, Slovenia
Serkan Balli, Turkey
Sebastian Baloš, Serbia
Mustapha Barakat, France
Nilson Barbieri, Brazil
Jani Barle, Slovenia
Cemal Baykara, Turkey
Bernd-Arno Behrens, Germany
Josep M. Bergada, Spain
Tomaž Berlec, Slovenia
Pablo Dolado Bielsa, Spain
Ignacijo Biluš, Slovenia
Benjamin Bizjan, Slovenia
Gunnar Bolmsjö, Sweden
Miha Boltežar, Slovenia
Éd Claudio Bordinassi, Brazil
Lincoln Cardoso Brandao, Brazil
Josip Brnić, Croatia
Mihael Bruncko, Slovenia
Charles-Henri Bruneau, France
Bruno Brunone, Italy
Borut Buchmeister, Slovenia
Juana Abenójar Buendía, Spain
Tomasz Adam Bulzak, Poland
Peter Butala, Slovenia
Vincenc Butala, Slovenia
Hrvoje Cajner, Croatia
M. Cali, Italy
Colin C. Caprani, Australia
Paolo Casoli, Italy
Ramón Barber Castaño, Spain
Kadir Cavdar, Turkey
Onur Çavuşoğlu, Turkey
Marco Ceccarelli, Italy
H. Kursat Celik, Turkey
Yikai Chen, China
Peng Cheng, USA
Simone Chiappino, Italy
Chong-Du Cho, South Korea
Christian Cierpka, Germany
Snezana Ciric-Kostic, Serbia
Franco Concli, Italy
Mario Costa, Portugal
Dario Croccolo, Italy
Gregor Čepon, Slovenia
Martin Česnik, Slovenia
Mirko Čudina, Slovenia
Franci Čuš, Slovenia
Jos Darling, UK
Marta Cristina Cardoso de Oliveira, Portugal
Marco Dell'Isola, Italy
Edvard Deticek, Slovenia
Andrew J. Dick, USA
Anselmo Eduardo Diniz, Brazil
Norman E. Dowling, USA
Janko Drnovšek, Slovenia
Jožef Duhovnik, Slovenia
Matevž Dular, Slovenia
Mihai Dupac, UK
Milan Edl, Slovenia
Igor Emri, Slovenia
Ahmet Erklig, Turkey
Nadimul Faisal, UK
Cuneyt Fetvaci, Turkey
Giorgio Ficco, Italy
Mirko Ficko, Slovenia
Aleš Fidler, Slovenia
Bogdan Filipič, Slovenia
Jože Flašker, Slovenia
Abbas Fotouhi, UK
Livan Fratini, Italy
Wolfgang Fricke, Germany
Patricia Frontini, Argentina
Andrés Gabriel García, Argentina
Emin Germen, Turkey
Hossein Gholizadeh, Canada
Mostafa Ghoreyshi, Iran
Gilbert-Rainer Gillich, Romania
Steven D. Glaser, USA
Alexey M. Glushenkov, Australia
Darko Goričanec, Slovenia
Kursad Gov, Turkey
Edvard Govekar, Slovenia
Adriana Greco, Italy
Niccolo Grossi, Italy
Janez Grum, Slovenia
Recep Gunes, Turkey
Leo Gusel, Slovenia
Aleš Hace, Slovenia
Jiří Hájek, Czech Republic
Miroslav Halilovič, Slovenia
Niels Hansen, Denmark
Guangbo Hao, Ireland
Sebastian Härtel, Germany
Boshu He, China
Rogelio L. Hecker, Argentina
Niko Herakovič, Slovenia

The Editorial would like to thank all the reviewers in participating in reviewing process.
We appreciate the time and effort and greatly value the assistance as a manuscript reviewer for Strojniški vestnik – Journal of Mechanical Engineering.

Vsebina

Strojniški vestnik - Journal of Mechanical Engineering
letnik 62, (2016), številka 1
Ljubljana, januar 2016
ISSN 0039-2480

Izhaja mesečno

Razširjeni povzetki (extended abstracts)

Strojniški vestnik - Journal of Mechanical Engineering 62(2016)1, SI 3

Prejeto v recenzijo: 2015-10-17
Prejeto popravljeno: 2015-11-17
Odobreno za objavo: 2015-11-24

Kompenzacija periodične optične distorzije pri metodi sledenja delcev na valovitih ploščnih prenosnikih toplote

Jaka Pribošek[1,*] – Miha Bobič[2] – Iztok Golobič[1] – Janez Diaci[1]

[1] Univerza v Ljubljani, Fakulteta za strojništvo, Slovenija
[2] Danfoss Trata, Slovenija

Optimizacija valovitih ploščnih prenosnikov toplote je bila dotlej omejena na numerične CFD simulacije, pri čemer pa spričo zaprte konstrukcije tovrstnih prenosnikov, eksperimentalna validacija teh simulacij ostaja nenaslovljena. Ker so tokovni pojavi v valovitih prenosnikih navadno kompleksne narave, je za uspešno validacijo nujna kvantitativno spremljanje celotnega tokovnega polja znotraj prenosnikov.

V ta namen smo na valovitih ploščnih prenosnikih toplote vpeljali metodo sledenja delcev. Za neposredno vizualizacijo toka v prenosniku je bil izdelan lasten eksperimentalni sistem, kjer je bila ena od kovinskih plošč ploščnega prenosnika zamenjana s prozorno polimerno ploščo.

Prozorna plošča je bila izdelana po postopkih vročega vtiskovanja in sicer tako, da njena geometrija popolnoma ustreza nadomeščeni kovinski plošči. Tak kompozitni sestav omogoča prosto vizualizacijo tokov znotraj prenosnika, vendar valovitost prozorne plošče in razlike v lomnem količniku vnesejo pojav kompleksne periodične optične distorzije. Optična distorzija močno popači trajektorije sledenih delcev, kar v meritev vnese veliko sistematično napako ter onemogoča direktno rabo obstoječih metod sledenja delcev.

V pričujočem članku predstavljamo metodo eksperimentalne identifikacije optične distorzije s pomočjo vzorca v obliki šahovnice ter lastnega algoritma na osnovi obdelave slik. Algoritem detektira popačenost slike šahovnice, ter iz nje določi iskano polje deformacij. Za boljši popis deformacij vpeljemo nov model periodične distorzije na osnovi diskretne kosinusne transformacije, ki znatno izboljša krajevno ločljivost zaznanih deformacijskih polj. Razvita metoda nam omogoča kompenzacijo vpliva optične distorzije na popačitev trajektorij sledenih delcev ter s tem eliminacijo sistematično napako meritev položaja delcev. Pravilnost delovanja algoritmov smo preverili z vrsto simulacijskih eksperimentov na znanih enodimenzionalnih hitrostnih poljih, kjer smo lahko eksperimentalno ovrednotili sistematično položajno napako delcev pred in po kompenzaciji. Sistematična napaka položaja delcev je bila v teh primerih s pomočjo razvite metode zmanjšana za več kot 50 %. Razvite algoritme za kompenzacijo tokovnic smo aplicirali tudi na realnem primeru na prenosniku med obratovanjem. Pri tem je bila sistematična napaka v določanju položaja delcev zmanjšana za 35 %.

Pričujoč članek predstavlja pionirsko delo na področju kvantitativne analize valovitih ploščnih prenosnikov toplote v svetovni javnosti. Naše nadaljnje delo bo naravnano v smeri uporabe obstoječih algoritmov za merjenje tridimenzionalnih velikostnih polj znotraj valovitih toplotnih prenosnikov za namene njihove eksperimentalne optimizacije ter validacije večjega števila obstoječih numeričnih analiz.

Ključne besede: periodična optična distorzija, metoda sledenja delcev, valoviti ploščni prenosniki toplote, optimizacija ploščnih prenosnikov, eksperimentalna validacija numeričnih analiz

*Naslov avtorja za dopisovanje: Univerza v Ljubljani, Fakulteta za strojništvo, Aškerčeva 6, 1000 Ljubljana, Slovenija, jaka.pribosek@fs.uni-lj.si

Strojniški vestnik - Journal of Mechanical Engineering 62(2016)1, SI 4

Prejeto v recenzijo: 2015-05-22
Prejeto popravljeno: 2015-09-14
Odobreno za objavo: 2015-11-09

Analiza natančnosti dveh modelov rekonstruiranih zob, izdelanih s tehnologijo 3DP in FDM

Grzegorz Budzik – Jan Burek – Anna Bazan – Paweł Turek
Tehniška univerza v Rzeszowu, Oddelek za strojništvo, Poljska

Dodajalne izdelovalne tehnologije (AM) imajo na področju biomedicine pomembne prednosti pred postopki izdelave z odvzemanjem materiala, še posebej takrat, ko gre za gradnjo kompliciranih oblik človeške anatomije in kompleksnih poroznih mikrostruktur. Na trgu je veliko naprav, ki uporabljajo dodajalne izdelovalne tehnologije. Vsaka od njih ima posebne lastnosti in zahteve glede materialov, pogojev okolice, temperature procesa in korakov končne obdelave modela. Prav zaradi raznolikosti omenjenih lastnosti in različne razpoložljivosti tehnologij za hitro izdelavo prototipov (RP) danes še nobena od njih nima dominantnega položaja na področju aplikacij v medicini, kar velja tudi za dentalno kirurgijo.

Tehnologije RP odpirajo nove priložnosti na področju razvoja aplikacij po meri, kot je izdelava dentalnih modelov. Znanstveniki še vedno raziskujejo, kako doseči zadostno natančnost v fazi obdelave podatkov, pridobljenih med skeniranjem pacientove anatomije, ter kako izboljšati kakovost dentalnih modelov, izdelanih po postopkih RP, iščejo pa tudi optimalen merilni sistem za kontrolo dimenzij.

Namen te raziskave je analiza natančnosti modelov dveh zob, izdelanih z različnimi postopki RP. Za raziskavo sta bila izbrana 3D-tiskanje (3DP) in neprekinjeno ciljno nalaganje (FDM), ker spadata med najbolj razširjene postopke RP in sta povezana z razmeroma majhnimi stroški. Dodatni cilj tega članka je tudi ovrednotenje primernosti mikroskopa s spremenljivim goriščem (FV) za uporabo v funkciji merilnega sistema za kontrolo majhnih predmetov s kompleksno geometrijo, kot so dentalni modeli.

Tridimenzionalni računalniški modeli dveh zob so bili pridobljeni s skeniranjem pacientove spodnje čeljusti po metodi računalniške tomografije s stožčastim snopom (CBCT), ki mu je sledilo segmentiranje zob na podlagi izmerjenih podatkov. Geometrija zob je bila najbolje rekonstruirana pri vokslih izotropnih dimenzij 0,2 mm x 0,2 mm x 0,2 mm. Pri 3D-rekonstrukciji sta bili za modele zob uporabljeni enaki Hounsfieldova vrednost (1254HU) in metoda segmentacije (rast območja). 3D-geometrija je bila popolnoma rekonstruirana z algoritmom Marching cubes, eno od metod za upodabljanje površin.

Modeli so bili izdelani po postopkih 3DP in FDM. Modeli so bili analogno orientirani v delovnem prostoru obeh tiskalnikov, s čimer so bili zagotovljeni podobni pogoji pri tiskanju, prav tako pa je bila nastavljena podobna debelina slojev 0,1 mm oz. 0,13 mm. Natisnjeni modeli so bili nato poskenirani z mikroskopom s spremenljivim goriščem (FV), in sicer po delih zaradi kompleksne geometrije.

Skenirana geometrija modelov dveh zob je bila primerjana s pripadajočimi CAD-modeli. Primerjava je bila opravljena tako za posamezne dele kakor tudi za sestavljene modele zob. Opravljen je bil proces iskanja najboljšega prilega s pogojem natančnosti prilega 0,001 mm. Natančnost izdelanih modelov je vsota napak pri skeniranju, napak pri izdelavi in uporabljenega algoritma za iskanje najboljšega prilega. Pri zobeh s kompleksnejšo geometrijo je med procesom iskanja prilega prišlo do prepoznavnih napak. Pri sestavih je bil dosežen boljši prileg kot pri posameznih delih. Modeli, izdelani po postopku FDM, so bili natančnejši od modelov, izdelanih po postopku 3DP. Vzrok je v infiltraciji, ki se uporablja pri modelih 3DP. Da bi bilo mogoče napovedovati končne dimenzije in doseči zahtevano natančnost modelov 3DP, bi bilo treba izvesti še dodatne študije.

Metoda spreminjanja gorišča je uporabna za merjenje delov kompleksnih oblik, kot so zobne krone in korenine. Dosežena natančnost meritev je bila bistveno večja od natančnosti uporabljenih postopkov tiskanja in zato lahko privzamemo, da je merilna napaka zanemarljiva. Metoda spreminjanja gorišča je dobra alternativa za postopke, ki se trenutno uporabljajo pri merjenju razmeroma majhnih in kompleksnih dentalnih modelov.

Ključne besede: dentalni model, vzvratno inženirstvo, hitra izdelava prototipov, spreminjanje gorišča

*Naslov avtorja za dopisovanje: Tehniška univerza v Rzeszowu, Oddelek za strojništvo, Poljska, pturek@prz.edu.pl

Strojniški vestnik - Journal of Mechanical Engineering 62(2016)1, SI 5

Prejeto v recenzijo: 2015-07-10
Prejeto popravljeno: 2015-09-18
Odobreno za objavo: 2015-10-08

Raziskava interakcij med rotorjem in statorjem ter nestacionarnosti toka pri centrifugalni črpalki z majhno specifično hitrostjo

Ning Zhang* – Minguan Yang – Bo Gao – Zhong Li – Dan Ni
Univerza Jiangsu, Šola za energetiko, Kitajska

Nestacionarni tlačni impulzi zaradi interakcij med fluidom in konstrukcijo pomembno vplivajo na stabilno in varno delovanje centrifugalnih črpalk. Zaradi intenzivne interakcije med kolesom in ohišjem (rotorjem in statorjem) nastajajo močne vibracije, ki lahko nepričakovano poškodujejo mehanske komponente. Zato je nujna analiza nestacionarnih tokovnih struktur, še posebej porazdelitve vrtincev v črpalki, za pojasnitev vpliva dinamike odlepljanja vrtincev na sprednjem robu lopatice na tlačne impulze. Predstavljena študija analizira nestacionarno interakcijo rotorja in statorja pri centrifugalni črpalki z majhno specifično hitrostjo. Pridobljeni so bili signali tlačnih impulzov skupaj s porazdelitvijo vrtincev. Posebna pozornost je bila posvečena odlepljanju vrtinčastih struktur v vrtinčni sledi na sprednjem robu lopatice ter interakciji z jezikom ohišja. Podrobno je bila analizirana evolucija vrtinčnih struktur v okolici jezika in v kanalu lopatice. Namen tega dela je ugotovitev povezav med tlačnimi impulzi in nestacionarnimi tokovnimi strukturami.

V predstavljeni študiji so bile za ugotovitev notranjih povezav med tlačnimi impulzi in nestacionarnimi tokovnimi strukturami analizirane nestacionarne interakcije med rotorjem in statorjem ter tokovne strukture po metodi LES. Za zaključevanje enačb je bil uporabljen SGS-model Smagorinsky-Lilly. Numerična metoda je bila validirana z eksperimenti.

Kotne porazdelitve amplitude tlaka v f_{BPF} nakazujejo značilen moduliran vzorec zaradi intenzivne interakcije med rotorjem in statorjem. Amplituda tlaka v f_{BPF} vzdolž ohišja pri imenskem pretoku kaže tendenco po zmanjševanju v območju, oddaljenem od jezika ohišja, kar lahko pripišemo širjenju reže med kolesom in ohišjem. V srednjem delu kolesa so bili ugotovljeni štirje različni vzorci območij vrtinčenja. Očitno je, da je vrtinčna struktura, ki se loči v vrtinčni sledi na izstopu lopatice, v intenzivni interakciji z jezikom ohišja. Kombinirana analiza tlačnih impulzov in vrtinčne strukture je pokazala, da je amplituda tlačnih impulzov odvisna od velikosti vrtinca. Ko lopatica prehaja mimo jezika ohišja, gorvodni učinek jezika ohišja pomembno vpliva na porazdelitev vrtincev na tlačni strani lopatice. Pri pretokih, ki se razlikujejo od projektiranih, se vrtinčne strukture na sesalni strani lopatice pri $1{,}4 \times Q_d$, na sprednjem robu lopatice in v okolici jezika pri $0{,}2 \times Q_d$ močno razlikujejo od struktur pri imenskem pretoku.

Podroben in natančen opis nestacionarnih tokovnih struktur v modelski črpalki je težavna naloga. V tej študiji ni bilo mogoče zajeti procesa evolucije odlepljanja vrtinca od sprednjega roba lopatice. V nadaljnjih študijah bi bilo zato treba uporabiti finejšo mrežo in več računskih zmogljivosti za razkritje procesa odlepljanja vrtinčne strukture na sprednjem robu lopatice in mehanizma interakcije z jezikom ohišja. Z eksperimentalno raziskavo tlačnih impulzov in nestacionarnimi meritvami PIV bi bilo mogoče validirati numerične rezultate ter pridobiti celovit pregled nad interakcijami med rotorjem in statorjem v centrifugalnih črpalkah.

Razjasnitev interakcij med rotorjem in statorjem pri centrifugalnih črpalkah je klasičen raziskovalni cilj. Objavljene raziskave obravnavajo bodisi amplitudo tlaka v f_{BPF} bodisi nestacionarne tokovne strukture. V splošnem velja, da je amplituda tlaka odvisna predvsem od interakcij med rotorjem in statorjem, sami vplivi na interakcijo med rotorjem in statorjem pa so le redko predmet raziskav.

Članek razkriva evolucijo odlepljanja vrtinca na sprednjem robu lopatice in njegovo interakcijo z jezikom ohišja. Analizirani so tudi dejavniki, ki vplivajo na amplitudo tlaka, kar je v objavljeni literaturi redkost. Raziskava tako prispeva k izboljšanemu razumevanju interakcij med rotorjem in statorjem.

Ključne besede: centrifugalna črpalka, simulacija velikih vrtincev, nestacionaren tok, interakcije med rotorjem in statorjem, tlačni impulzi, vrtinčna struktura

*Naslov avtorja za dopisovanje: Univerza Jiangsu, Šola za energetiko, Xuefu road 301, Zhenjiang, Kitajska, zhangningwlg@163.com

Strojniški vestnik - Journal of Mechanical Engineering 62(2016)1, SI 6

Prejeto v recenzijo: 2015-04-17
Prejeto popravljeno: 2015-10-12
Odobreno za objavo: 2015-11-09

Uporaba lupin iz sendvič kompozitov pri tlačnih posodah za tankerje za ukapljen naftni plin

Veysel Alankaya[1,*] – Fuat Alarçin[2]

[1]Turška pomorska akademija, Oddelek za ladjedelništvo, Turčija
[2]Tehniška univerza Yıldız, Oddelek za ladijsko strojništvo, Turčija

Naftni plin kot alternativa za kurilno olje je na voljo po nižjih tržnih cenah in je primeren za mnoge namene, med drugim: (i) za osnovne gospodinjske potrebe, kot sta kuhanje in ogrevanje, (ii) za industrijske potrebe v elektrarnah, industriji plastike in kemični industriji, (iii) kot pogonsko gorivo za transport. Izkoriščanje tega potenciala zahteva izgradnjo distribucijskih omrežij s plinovodi za infrastrukturna območja, skladiščne zmožnosti za terensko uporabo in rešitve za transport po morju. Rast trgovskih ladjevij zahteva tankerje z večjimi kapacitetami za transport plina, vendar z minimalno težo. Prednostna rešitev za izpolnitev te zahteve so kompozitni materiali, ki imajo veliko razmerje med togostjo in težo. Namen te študije je preučitev primernosti lupin iz sendvič kompozitov v vlogi konstrukcijskih delov cilindričnih ali sferičnih rezervoarjev, in sicer z analizo porazdelitve napetosti po debelini lupine in deformacij lupin pod tlačno obremenitvijo.

Uporaba kompozitnih materialov je povezana z določenimi težavami pri analizi, kot so medslojne ali transverzalne strižne napetosti zaradi neujemanja materialnih lastnosti med sloji, sklapljanje upogibanja in natezanja zaradi asimetrične laminacije, in ravninska ortotropija. Transverzalne komponente napetosti in deformacij se v teoriji klasičnih ali tankih lupin zanemarijo, zato te teorije niso primerne za analizo debelejših lupin. Zanesljivo napovedovanje deformacij in napetosti v debelejših konstrukcijah tako zahteva uporabo strižno-deformacijskih teorij višjega reda na osnovi ekspanzije ravninskih odmikov tretjega ali višjega reda. Teorije višjega reda uvajajo dodatne neznanke, za katere je težje poiskati fizikalno interpretacijo, iskanje rešitev pa zahteva tudi več matematičnih izračunov.

Za učinkovito in točno analizo podrobnosti zasnove so nujne ustrezne tehnike v povezavi z dobrimi strukturnimi modeli, zato obstaja potreba po razvoju metodologije reševanja, ki bi upoštevala dodatne kompleksnosti zaradi robnih pogojev, ki izključujejo tradicionalne analitične pristope po Navierju ali Levyju. Ta študija preučuje statični odklon cilindričnih in sferičnih tlačnih posod iz sendvič kompozitov z uporabo teorije strižnih deformacij višjega reda. Vplivi predpisanih robnih pogojev na funkcije za reševanje so dostopni v literaturi, v tej študiji pa so bili razviti posebej za sendvič kompozite. Metodologija za analizo napetosti in deformacij bazira na teoriji strižnih deformacij višjega reda (HSDT). Za reševanje visoko sklopljenih linearnih parcialnih diferencialnih enačb je bil uporabljen pristop mejno nezvezne posplošene dvojne Fourierjeve vrste. Dodatne robne omejitve so bile uvedene z mejnimi nezveznostmi, ustvarjenimi z izbranimi robnimi pogoji za izpeljavo komplementarne rešitve. Predstavljene so numerične rešitve za laminirane sendvič lupine cilindrične in sferične geometrije, ki prevladujejo pri tlačnih posodah.

Nadaljnji rezultati so zbrani v nadaljevanju:

- Prediktivna ocena razvite metodologije reševanja je predstavljena s primerjavo numeričnih rezultatov rešitev FSDT in MKE.
- Čeprav je metoda končnih elementov v raziskovalnih sferah močno razširjena, je prednost predstavljene metodologije za cilindrične in sferične sendvič lupine v tem, da zahteva manjše računske zmogljivosti.
- Vpliv debeline jedrne plasti na normalizirani centralni odklon lupine je signifikanten. Debelina jedrnega sloja, kot eden glavnih parametrov, je zato uporabna za spreminjanje geometrije rezervoarjev za ukapljen naftni plin.
- Geometrija kot naslednji glavni parameter zasnove rezervoarjev ima velik vpliv na vrednosti odklona. Ukrivljenost lupine zmerno vpliva na centralni odklon.
- Pomemben je tudi vpliv debeline jedrnega sloja na porazdelitev medslojnih napetosti. Povečanje debeline prinese občutno zmanjšanje porazdelitve medslojnih napetosti.

Ključne besede: sendvič kompoziti, analiza po metodi končnih elementov, teorija strižnih deformacij višjega reda, mejna nezveznost, tlačne posode, dvakrat ukrivljena lupina, tankerji za ukapljen naftni plin

*Naslov avtorja za dopisovanje: Turška pomorska akademija, Oddelek za ladjedelništvo, Tuzla, 34942 Istanbul, Turčija, valankaya@dho.edu.tr

Strojniški vestnik - Journal of Mechanical Engineering 62(2016)1, SI 7

Prejeto v recenzijo: 2015-09-21
Prejeto popravljeno: 2015-11-03
Odobreno za objavo: 2015-11-19

Vpliv razmerja iztiskavanja na kontaktne napetosti in elastične deformacije matrice pri hladnem protismernem iztiskavanju

Tomaž Pepelnjak[1,*] – Mladomir Milutinović[2] – Miroslav Plančak[2] –
Dragiša Vilotić[2] – Saša Randjelović[3] – Dejan Movrin[2]

[1] Univerza v Ljubljani, Fakulteta za strojništvo, Slovenia
[2] Univerza v Novem Sadu, Fakulteta tehniških znanosti, Serbia
[3] Univerza v Nišu, Fakulteta za strojništvo, Serbia

V članku je obravnavan problem elasto-plastičnega obnašanja sistema orodje-preoblikovanec za postopek protismernega iztiskavanja. Dobro poznavanje velikih tlačnih obremenitev orodja je neobhodno tako za konstrukcijo orodja kot tudi za opredelitev izdelovalne natančnosti samega preoblikovalnega procesa. V ta namen je potrebno združiti teoretska znanja, meritve opazovanih veličin in numerične analize s katerimi vnaprej napovedujemo pojave pri izdelovalnih procesih.

V članku je predstavljena porazdelitev napetosti v kontaktu orodje-preoblikovanec kot tudi elastična deformacija orodja pri procesu hladnega protismernega iztiskavanja. Slednja se pojavi kot posledica obremenitev orodja zaradi plastične deformacije preoblikovanega jeklenega surovca. Analize kontaktnih tlakov in elastičnih deformacij so bile analizirane eksperimentalno in numerično z metodo končnih elementov.

Za eksperimentalno določanje kontaktnih tlakov obstaja več merilnih metod. Pri predstavljenih rasziskavah je bila uporabljena meritev s palično tlačno merilno celico, ki meri obremenitve orodja neposredno na njegovi površini. Za zasledovanje kontaktnih tlakov na aktivni površini orodja za protismerno iztiskavanje je bilo zasnovano posebno orodje z vgrajenim zaznavalom, ki se ga vstavlja na različne lokacije v orodju. S tem je bil analiziran tlak pri različnih pomikih gibljivega dela orodja in ovrednoteno njegovo spreminjanje med preoblikovalnim postopkom.

Raziskave so bile usmerjene v določitev vpliva razmerja iztiskavanja na porazdelitev kontaktnih tlakov. V ta namen je bilo uporabljenih pet različnih premerov pestičev, ki zagotavljajo različne stopnje protismernega iztiskavanja. V naslednjem koraku se je na osnovi izmerjenih kontaktnih tlakov in preračuna z Lamejevo enačbo določilo radialne pomike notranje stene matrice. Izvedena je bila primerjalna analiza dobljenih rezultatov in preračunov z metodo končnih elementov. Za analize z metodo končnih elementov je bil izbran komercialni računalniški program Simufact.forming.

Na osnovi meritev kontaktnih tlakov in rezultatov numeričnih simulacij se je v prvi fazi primerjave preverilo natančnost numeričnih izračunov. Primerjava je pokazala, da numerični izračuni izkazujejo višje vrednosti maksimalnih radialnih napetosti v primerjavi z eksperimentalno določenimi za vse vrednosti razmerja iztiskavanja e_p. Numerične vrednosti maksimalnih radialnih napetosti so od eksperimentalnih večje med 14,8 % in 23,7%.

Elastična deformacija orodja vpliva tudi na natančnost izdelovalnega procesa. Z numeričnimi simulacijami se je ovrednotilo vpliv elastične obremenitve in radialne deformacije matrice na natančnost izdelovalnega postopka. Za protismerno iztiskavanje ob največji analizirani deformaciji prečnega preseka z vrednostjo e_p = 2.11 so numerične simulacije pokazale, da se velikost odstopka zunanjega premera izdelka giblje v toleračnih razredih od IT8 do IT11. Velikost toleračnega razreda je odvisna od višine protismerno iztisnjenega dela – večja je globina iztiskavanja, večji je izdelovalni toleračni razred.

Primerjalne analize vseh treh raziskovalnih konceptov so pokazale njihove prednosti in slabosti. Pri tem se je analizirala predvsem primernost uporabe Lamejeve enačbe in uporabnost palične tlačne celice za merjenje kontaktnih tlakov pri postopkih iztiskavanja za vključevanje v nadaljnje raziskovalno delo. Razlika med izračunanimi radialnimi pomiki dobljenimi z Lamejevo enačbo in numerično izračunanimi vrednostmi je prečejšnja. Izkaže se, da je ta razlika precej večja kot primerjava eksperimentalnih in numeričnih izračunanih vrednost. Iz navedenega lahko povzamemo, da je izračun po Lamejevi enačbi pomanjkljiv in le omejeno uporaben pri analizah obremenitev in deformacij orodij za masivno preoblikovanje.

Ključne besede: protismerno iztiskavanje, kontaktne napetosti, elastična deformacija matrice, palična tlačna merilna celica, metoda končnih elementov

*Naslov avtorja za dopisovanje: Univerza v Ljubljani, Fakulteta za strojništvo, Aškerčeva 6, SI-1000 Ljubljana, Slovenija, tomaz.pepelnjak@fs.uni-lj.si

Strojniški vestnik - Journal of Mechanical Engineering 62(2016)1, SI 8

Prejeto v recenzijo: 2015-09-21
Prejeto popravljeno: 2015-12-07
Odobreno za objavo: 2015-12-10

Algoritem za izračunavanje odstopanja oblike pri koordinatnih meritvah površine izdelkov poljubnih oblik

Marek Magdziak*
Tehniška univerza v Rzeszowu, Fakulteta za strojništvo in aeronavtiko, Poljska

Glavni cilj predstavljene raziskave je bil razvoj nove metode za izračunavanje odstopanja oblik, ki bo uporabna pri koordinatnih meritvah površin izdelkov poljubnih oblik. Nova metoda mora biti primerna tudi za programsko opremo koordinatnih merilnih strojev.

Predlagani algoritem za vrednotenje odstopanja oblik bazira na metodi interpolacije korigiranih merilnih točk po Lagrangeu in Čebišovu. Algoritem razdeli točke, ki jih izmeri koordinatni merilni stroj, v skupine po pet točk. Skupine se interpolirajo po obeh omenjenih metodah interpolacije in pri tem se oblikujejo skupine polinomskih krivulj četrtega reda, ki predstavljajo dejansko obliko merjenca.

V članku so predstavljeni rezultati numeričnih in eksperimentalnih preiskav, povezanih s predlaganim algoritmom. Numerične preiskave vključujejo simulacijo kontaktnih koordinatnih meritev izdelkov na koordinatnem merilnem stroju. Merjeni izdelki so bili prostih oblik, za katere je značilna spremenljiva ukrivljenost in posledično stopnja geometrijske kompleksnosti. V simulacijah so bile generirane izmerjene točke na različnih oddaljenostih od imenskih profilov. Raztros merilnih točk je posledica nenatančnosti postopkov izdelave merjencev ter nenatančnosti koordinatnih meritev analiziranih predmetov. Rezultati simulacij so bili eksperimentalno preverjeni z realnimi kontaktnimi meritvami na koordinatnem merilnem stroju *ACCURA II*.

Predstavljena metoda izboljšuje natančnost meritev površin izdelkov poljubnih oblik. Predlagani algoritem za izračunavanje odstopanja oblik zagotavlja boljše rezultate preizkusov kot metoda na podlagi nominalnih točk v programski opremi Calypso. Prednost predlagane metode je v možnosti izbire primernega algoritma za interpolacijo izmerjenih točk. Razviti algoritem je poleg tega mogoče implementirati v večini programskih paketov za meritve in programska oprema Calypso konkretno omogoča implementacijo s pomočjo modula PCM. Uporabnik lahko v tem okolju uporablja zunanje uporabniško definirane procedure in izvaja uporabniške programe. S takšnim pristopom so mu na voljo izboljšane možnosti za analizo rezultatov koordinatnih meritev.

Predlagani algoritem se lahko v prihodnjih raziskavah podrobneje verificira z realnimi koordinatnimi meritvami. Meritve se lahko opravijo tudi z drugačnimi merilnimi parametri od tistih, ki so bili analizirani v študijah.

Glavna inovacija novega algoritma za izračunavanje odstopanja oblik je v tem, da se interpolacija merilnih točk izvaja po metodah Lagrangea in Čebišova. Te interpolacijske metode niso na voljo v programski opremi uporabljenega koordinatnega merilnega stroja.

Ključne besede: koordinatna merilna tehnika, poljubna oblika, interpolacija, odstopanje oblike

*Naslov avtorja za dopisovanje: Tehniška univerza v Rzeszowu, Fakulteta za strojništvo in aeronavtiko, 35-959 Rzeszów, Poljska, marekm@prz.edu.pl

Strojniški vestnik - Journal of Mechanical Engineering 62(2016)1, SI 9

Prejeto v recenzijo: 2015-07-23
Prejeto popravljeno: 2015-11-10
Odobreno za objavo: 2015-12-10

Pregled metod ekstrapolacije pri zbiranju spektrov obremenitev

Jixin Wang* – Hongbin Chen – Yan Li – Yuqian Wu – Yingshuang Zhang
Univerza v Jilinu, Fakulteta za tehniške vede in strojništvo, Kitajska

Spektri obremenitev predstavljajo osnovo za analizo utrujanja in napovedovanje življenjske dobe v strojništvu. Ekstrapolacija obremenitev je nepogrešljiv postopek za določanje dolgoročnega spektra obremenitev. V zadnjih desetletjih je bilo predlaganih več metod ekstrapolacije in izbiranje ustrezne med njimi je pomemben korak, ki zahteva več pozornosti. Članek podaja pregled pogosto uporabljenih metod ekstrapolacije ter povzetek njihovih načel in lastnosti. Podane so tudi smernice pri izbiri ter nekatere omejitve in smeri raziskav na tem področju.

V tem pregledu se metode ekstrapolacije glede na to, ali je privzeta določena porazdelitev vzorčnih podatkov, delijo na parametrične metode ekstrapolacije (PE) in neparametrične metode ekstrapolacije (NPE). Metode PE se z ozirom na predmete ekstrapolacije in osnovno teorijo delijo tudi na metode ekstrapolacije z ocenjevanjem parametrov (PEE) in metode ekstrapolacije z ekstremnimi vrednostmi (EVE). Dodatno je pregledana še kvantilna metoda ekstrapolacije (QE). Po predstavitvi postopkov posameznih metod je podana pripadajoča literatura za nadaljnji študij. Metode in osnovna načela so nato strnjeni v obliki preglednega diagrama. Prikazanih je nekaj ilustracij ter primerov za vrednotenje in demonstracijo metod. Na podlagi ilustracij je preverjenih nekaj ključnih točk metod, kot so vpliv vzorčnih podatkov pri PEE, vpliv izbire praga pri EVE ter pomen pasovne širine pri NPE. Citirana literatura obravnava tudi nekatere druge lastnosti, vključno z vplivom porazdelitvenih funkcij v PE, različnimi uporabami EVE v različnih domenah, vplivom izbire jedrne funkcije v NPE ter pomenom in nujnostjo QE.

Na podlagi pregleda, primerjav, literature in ilustracij je podan povzetek lastnosti posameznih metod, vključno s kritičnimi dejavniki, prednostmi, slabostmi in področji uporabe:

1. Postopek PEE je preprost in učinkovit, toda v rezultatih se lahko pojavijo določene napake.
2. EVE velja za zgodovino obremenitev z dolgimi cikli obremenitev, izbira ustreznega praga ali velikosti bloka pri ekstrahiranju podatkov pa je težavna.
3. Pri ekstrapolaciji manjših in zmernih obremenitev se lahko uporabi NPE v kombinaciji z oceno jedra. Na verodostojnost rezultatov, ekstrapoliranih z NPE, vplivata jedrna funkcija in še posebej pasovna širina.
4. QE se lahko uporabi takrat, ko vzorčni podatki zajemajo različne delovne pogoje in obratovalne režime. QE je mogoče kombinirati tudi z drugimi metodami ekstrapolacije.

Ta pregled ima tudi nekaj pomanjkljivosti. Tako so bile v pregled vključene samo nekatere najbolj pogosto uporabljene metode ekstrapolacije v tehniki, dodati pa bi bilo treba tudi metode iz drugih področij. Uporaba metod ekstrapolacije ni popolnoma razdelana in zato bi bilo treba vključiti dodatno literaturo ter popolnejše smernice za izbiranje. Opraviti bi bilo treba tudi več eksperimentov za preverjanje lastnosti in ovrednotenje vpliva metod.

Končno je podanih tudi nekaj smeri za nadaljnje raziskave. Postaviti bi bilo mogoče kriterij za vrednotenje razlike med ekstrapoliranimi in izmerjenimi obremenitvami. Ekstrapolacije se uporabljajo na mnogih področjih, od koder bi si jih bilo mogoče izposoditi in jih smiselno prilagoditi. Rezultati ekstrapolacije morajo biti znotraj zgornjih in spodnjih fizičnih meja tehniških obremenitev, kar daje raziskavam pravilne ekstrapolacije poseben pomen.

Članek podaja izčrpen pregled pogosto uporabljenih metod ekstrapolacije v strojništvu, s tem pa prispeva k boljšemu razumevanju metod in njihovih lastnosti. V smernice za izbiro bi bilo mogoče vključiti tudi omembe uporabe metod, predlagane smeri nadaljnjih raziskav pa bi lahko pospešile razvoj na tem področju.

Ključne besede: kratkoročni spekter obremenitev, dolgoročni spekter obremenitev, ekstrapolacija obremenitev, parametrična ekstrapolacija, neparametrična ekstrapolacija, kvantilna ekstrapolacija

*Naslov avtorja za dopisovanje: Univerza v Jilinu, Fakulteta za tehniške vede in strojništvo, Changchun, Kitajska, 1518051537@qq.com

Na Fakulteti za strojništvo Univerze v Ljubljani so obranili svojo doktorsko disertacijo:

- dne *9. decembra 2015* **Igor PETROVIĆ** z naslovom: »Določitev vpliva odcepljenega toka na aerodinamične lastnosti membranskega aeroprofila« (mentor: prof. dr. Franc Kosel);

V nalogi je določen vpliv odcepljenega toka na aerodinamične lastnosti deformabilnega membranskega aeroprofila. Predlagan je numerični algoritem za reševanje dvojno povezane interakcije med fluidom in strukturo, ki je uporabljen za določitev vpliva geometrijskih in snovnih parametrov membrane ter vpliv presežne dolžine membrane na odcepitev in posledično aerodinamične lastnosti membranskih aeroprofilov. Razvit je aeroelastični model s tremi prostostnimi stopnjami, z vertikalnimi in horizontalnimi pomiki ter zasuki okoli prečne osi, ki v aerodinamičnem delu upošteva tudi vpliv odcepljenega toka in sile upora za določitev statičnih aeroelastičnih nestabilnosti krila, npr. divergenčne hitrosti. Rezultati numeričnih simulacij so primerjani z rezultati meritev v vetrovniku, za katere je izdelan merilni model. Ugotovljeno je dobro kvalitativno in kvantitativno ujemanje. Dobljeni numerični rezultati omogočajo razvoj modela majhnega brezpilotnega letala z membranskimi krili, katerega aerodinamične lastnosti so preverjene v vetrovniku;

- dne *23. decembra 2015* **Marko POLAJNAR** z naslovom: »Vpliv zdrsa med mazivom in površino na tribološke lastnosti mazanih kontaktov« (mentor: prof. dr. Mitjan Kalin);

V doktorskem delu smo preučevali vpliva zdrsa med površino in mazivom na trenje v mazanih inženirskih makro-kontaktih. V začetnem delu je predstavljeno teoretično ozadje obravnavanega problema in podan pregled dosedanjih raziskav na tem področju, ki pokaže, da je trenutno razumevanje zdrsa med inženirskimi površinami in mazalnimi olji slabo, tudi zaradi nerazumevanja vloge omočljivosti pri tem procesu. V rezultatih doktorske naloge smo tako predstavili medsebojne povezave površinskih lastnosti inženirskih površin in maziv z omočljivostjo, pri čemer smo ugotovili, da je za vrednotenje omočljivosti inženirskih površin z mazalnimi olji potrebno namesto kota omočljivosti uporabljati parameter razširjanja. Ta prameter je tudi ključno orodje za nadzor zdrsa in s tem trenja v mazanih kontaktih. Nadalje smo na podlagi ugotovitve, da vrsta medmolekulskih interakcij pomembno vpliva na omočljivost, predlagali okvirni model zdrsa, ki pojasni, da odsotnost trajnih polarnih interakcij med mazivom in površino povečuje zdrs. V nadaljevanju je predstavljen iterativni postopek za vrednotenje zdrsa v makro-kontaktih, pri čemer smo z vpeljavo novega parametra navideznega zdrsa, prikazali omejitve, doslej najpogosteje uporabljene zdrsne dolžine, za optimiranje tornih lastnosti v mazanih kontaktih, ki temelji na njeni odvisnosti od debeline mazalnega filma. Na koncu smo tudi prikazali, kako lahko s spreminjanjem površin kontakta in kontaktne kinematike, vplivamo na zdrs in trenje. Pri tem lahko podobne učinke znižanja trenja, kot v kontaktih z zdrsom na obeh kontaktnih površinah, pri določenih pogojih dosežemo že v kontaktih le z eno zdrsno površino, kar predstavlja pomemben tehnološki doprinos;

- dne *30. decembra 2015* **Klemen DOVRTEL** z naslovom: »Vremensko pogojeno aktivno naravno ogrevanje in hlajenje stavb« (mentor: prof. dr. Sašo Medved);

V doktorski nalogi je prikazan razvoj algoritma vremensko pogojenega delovanja sistemov aktivnega naravnega ogrevanja in hlajenja stavb. Na delovanje teh sistemov močno vplivajo meteorološke razmere, te pa vplivajo tako na potencial energijskega vira (sončno obsevanje, toplota in hlad okolja), ki ga izkoriščamo za ogrevanje in hlajenje stavb, kakor tudi na toplotni odziv sistemov in stavbe. Učinek in razpoložljiva moč energijskega vira sta zato odvisna ne le od trenutnega potenciala naravnih virov energije, temveč tudi od njihovega spreminjanja in pričakovanega toplotnega odziva stavbe v bližnji prihodnosti. Zato smo zasnovali scenarije delovanja sistema aktivnega naravnega ogrevanja in hlajenja ter razvili algoritem, s pomočjo katerega lahko njihovo delovanje optimiramo na podlagi vremenske napovedi. Algoritem vključuje tudi korekcijo vremenske napovedi, ki temelji na rekurzivni metodi korekcije vremenske napovedi z diskretnim Kalmanovim filtrom, s katerim napoved prilagodimo glede na lokalne, specifične lastnosti okolja. Na podlagi razvitega modela nestacionarnega toplotnega odziva sistema aktivnega naravnega ogrevanja in hlajenja ter modela nestacionarnega toplotnega odziva stavbe smo ob predvidenih vremenskih parametrih optimirali delovanje sistema. Na podlagi enokriterijske analize s Quazi-Newtonovo metodo in metodo Nelder-Maid ter večkriterijske analize na podlagi algoritma NSGAII in metode utežnih ostankov smo določili enokriterijski in večkriterijski optimum delovanja sistema. Algoritem vremensko pogojenega delovanja za primer hlajenja smo eksperimentalno preverili na modelu manjše bivalne enote.

Information for Authors

All manuscripts must be in English. Pages should be numbered sequentially. The manuscript should be composed in accordance with the Article Template given above. The maximum length of contributions is 10 pages. Longer contributions will only be accepted if authors provide juastification in a cover letter. For full instructions see the Information for Authors section on the journal's website: http://en.sv-jme.eu .

SUBMISSION:

Submission to SV-JME is made with the implicit understanding that neither the manuscript nor the essence of its content has been published previously either in whole or in part and that it is not being considered for publication elsewhere. All the listed authors should have agreed on the content and the corresponding (submitting) author is responsible for having ensured that this agreement has been reached. The acceptance of an article is based entirely on its scientific merit, as judged by peer review. Scientific articles comprising simulations only will not be accepted for publication; simulations must be accompanied by experimental results carried out to confirm or deny the accuracy of the simulation. Every manuscript submitted to the SV-JME undergoes a peer-review process.

The authors are kindly invited to submit the paper through our web site: http://ojs.sv-jme.eu. The Author is able to track the submission through the editorial process - as well as participate in the copyediting and proofreading of submissions accepted for publication - by logging in, and using the username and password provided.

SUBMISSION CONTENT:

The typical submission material consists of:

- A **manuscript** (A PDF file, with title, all authors with affiliations, abstract, keywords, highlights, inserted figures and tables and references),
- Supplementary files:
  - a **manuscript** in a WORD file format
  - a **cover letter** (please see instructions for composing the cover letter)
  - a ZIP file containing **figures** in high resolution in one of the graphical formats (please see instructions for preparing the figure files)
  - possible **appendicies** (optional), cover materials, video materials, etc.

Incomplete or improperly prepared submissions will be rejected with explanatory comments provided. In this case we will kindly ask the authors to carefully read the Information for Authors and to resubmit their manuscripts taking into consideration our comments.

COVER LETTER INSTRUCTIONS:

Please add a **cover letter** stating the following information about the submitted paper:

1. Paper **title**, list of **authors** and their **affiliations**.
2. **Type of paper**: original scientific paper (1.01), review scientific paper (1.02) or short scientific paper (1.03).
3. A **declaration** that neither the manuscript nor the essence of its content has been published in whole or in part previously and that it is not being considered for publication elsewhere.
4. State the **value of the paper** or its practical, theoretical and scientific implications. What is new in the paper with respect to the state-of-the-art in the published papers? Do not repeat the content of your abstract for this purpose.
5. We kindly ask you to suggest at least two **reviewers** for your paper and give us their names, their full affiliation and contact information, and their scientific research interest. The suggested reviewers should have at least two relevant references (with an impact factor) to the scientific field concerned; they should not be from the same country as the authors and should have no close connection with the authors.

FORMAT OF THE MANUSCRIPT:

The manuscript should be composed in accordance with the Article Template. The manuscript should be written in the following format:

- A **Title** that adequately describes the content of the manuscript.
- A list of **Authors** and their **affiliations**.
- An **Abstract** that should not exceed 250 words. The Abstract should state the principal objectives and the scope of the investigation, as well as the methodology employed. It should summarize the results and state the principal conclusions.
- 4 to 6 significant **key words** should follow the abstract to aid indexing.
- 4 to 6 **highlights;** a short collection of bullet points that convey the core findings and provide readers with a quick textual overview of the article. These four to six bullet points should describe the essence of the research (e.g. results or conclusions) and highlight what is distinctive about it.
- An **Introduction** that should provide a review of recent literature and sufficient background information to allow the results of the article to be understood and evaluated.
- A **Methods** section detailing the theoretical or experimental methods used.
- An **Experimental section** that should provide details of the experimental set-up and the methods used to obtain the results.
- A **Results** section that should clearly and concisely present the data, using figures and tables where appropriate.
- A **Discussion** section that should describe the relationships and generalizations shown by the results and discuss the significance of the results, making comparisons with previously published work. (It may be appropriate to combine the Results and Discussion sections into a single section to improve clarity.)
- A **Conclusions** section that should present one or more conclusions drawn from the results and subsequent discussion and should not duplicate the Abstract.
- **Acknowledgement** (optional) of collaboration or preparation assistance may be included. Please note the source of funding for the research.
- **Nomenclature** (optional). Papers with many symbols should have a nomenclature that defines all symbols with units, inserted above the references. If one is used, it must contain all the symbols used in the manuscript and the definitions should not be repeated in the text. In all cases, identify the symbols used if they are not widely recognized in the profession. Define acronyms in the text, not in the nomenclature.
- **References** must be cited consecutively in the text using square brackets [1] and collected together in a reference list at the end of the manuscript.
- **Appendix(-icies)** if any.

SPECIAL NOTES

Units: The SI system of units for nomenclature, symbols and abbreviations should be followed closely. Symbols for physical quantities in the text should be written in italics (e.g. *v*, *T*, *n*, etc.). Symbols for units that consist of letters should be in plain text (e.g. ms^{-1}, K, min, mm, etc.). Please also see: http://physics.nist.gov/cuu/pdf/sp811.pdf .

Abbreviations should be spelt out in full on first appearance followed by the abbreviation in parentheses, e.g. variable time geometry (VTG). The meaning of symbols and units belonging to symbols should be explained in each case or cited in a **nomenclature** section at the end of the manuscript before the References.

Figures (figures, graphs, illustrations digital images, photographs) must be cited in consecutive numerical order in the text and referred to in both the text and the captions as Fig. 1, Fig. 2, etc. Figures should be prepared without borders and on white grounding and should be sent separately in their original formats. If a figure is composed of several parts, please mark each part with a), b), c), etc. and provide an explanation for each part in Figure caption. The caption should be self-explanatory. Letters and numbers should be readable (Arial or Times New Roman, min 6 pt with equal sizes and fonts in all figures). Graphics (submitted as supplementary files) may be exported in resolution good enough for printing (min. 300 dpi) in any common format, e.g. TIFF, BMP or JPG, PDF and should be named Fig1.jpg, Fig2.tif, etc. However, graphs and line drawings should be prepared as vector images, e.g. CDR, AI. Multi-curve graphs should have individual curves marked with a symbol or otherwise provide distinguishing differences using, for example, different thicknesses or dashing.

Tables should carry separate titles and must be numbered in consecutive numerical order in the text and referred to in both the text and the captions as Table 1, Table 2, etc. In addition to the physical quantities, such as *t* (in italics), the units [s] (normal text) should be added in square brackets. Tables should not duplicate data found elsewhere in the manuscript. Tables should be prepared using a table editor and not inserted as a graphic.

REFERENCES:

A reference list must be included using the following information as a guide. Only cited text references are to be included. Each reference is to be referred to in the text by a number enclosed in a square bracket (i.e. [3] or [2] to [4] for more references; do not combine more than 3 references, explain each). No reference to the author is necessary.

References must be numbered and ordered according to where they are first mentioned in the paper, not alphabetically. All references must be complete and accurate. Please add DOI code when available. Examples follow.

Journal Papers:

Surname 1, Initials, Surname 2, Initials (year). Title. Journal, volume, number, pages, DOI code.

[1] Hackenschmidt, R., Alber-Laukant, B., Rieg, F. (2010). Simulating nonlinear materials under centrifugal forces by using intelligent cross-linked simulations. *Strojniški vestnik - Journal of Mechanical Engineering,* vol. 57, no. 7-8, p. 531-538, DOI:10.5545/sv-jme.2011.013.

Journal titles should not be abbreviated. Note that journal title is set in italics.

Books:

Surname 1, Initials, Surname 2, Initials (year). Title. Publisher, place of publication.

[2] Groover, M.P. (2007). *Fundamentals of Modern Manufacturing*. John Wiley & Sons, Hoboken.

Note that the title of the book is italicized.

Chapters in Books:

Surname 1, Initials, Surname 2, Initials (year). Chapter title. Editor(s) of book, book title. Publisher, place of publication, pages.

[3] Carbone, G., Ceccarelli, M. (2005). Legged robotic systems. Kordić, V., Lazinica, A., Merdan, M. (Eds.), Cutting Edge Robotics. Pro literatur Verlag, Mammendorf, p. 553-576.

Proceedings Papers:

Surname 1, Initials, Surname 2, Initials (year). Paper title. Proceedings title, pages.

[4] Štefanić, N., Martinčević-Mikić, S., Tošanović, N. (2009). Applied lean system in process industry. *MOTSP Conference Proceedings*, p. 422-427.

Standards:

Standard-Code (year). Title. Organisation. Place.

[5] ISO/DIS 16000-6.2:2002. *Indoor Air – Part 6: Determination of Volatile Organic Compounds in Indoor and Chamber Air by Active Sampling on TENAX TA Sorbent, Thermal Desorption and Gas Chromatography using MSD/FID.* International Organization for Standardization. Geneva.

WWW pages:

Surname, Initials or Company name. Title, from http://address, date of access.

[6] Rockwell Automation. Arena, from *http://www.arenasimulation.com,* accessed on 2009-09-07.

EXTENDED ABSTRACT:

When the paper is accepted for publishing, the authors will be requested to send an **extended abstract** (approx. one A4 page or 3500 to 4000 characters). The instruction for composing the extended abstract are published on-line: http://www.sv-jme.eu/information-for-authors/ .

COPYRIGHT:

Authors submitting a manuscript do so on the understanding that the work has not been published before, is not being considered for publication elsewhere and has been read and approved by all authors. The submission of the manuscript by the authors means that the authors automatically agree to transfer copyright to SV-JME when the manuscript is accepted for publication. All accepted manuscripts must be accompanied by a Copyright Transfer Agreement, which should be sent to the editor. The work should be original work by the authors and not be published elsewhere in any language without the written consent of the publisher. The proof will be sent to the author showing the final layout of the article. Proof correction must be minimal and executed quickly. Thus it is essential that manuscripts are accurate when submitted. Authors can track the status of their accepted articles on http://en.sv-jme.eu/.

PUBLICATION FEE:

Authors will be asked to pay a publication fee for each article prior to the article appearing in the journal. However, this fee only needs to be paid after the article has been accepted for publishing. The fee is 240.00 EUR (for articles with maximum of 6 pages), 300.00 EUR (for articles with maximum of 10 pages), plus 30.00 EUR for each additional page. The additional cost for a color page is 90.00 EUR. These fees do not include tax.

Strojniški vestnik -Journal of Mechanical Engineering
Aškerčeva 6, 1000 Ljubljana, Slovenia,
e-mail: info@sv-jme.eu

9 770039 248001
ISSN 0039-2480

http://www.sv-jme.eu

Contents

Papers